Electromagnetic Pulses Propagation in Dispersive Biological Cells with Arbitrary Shape

Politecnico di Bari

Department of Electrical and Information Engineering
Electrical and Information ENGINEERING
Ph.D. Program
SSD: ING-INF/02–ELECTROMAGNETIC FIELDS

Final Dissertation

Electromagnetic Pulses Propagation in Dispersive Biological Cells with Arbitrary Shape

---

by
Chiapperino Michele Alessandro

Supervisor:

Prof. Luciano Mescia

Coordinator of Ph.D. Program:
Prof. Alfredo Grieco

Course n°31, 01/11/2015-31/10/2018

Department of Electrical and Information Engineering
Electrical and Information ENGINEERING
Ph.D. Program
SSD: ING-INF/02–ELECTROMAGNETIC FIELDS

Final Dissertation

Electromagnetic Pulses Propagation in Dispersive Biological Cells with Arbitrary Shape

---

by
Chiapperino Michele Alessandro:
Michele A Chiapperino

Referees:

Prof. Clair Poignard

Prof. Damijan Miklavčič

Supervisor:

Prof. Luciano Mescia

Coordinator of Ph.D Program:

Prof. Alfredo Grieco

Course n°31, 01/11/2015-31/10/2018

ACKNOWLEDGEMENT

Firstly, I would like to express my sincere gratitude to my advisor Prof. Luciano Mescia for the continuous support of my PhD study and related research. His guidance helped me in all the time of research and writing of this thesis. My sincere thanks also goes to Prof. Damijan Miklavcic, who provided me the opportunity to join his research team at university of Ljubljana. A special thanks to Dr. Janja Dermol-Cerne for her costant support during and after the research period spent in Ljubljana.

ABSTRACT

The biomembrane is a critical biological structure essential for cell's function and survival. It enables separation between the cell's interior from its extracellular environment controlling the exchange of molecules and nutrients. When biomembranes are exposed to sufficiently intense pulsed electric fields (PEFs), structural changes resulting in formation of transient aqueous pores increase the membrane conductance enhacing the molecular exchange between the cell and its environment [1]. This non-thermal electromagnetic phenomenon, knows as electroporation (EP), is used in medical diseases treatment to deliver drugs, vaccine, genes and other molecules to mammalian cells [2]. Since the basic mechanisms of this process have not yet been fully clarified, different mathematical models of electroporation have been proposed in literature to study pore formation in biological membranes [3–5]. Major limitations of such models are due to the various approximations which they rely on, such as stationary dielectric properties and simple cell shapes. As a result, errors in estimating electroporation process can occur. In this PhD dissertation, the electroporation phenomenon induced by pulsed electric field on different biological cells and on multiple irregular cells systems is studied in detail. A nonlinear, non-local, dispersive and space-time multiphysic model based on Maxwells and asymptotic Smoluchowskis equations has been developed to calculate the transmembrane voltage and pore density along both plasma and nuclear membranes. The irregular cell shape has been modelled by incorporating in the numerical algorithm the Gielis superformula. The dielectric dispersion of the cell media has been modelled considering the multi-relaxation Debye-based relationship. In particular, the influence of electric pulse parameters, cell shape, cytoplasm and nuclear dielectric properties on the transmembrane voltage, pore density and electroporation relative length have been investigated.

Contents

List of Figures

List of Tables

List of Acronyms

AC - Alternating Current
DC - Direct Current
DNA - DeoxyriboNucleic Acid
ECT - Electrochemotherapy
EP - Electroporation
EPRL - Electroporation Relative Length
Np - Pulses Number
NTIRE - Nonthermal Irreversible Electroporation
PE - Pulse Energy
PEF - Pulsed Electric Field
RBCs - Red Blood Cells
RNA - RiboNucleic Acid
TDDS - Transdermal Drug Delivery System
TMV - Transmembrane Voltage

Chapter 1

CELL BIOLOGY AND ELECTROPORATION PROCESS

1.1 PROKARYOTIC AND EUKARIOTIC CELLS

The cell is the basic unit of living organisms. All cells are made from the same major classes of organic molecules: nucleic acids, proteins, carbohydrates and lipids. Depending how their genetic material is packaged, the cells are categorized in prokaryotes and eukaryotes (Fig. 1.1). The genetic material of a cell can be a gene, a part of a gene, a group of genes, a deoxyribonucleic acid (DNA) molecule, a fragment of DNA, a group of DNA molecules, or the entire genome of an organism. Prokaryotic cells do not have any membrane that encloses their genetic material. All known prokaryotes, such as bacteria, are single cells. They are also small, with a length of $1-2$ μm. In contrast, eukaryotic cells have a membrane that encloses their genetic material, which forms a structure called nucleus. A typical eukaryotic cell has additional membrane-bound organelles of different shapes and sizes. Most eukaryotic cells have size in the range between 5 μm and 100 μm, although some eukaryotic cells are large enough to be seen with the naked eye, i.e. frog egg size of 1 mm. Some eukaryotes, like amoebae exist as single cells. Other eukaryotic cells are part of multicellular organisms. For instance, all plants and animals are made of eukaryotic cells, that are organized into collectives of trillions of them called tissues [6].

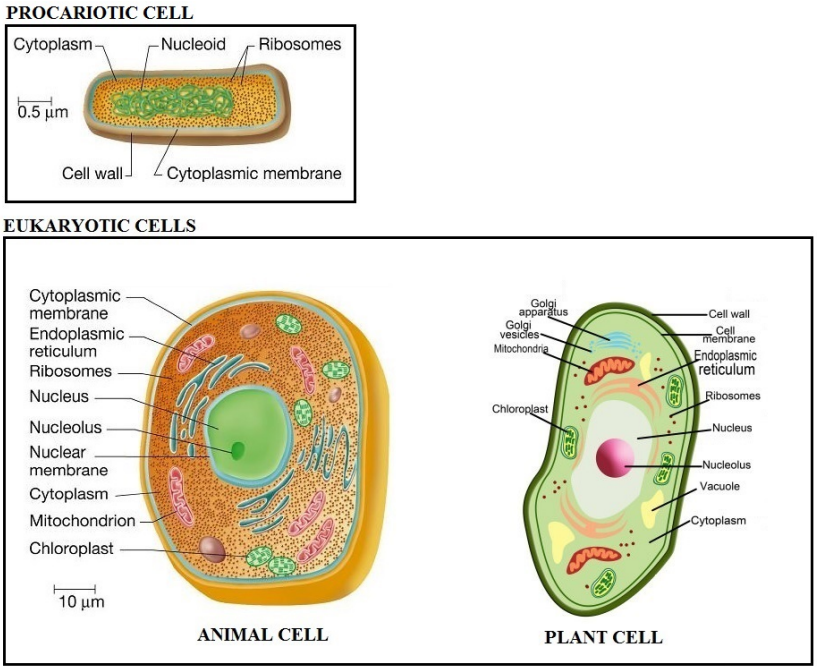

Figure 1.1: Prokaryotic and eukaryotic cells.

1.2 EUKARYOTIC ANIMAL CELL STRUCTURE

The fundamental constituents of a eukaryotic animal cell are the plasma membrane, the cytoplasm and the nucleus (Fig. 1.2) [6]. Plasma membrane defines the boundary of the cell dividing its internal living part from the nonliving extracellular medium. It is based on a framework of fat consisting molecules called phospholipids, which constitute a lipid bilayer having a hydrophilic head and a hydrophobic tail (Fig. 1.3). This structure prevents substances from entering or escaping the cell and it is typical also for the other membranes that define the boundaries of the internal organelles, such as nuclear membrane. Plasma membrane regulates the movement of materials into and out of the cell and facilitates electrical signaling between cells. Molecules of oxygen, carbon dioxide, nitrogen gas and water pass across the membranes by simple diffusion. In contrast, charged ions and glucose cannot dissolve in hydrophobic regions and therefore cannot cross membranes by simple diffusion (Fig.1.4).

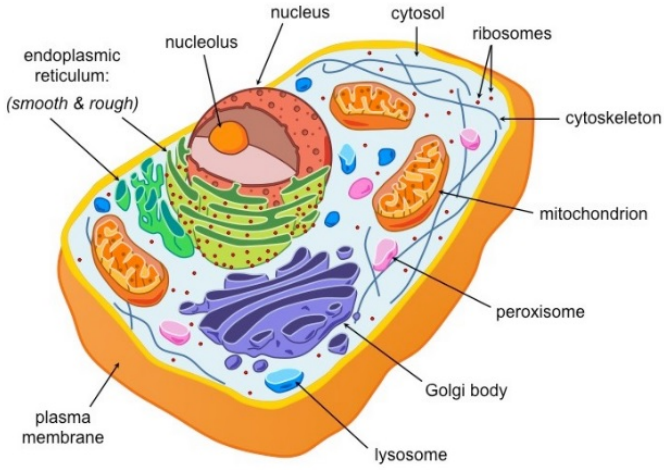

Figure 1.2: Eukaryotic animal cell structure.

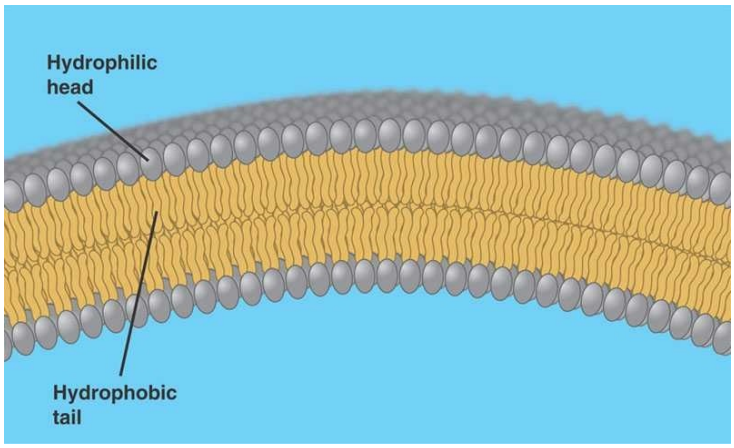

Figure 1.3: Plasma membrane lipid bilayer.

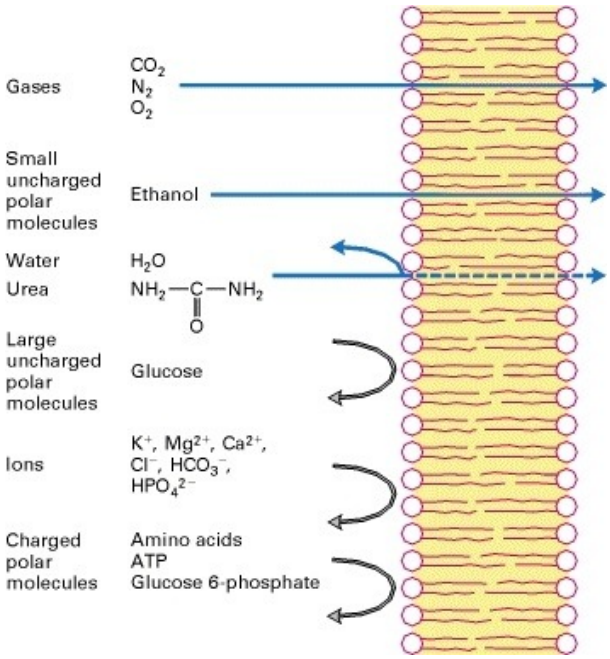

Figure 1.4: Permeability of plasma membrane to specific molecules.

All the membranes of the cell, including the plasma membrane, are also studded with proteins that serve various functions (Fig. 1.5). Receptor proteins serve as communicators, sending and receiving chemical signals from neighboring cells and the environment. Glycoproteins have many functions such as collagen or cell-to-cell adhesion. Channel and transport proteins act as gatekeepers, determining what substances can and cannot cross the membrane. Channel protein allow for facilitated diffusion by certain materials down the concentration gradient. Transport proteins are the main component of active transport and they allow for selective passage of specific molecules from the external environment. They move more molecules into and out of the cell, typically acting as a sort of pump. This process requires energy. The cytoplasm is constituted by a fluid part, called cytosol, and different organelles, such as mitochondria and Golgi bodies (Fig. 1.2). Cytoplasm executes the genetic instruction from the nucleus and it is the place where glycolysis and protein synthesis are performed to provide energy to the cell. The nucleus (Fig. 1.6) is bounded by a nuclear envelope composed of two membranes separated by an intermembrane space. A proteins network within the inner nuclear membrane, called nuclear lamina, adds rigidity to the nucleus.

Nuclear pores regulate the nuclear transport of molecules across the nuclear membranes. The nuclear membranes envelop the nucleoplasm of the cell, that includes the DNA genetic material (chromatin) and the nucleolus.

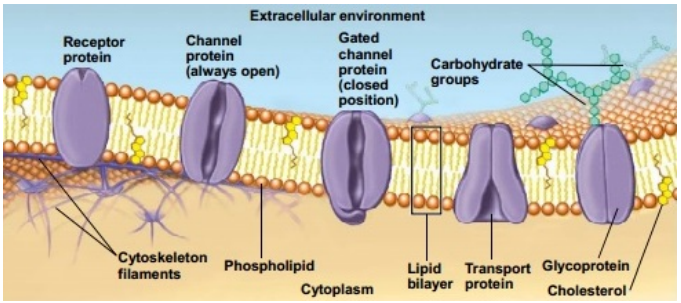

Figure 1.5: Proteins studded in the cell membranes.

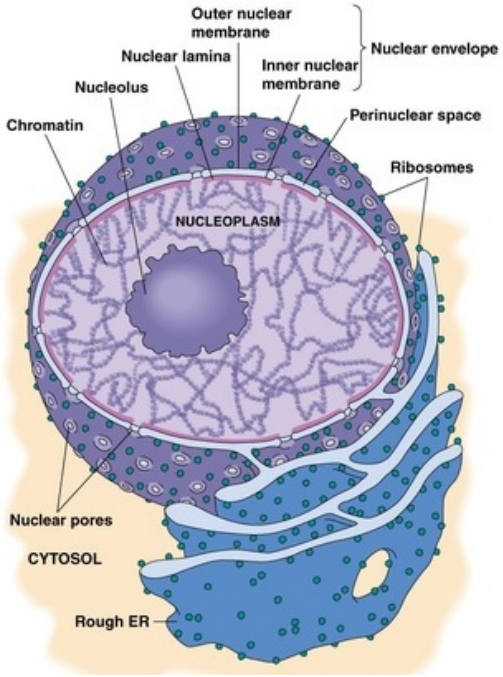

Figure 1.6: Nucleus structure.

1.3 OVERVIEW OF ELECTROPORATION

Acoustic, electrical, magnetic or optical forces are often used for the physical manipulation of biological cells. AC, DC or pulsed electric fields are adopted for the electromanipulation of biological cells for various applications, such as dielectrophoresis, electrorotation, electrodeformation, electrodisruption and electroporation [7]. For the transport of molecules through the cell membrane several methods have been developed, including: mechanical (microinjection), chemical (lipofection reagents), biological (viral vectors) and physical (sonoporation, magnetofection, electroporation) [8]. During the past four decades electroporation have gained increasing importance in biology and in medicine [9]. Electroporation (EP) is a non-thermal electromagnetic phenomenon in which an external pulsed electric field (PEF) triggers the creation of pores on cellular membranes increasing the membranes permeability [1]. Although electroporation is commonly used in biotechnology and medical applications, the molecular and cellular mechanisms of pores formation and stabilization during the electropermeabilization of membranes are still not fully understood and there are often discrepancies between experimental data and theoretical descriptions of pores creation [10]. Furthermore, the effect of electroporation depends on the cell type and the cell population in which it is located [11]. In fact, electroporation phenomenon is influenced by cell's dimension, its shape, its relative position to the direction of the electric field and the specific structure of the considered biological membrane [12, 13]. The electroporation's effectiveness is associated to the parameters defining the applied electric pulses such as the number, duration, frequency and intensity [14]. Depending on the intensity and duration of the applied electric field, the electroporation process could be reversible or irreversible. In the first case, when the electric field is removed, pores disappears, and the intact bilayer structure is reobtained. In the irreversible case the pores expansion leads to the mechanical rupture of the cell membrane [15]. Based on the type of electroporation, reversible or irreversible, the EP applications could be classified as functional or destructive. After the application of reversible EP the functionality of the cells or tissues is maintained inalterated.

Instead the application of irreversible EP produces the destruction of the plasma membranes of cells or microorganisms [16]. Electroporation technique has been used in biotechnology to incorporate various molecules, such as genes [17], DNA [9], RNA [18], proteins [19], drugs [20], antibodies [21] and fluorescent probes [22] into many different types of cells, like bacteria [23], yeasts [24], plant[25] and mammalian cells [26]. Moreover, electroporation can be used for achieving selective killing of cancer cells, tissue ablation and for nonthermal food and water preservation, mainly causing permanent destruction of microorganisms [7,27–29].

1.3.1 INDUCED TRANSMEMBRANE VOLTAGE

In a living cell the intrinsic membrane resting potential difference, ΔV_i is the electric voltage between the inside and outside the cell membrane in its unstimulated state. The sodium and potassium pumps, that are embedded in the cell membrane, generate across the membrane an electrical potential difference in the range of -90 mV up to -40 mV[6]. When a biological cell is exposed to an external electric field, a transmembrane voltage (TMV) is induced on the cell membranes. For an isolated spherical cell, exposed to a DC homogeneous electric field, the induced TMV membrane is given by the Schwan's equation [30]:

$$TMV = f_s ERcos(\theta) - \Delta V_i \tag{1.1}$$

where E is the applied external electric field, R is the radius of the cell, θ is the angle between the direction of the field and the normal to the cell surface and ΔV_i is the membrane intrinsic resting potential difference and f_s is obtained using the following equation [31]:

$$f_s = \frac{3\sigma_{Ex}\left[3R^2 h_m \sigma_{Cp} + \left(3Rh^2 - h^3\right) + \left(\sigma_m^0 - \sigma_{Cp}\right)\right]}{R^3\left(2\sigma_{Ex} + \sigma_m^0\right) + \left(2\sigma_m^0 + \sigma_{Cp}\right) + 2\left(R - h_m\right)^3\left(\sigma_{Cp} + \sigma_m^0\right)\left(\sigma_m^0 + \sigma_{Ex}\right)} \tag{1.2}$$

where σ_{Ex} is the conductivity of extracellular medium, σ_m^0 the passive conductivity of membrane, σ_{Cp} the conductivity of cytoplasm and h_m the thickness of membrane. As σ_{Cp},$\sigma_{Ex} \gg \sigma_m^0$ and $R \gg h_m$, $f_s \approx 1.5$.

Schwan's equation implies that the transmembrane potential varies proportionally to the cosine of the angle and the maximum potential is induced at the points where the electric field is perpendicular to the membrane. The critical TMV built up for electroporation to occur is about ± 1 V [32].

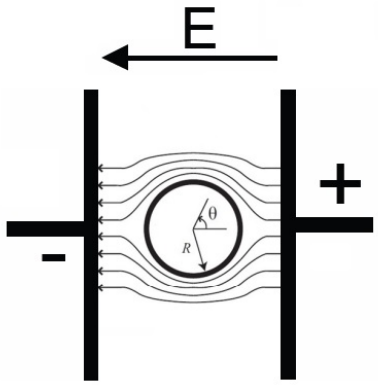

Figure 1.7: Isolated spherical cell exposed to a DC homogeneous electric field.

1.3.2 EQUIVALENT CIRCUIT MODEL OF CELL

In order to describe the electroporation effect of electrical pulses on cells over a wide range of pulse duration, in this work the following equivalent circuit model of cell has been taken into account [33]:

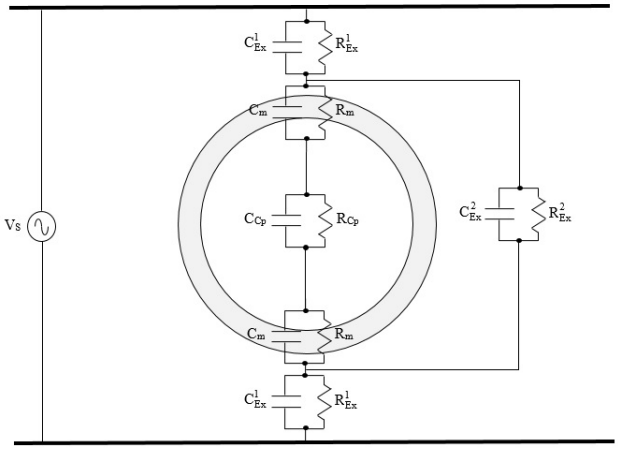

Figure 1.8: Equivalent circuit model of cell.

with:

$$R_{Ex}^{1} = \frac{h_{Ex}^{1}}{S\sigma_{Ex}} \tag{1.3}$$

$$C_{Ex}^{1} = \frac{S\varepsilon_{Ex}}{h_{Ex}^{1}} \tag{1.4}$$

$$R_{m} = \frac{h_{m}}{S\sigma_{m}^{0}} \tag{1.5}$$

$$C_{m} = \frac{S\varepsilon_{0m}}{h_{m}} \tag{1.6}$$

$$R_{Cp} = \frac{h_{Cp}}{S\sigma_{Cp}} \tag{1.7}$$

$$C_{Cp} = \frac{S\varepsilon_{Cp}}{h_{Cp}} \tag{1.8}$$

$$R_{Ex}^{2} = \frac{h_{Ex}^{2}}{S\sigma_{Ex}} \tag{1.9}$$

$$C_{Ex}^{2} = \frac{S\varepsilon_{Ex}}{h_{Ex}^{2}} \tag{1.10}$$

where R_{Ex}^{1}, C_{Ex}^{1} and h_{Ex}^{1} are, respectively, the resistance, the capacitance and the thickness of extracellular medium between electrode and cell membrane, ε_{Ex} the permittivity of extracellular medium, R_m the resistance of membrane, C_m the capacitance of membrane, ε_{0m} the static permittivity of membrane, R_{Cp} the resistance of cytoplasm, C_{Cp} the capacitance of cytoplasm, ε_{Cp} the permittivity of cytoplasm, h_{Cp} the thickness of cytoplasm, R_{Ex}^{2}, C_{Ex}^{2} and h_{Ex}^{2}, respectively, the resistance, the capacitance and the thickness of extracellular medium between electrodes, S the effective cross-sectional area and V_s the applied voltage signal.

1.3.3 THEORETICAL MODEL OF PLANAR LIPID BILAYERS ELECTROPORATION

A number of theoretical models have been proposed for the explanation of electroporation. The hydrodynamic, the elastic, the viscoelastic, and the viscohydroelastic models consider electroporation as a large scale phenomenon, in which the molecular structure of the membrane plays no direct role [10].

The phase transition model and the domain-interface breakdown models explain the electroporation by the properties of individual lipid molecules and the interactions between them [10]. The aqueous pore formation offers a compromise between these two approaches considering the electropermeabilization as a result of the formation of transient aqueous pores in the lipid bilayer [10, 34]. When the intact phospholipid bilayer (Fig. 1.9a) is exposed to an external electric field transient unstable pores are created in the membrane. These pores, called pre-pores, are hydrophobic since their walls are formed by the hydrophobic tails of the phospholipid molecules (Fig. 1.9b). The pre-pores expansion leads from a hydrophobic state to a hydrophilic structure, where the lipids adjacent to the aqueous inside of the pore are reoriented in a manner that their hydrophilic heads are facing the pore, while their hydrophobic tails are hidden inside the membrane (Fig. 1.9c). In case of reversible electroporation, when the electric field is removed, the metastable pores reseal and the intact bilayer structure is reobtained. After electric field removal pores have lifetimes ranging from milliseconds up to minutes. When pores radius exceeds a critical value, pores convert into unstable self-expanding hydrophilic pores (Fig. 1.9d). In this case the electroporation is irreversible and the pores expansion leads to the mechanical rupture of the cell membrane[10, 15, 35].

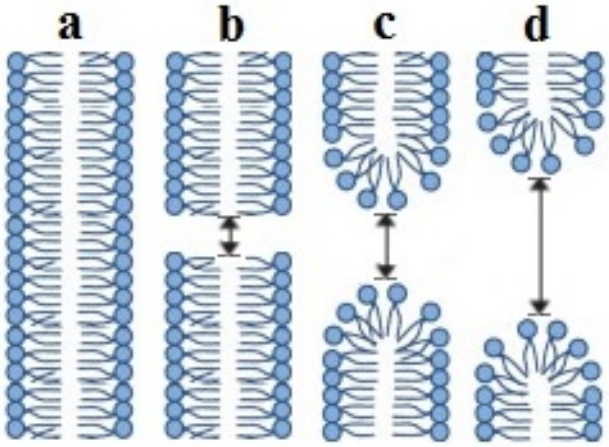

Figure 1.9: (a) Intact bilayer; (b) hydrophobic pre-pore; (c) metastable hydrophilic pore; (d) unstable self-expanding hydrophilic pore.

1.4 EP MATHEMATICAL MODELS

Different mathematical models of electroporation have been proposed in literature to study pore formation in plasma and nuclear membranes. Those models can be classified as nonlinear with cell compartments treated as nondispersive media[3, 13, 36–41] or linear with cell compartments treated as dispersive media [5,11,42]. However, in nanosecond pulses regime the frequency dependent dielectric properties of membranes, intracellular and extracellular media have to be considered to obtain an accurate and predictive model of electroporation [11, 43, 44]. Moreover, to model the pores creation process inside the membranes the dielectric dispersion relationships pertaining the cell media should be used in conjunction with the electroporation nonlinear model. Nonlinear dispersive model of electroporation for a spherical single-shell cell were discussed in literature [4, 36]. Different papers also illustrate the influence of the irregular shape of the membrane on the electroporation process [11, 13, 36, 42]. Furthermore in [45] a dynamic model of electroporation is presented. The model is based on the chemical-kinetics model and trapezium barrier model. In the calculation two types of pores are taken into account, prepores (P_1)and final pores (P_2). The model evaluates the pore distribution on the membrane solving equations with field-dependent rate coefficients. The conductivity of pores is computed using the trapezium barrier model for the image forces. Thus the membrane conductivity is obtained solving the following equation:

$$\sigma_m(\mathbf{r},t) = \sigma_m^0 + \sigma_{\mathrm{p},1} P_1(\mathbf{r},t) + \sigma_{\mathrm{p},2} P_2(\mathbf{r},t) \tag{1.11}$$

where t is the time, $\mathbf{r}$ the radius vector, σ_m^0 the initial conductivity of the membrane, $\sigma_{\mathrm{p},1}$ and $\sigma_{\mathrm{p},2}$ the intrinsic pore conductivities of pores P_1 and P_2, $P_1(\mathbf{r},t)$ and $P_1(\mathbf{r},t)$ the states of the considered pores. Finally, the model is integrated with a molecular transport model for a single cell to calculate the molecular uptake of cells. In my PhD work, a nonlinear dispersive model of electroporation for irregular cells is presented. The nonlinear effect due to the pore creation is modelled in accordance to the asymptotic electroporation model based on Smolouchouski partial differential equation [28, 46, 47].

The dielectric properties of the biological cell media are described using the multi-relaxation Debye-based equation. Using a finite element based technique, the quasi-static Maxwell equations, the Smolouchouski partial differential equation and the differential equation relating the electric and polarization fields are simultaneously solved in the 4D space-time domain. Moreover, the irregular cell shape has been modelled by the Gielis superformula [48–50].

1.4.1 CONVENTIONAL EP AND NANO-EP

Conventional methods of electroporation use pulses of micro-millisecond duration to electroporate the cells. In this case, since the cytoplasm and the extracellular medium act like good conductors, only the plasma membrane is electroporated. The biomembranes electroporation obtained using high intensities nanosecond pulsed electric filed (nsPEF) is termed Nanoelectroporation. Nano-EP is used to disturb the internal cellular structures such as nucleus, mitochondria and endoplasmic reticulum. Based on the duration and magnitude of applied pulses, Nano-EP may cover both the plasma and nuclear membranes, or it could affect only the nuclear membrane leaving intact the plasma one[51]. According to the theoretical modeling, the pulses of nanosecond-duration should create smaller pores than the pulses of micro-millisecond duration. At the same time, the number of pores created by nanosecond-duration pulses should be by 2-3 orders of magnitude larger than in the case of longer pulses [52]. Moreover, nsPEF induces different physiological changes in mammalians cells leading to apoptosis in cancer cells [53], release of calcium from endoplasmic reticulum and calcium uptake from the membranes outside [54], caspase activation[55], externalization of phosphatidylserine (PS)[56], calcium bursts [57], cytochrome C release [58] and DNA fragmentation [59].

1.5 EP MEDICAL APPLICATIONS

1.5.1 ELECTROCHEMOTHERAPY

Electrochemotherapy (ECT) is an antitumor treatment that combines the electroporation of membranes and the transport of cytotoxic drugs such as bleomycin and cisplatin. Pulsed Electric Fields (PEF) are locally delivered at the tumor site, allowing nonpermeant cytotoxic drugs to enter the transiently permeabilized cancer cells and to kill them [9, 60]. Cell electropermeabilization allows the drug to be highly cytotoxic at concentrations several orders of magnitude lower than those necessary to kill unpermeabilized cells [61]. Furthermore, the application of electric pulses to tissues generates an interruption of the blood flow, named vascular lock. In tumors vascular lock is of a longer duration than in normal tissues and results in a vascular disruption effect in tumor site [9]. Electrochemotherapy is used in clinics for treatment of solid tumours. For small tumours electric pulses are delivered to the tissue usually via two metal plate electrodes. Instead, for electrochemotherapy of larger tumours multiple needle electrodes were used to cover the whole tumour with sufficiently high electric field [62]. In treatments, a train of eight electric pulses with intensity of 400-900 $\mathrm{V/cm}$ and repetition frequency of 1 Hz is usually applied to the tumors [63]. Each pulse in the train excites underlying nerves and provokes muscle contractions. To reduce the number of muscle contractions and the pain associated with electrochemotherapy, the use of pulses with repetition frequency exceeding the frequency of tetanic contraction have been proposed [64]. Clinical studies demonstrate the effectiveness of ECT with an objective response rate of more than 80 % [65]. Electrochemotherapy is used for the treatment of cutaneous and subcutaneous tumours and several reports demonstrate its effectiveness in tumour nodules of different histologies: melanoma [66], breast carcinoma [67], head and neck tumours [68], squamous cell carcinoma [69], basal cell carcinoma [70]. Electrochemotherapy is easy and quick (25 min) to perform and can be applied in general or local anaesthesia. In the case of large tumour nodules several applications of electric pulses are required and as demonstrated in different clinical cases, electrochemotherapy is very effective in repetitive treatments [65].

1.5.2 NONTHERMAL IRREVERSIBLE EP FOR TISSUE ABLATION

Over the years, a number of minimally invasive surgical technique for tissue ablation have been developed to selectively destroy specific areas of undesirable tissues, such as: cryosurgery, nonselective chemical ablation, focused ultrasound, radiofrequency ablation, interstitial laser coagulation, electrochemotherapy. Nonthermal irreversible electroporation (NTIRE) is an emerging minimally invasive surgical procedure to ablate tissue. NTIRE applies high voltage electrical pulses on the microsecond timescale with inserted needle-like electrodes inducing irreversible permeabilization of the cells membrane and the consequent cells death. This technique has the advantages that it is easy to apply, can be monitored and controlled with electrical impedance tomography, is not affected by local blood flow, does not require the use of adjunctive drugs, does not produce any collateral damage to anatomical borders and does not cause protein denaturation [71, 72]. In contrast, the strong electric fields used in NTIRE induce muscle contractions and thus special anesthesia are required during the treatment. Futhermore, several patients have been managed by electrocardiographically to control cardiac arrhythmias developed during NTIRE. Several studies demonstrate the NTIRE successful effectiveness in tumor ablation in pancreatic and prostate cancer [9].

1.5.3 TRANSDERMAL DRUG DELIVERY AND GENE ELECTROTRANSFER

The transdermal drug delivery system (TDDS) is an alternative to intravenous or oral drug introduction, that avoid the livers first-pass effect and the serious effects on the gastrointestinal tract of oral dosage forms. However, the effectiveness of TDDS is limited by the formidable barrier of the stratum corneum. To promote the skin permeation of drugs several methods have been evaluated. Among these methods, electroporation has shown to be an effective TDDS. EP involves the creation of tiny and transient aqueous pathways in the transcellular lipid region in the stratum corneum barrier, thus enhancing transdermal drug delivery.

The application of high-voltage electric pulses with time duration of millisecond order results in the enhanced permeation of high molecular compounds through the skin [20]. The molecules pass through electroporated skin mainly by diffusion during and after the application of the electrical pulses and by electrophoresis with a slight electroosmosis during the application of the pulses. In general, the increase in amplitude, duration and number of pulses generates an increase in the permeability of the stratum corneum, allowing a better transport of the drug. The treatment has been shown to successfully enhance the delivery through the skin of many drugs and molecules with differing lipophilicity and size. In contrast, the main obstacle in the use of TDDS by electroporation is represented by the poor control of the dose administered during the treatment. Furthermore, the choice of electric pulses and electrodes must be accurate in order to avoid to the skin [9, 73]. Gene electrotransfer (GET) employs electroporation technique to transfer genetic material into biological cells. GET has been successfully used for gene transfection of bacteria, DNA vaccination, regenerative medicine applications and cancer treatment. In particular, DNA vaccination is a technique in which genetically engineered DNA is delivered to biological organism to produce an immunological response[9, 17].

Chapter 2

MATHEMATICAL MODELING OF ELECTROPORATION

2.1 EP MATHEMATICAL FORMULATION

The modeling of the EP effects on intracellular electric field is a subject of increasing research activities since it is the key issue in electric field-mediated molecular delivering. Qualitatively, external PEF field application can strongly change the dimension and spatial distribution of the membrane pores modifying the cell electric parameters and increasing the intra-cellular electric field. As a consequence, to evaluate the PEF distribution inside the cell during EP process it is necessary to consider suitable theoretical models and computational techniques based on both the Maxwell and poration equations. Such approaches are essential to gain insights into the mechanism of membrane permeabilization, to identify the fundamental parameters involved in noninvasive diagnosis and medical sensors as well as to provide guidance for computational dosimetry and for the development of specific therapeutic approaches. In fact, the efficiency of EP-based therapies and treatments strongly depends on the magnitude, shape and duration of the applied PEF, polarity, number of pulses and repetition frequency.

A number of theoretical and numerical models of cell EP are available in the scientific literature [4, 13, 36, 74–79]. Major limitations of such models are due to the various approximations which they rely on, such as spatial uniform distribution

of electric conductivity, stationary dielectric properties, simple cell shapes. As a result, errors in estimating the angular width of the electroporated membrane, TMV and pore density dynamics, threshold amplitude of external electric field can occur. In order to provide a realistic description of the electric phenomena involved during EP process, the computational approach has to be able to deal with geometry, physical properties and broadband response of the exposed cell as well as to be numerically robust and appropriate for the current computer technology. Moreover, a numerical code should be able to correctly model, especially in the nanosecond time scale, the effects of dielectric dispersion of external medium, plasma membrane and cytoplasm media. Because of these demands and considering that EP simulations and optimization require significant computational burden, the development of numerical models for predicting the effects of PEF on cells is still needed. As a result, we present here a numerical model describing the EP on irregularly shaped cells [80]. The 3-D quasi-static formulation of the Maxwell's equations is used in conjunction with the nonlinear Smoluchowski equation describing the pore dynamics [13, 36, 40]. Moreover, the dielectric dispersion laws of each cell compartment have been suitably formulated to be correctly incorporated inside the kernel of the numerical code. In proposed study, a non-local mathematical model was employed since the pore density across a given point of the plasma membrane depends on the TMV of the whole cell membrane domain. In other words, in addition to the temporal evolution, the spatial distribution of the membrane conductivity is modeled, too. Finally, the irregular geometry of the cells has been described by Gielis' superformula [48–50]. The unified geometrical description provided by such formula makes possible the generation of a countless and sophisticated 2-D and 3-D shapes in a simple and analytical way by changing a reduced number of parameters. In particular, the superformula is able to cover a wide variety of cell morphologies, e.g. different types of red blood cells, box-shaped tissue cells, oval cells, muscular cells as well as simple spheres or ellipsoids. In this way, the calculation of the spatial distribution of the TMV on the irregular plasma membrane is carried out allowing a reliable estimation of both time and spatial dependence of the pore density.

2.2 GIELIS' SUPERFORMULA

The Gielis' superformula is a generalization of the superellipse curves or also known as Lamé curves (see Fig. 2.1). In the Cartesian coordinate system the superellipse curves are described by the following equation [48]:

$$\left|\frac{x}{a}\right|^n + \left|\frac{y}{b}\right|^n = 1 \tag{2.1}$$

where n, a and b are positive real numbers. The Lamé equation (2.1) makes possible the modelling of the classical circle and square shapes as well as the intermediate ones. The costants a, b and n define the height, width and shape of the resulting curve, respectively. As n approaches zero the curve degenerates to two straight crossed lines along the axes. When $n = 1$ a diamond with vertices on the axes is obtained. For $n = 2$, it is generated an ellipse that degenerate in a circle when $a = b$. If the value of n is increased beyond two superellipses are created. As n approaches infinity the shape becomes a rectangle.

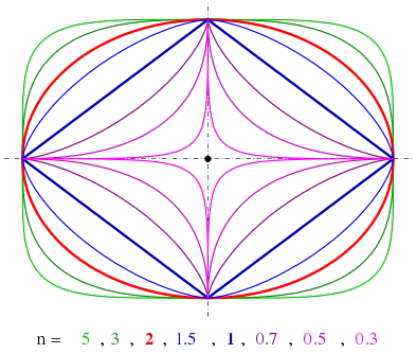

Figure 2.1: Examples of superellipses for $a = 1$ and $b = 0.75$.

Reformulating the Lamé equation in polar coordinates, the following equation is obtained [48]:

$$R(\theta) = \frac{r}{\sqrt[n]{|cos\theta|^n + |sin\theta|^n}} \tag{2.2}$$

where r and θ are the radial azimuthal coordinates, respectively.

By introducing the parameter $m/4$ the polar plane is separated into a number of sectors and the following equation can be written:

$$R(\theta) = \frac{r}{\sqrt[n]{\left|cos\frac{m\theta}{4}\right|^n + \left|sin\frac{m\theta}{4}\right|^n}} \tag{2.3}$$

Further elaborating Eq. (1.3) the Gielis' superfomula is obtained:

$$R(\theta) = f(\theta)\left(\left|\frac{cos\frac{m_1\theta}{4}}{a_1}\right|^{n_1} + \left|\frac{sin\frac{m_2\theta}{4}}{a_2}\right|^{n_2}\right)^{-\frac{1}{b_1}} \tag{2.4}$$

where $f(\theta)$ is a generic function and in particular it can be constant, exponential, spiral, or a trigonometric function. If $f(\theta)$ is a constant, the circle can be modified in various shapes. Supershaped spirals are obtained when $f(\theta) = exp(\alpha\theta)$. While supershaped Archimedean spirals are obtained when $f(\theta) = \theta$ (Fig. 2.2 [81]).

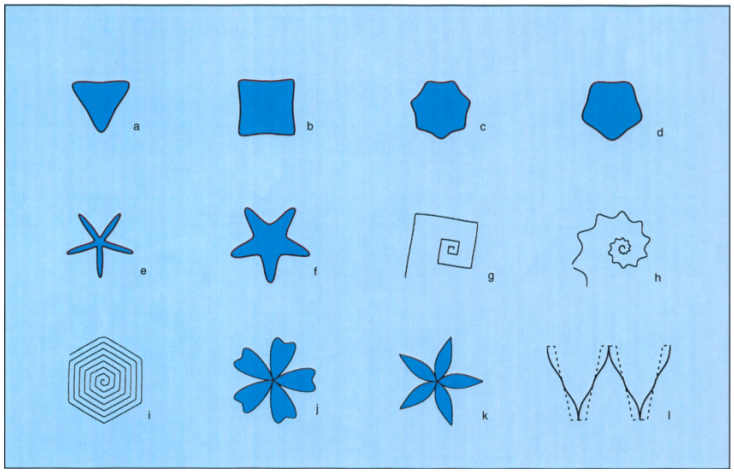

Figure 2.2: a-d: cross sections of plant stems; e-f: starfish; g-h: spirals; i: Archimedean spirals; j-l: transformations of cosines.

The origin of the Gielis transformations can be assessed in the context of botany. In fact, when $f(\theta)$ is a cosine function, many natural flowers shapes result (see Fig. 2.3 [81]). By changing the paramenters of the superformula many shape can be obtained (Fig. 2.4 and Fig. 2.5 [82]). In the case of $m_1 = m_2 = m$ (m is a positive integer) eq. (2.5) generates a certain variety of symmetric shapes and m represents the number of symmetry axis or the number of sectors in which the plane is folded. In particular, zerogons ($m = 0$), monogons ($m = 1$), and diagons ($m = 2$), as well as triangles, squares, and polygons with higher rotational symmetries can be defined. The parameters a_1, a_2 control the relative scale of the supershape over each sector. Coefficients n_1, n_2, and b_1 control the shape. In particular, for $n_1 = n_2 < 2$ the shape is inscribed, while for $n_1 = n_2 > 2$ the shape circumscribes the circle. Moreover, changing the coefficient b_1 the corners can be sharpened or flattened and the sides can be straight or bent. The trios (a, n_1, b_1) and (b, n_2, b_1) determine the pseudo-vertices sharpness (or roundness) and the pseudo-sides convexity (or concavity) together with the span of the pseudo-polygon. More complex shapes can be produced using real-valued $m_1 \neq m_2$ and combining eq. (2.5) with other functions [48].

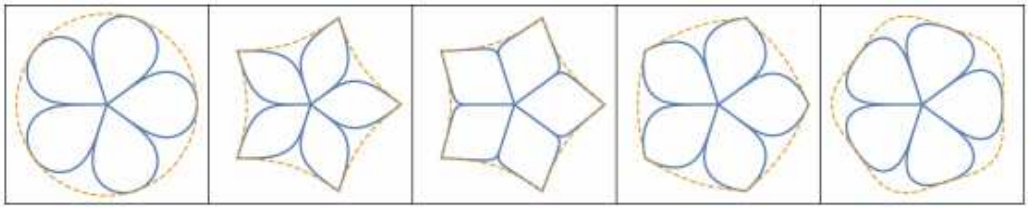

Figure 2.3: Choripetalous five-petalled flowers.

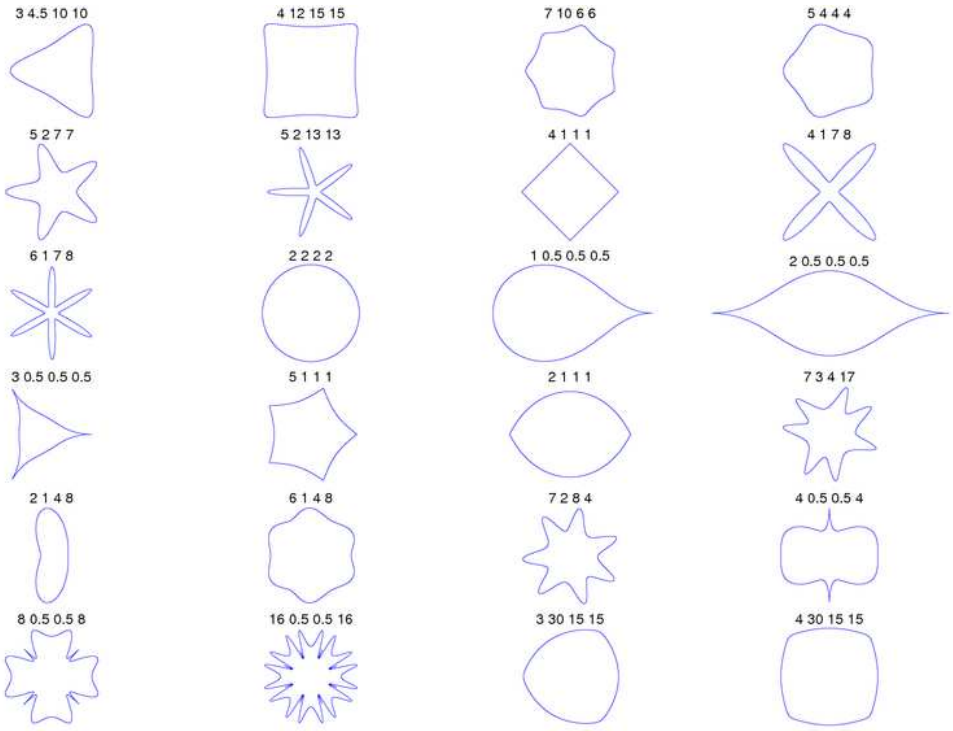

Figure 2.4: Example of 2D shapes obtained using different values of Gielis' paramenter $m_1 = m_2 = m$, b_1, n_1, n_2 and $a_1 = a_2 = 1$.

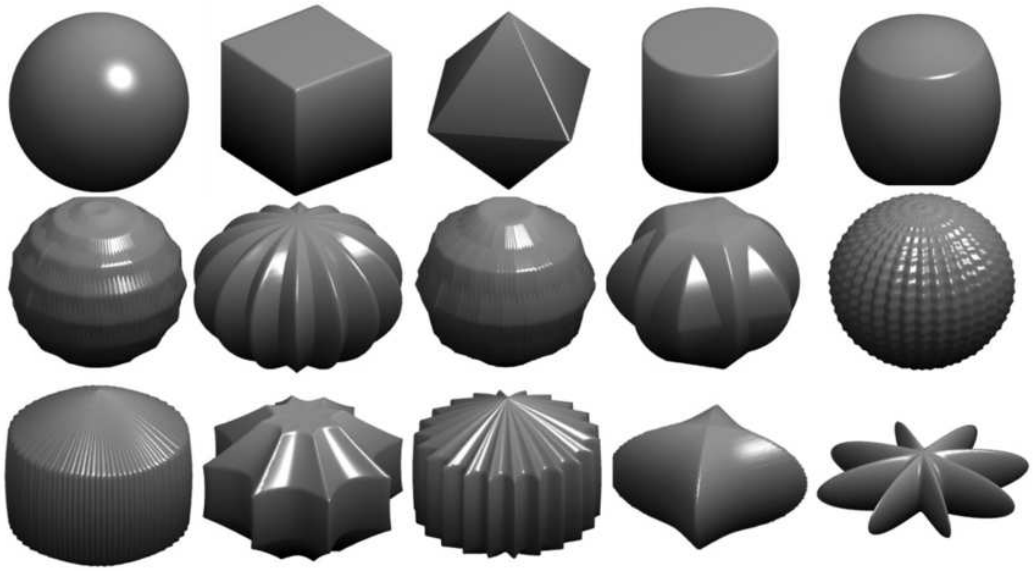

Figure 2.5: Example of 3D shapes obtained using Gielis superformula.

Furthermore, the Gielis superformula can be generalized by considering the arguments of cosine and sine to be functions [83]:

$$R(\theta) = f(\theta)\left(\left|\frac{cos\frac{m_1 g_1(\theta)}{4}}{a_1}\right|^{n_1} + \left|\frac{sin\frac{m_2 g_2(\theta)}{4}}{a_2}\right|^{n_2}\right)^{-\frac{1}{b_1}} \tag{2.5}$$

where $g_1(\theta)$ and $g_2(\theta)$ are continuous functions. This generalized form of the Gielis formula allows the creation of asymmetric and nested structures (Fig. 2.6 [84]). The Gielis transfomation has been employed in different fields of application. In engineering it has been used to optimize the shapes of wind turbines or the shape of non-planar wings in aircraft [81]. In the field of telecommunications it has been used to design waveguides and antennas and to optimize lasers [81]. In biology, it has been used to model the annual rings in trees or to model the backbone of RNA [81]. In this work Gielis' formula is used to describe the irregular shape of biological cells.

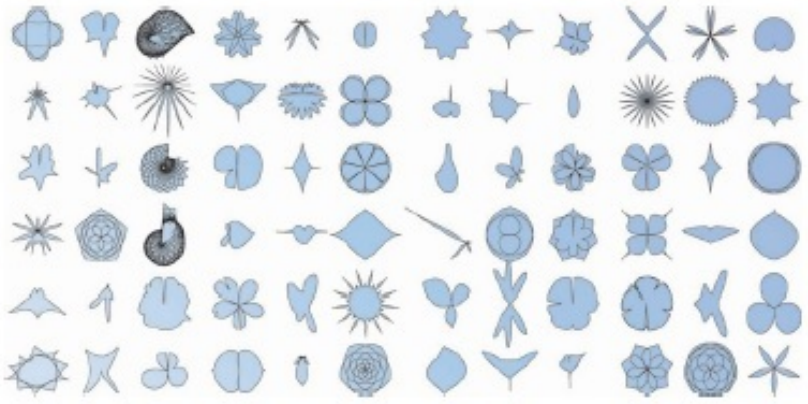

Figure 2.6: Example of more complex shapes obtained using Gielis superformula.

2.3 CELL GEOMETRY MODEL

Most of the studies available in the scientific literature regarding to the calculation of TMV are based on models relying on a simple geometrical description of the cells in terms of canonical shapes (e.g., circular or elliptical) or a combination of those. Such approach can result in inaccurate results because of the rough approximation of the actual cells shape. In order to overcome this drawback, in this study , the irregular cells shape is described by using the Gielis' superformula. This allows the analytical description of the cells geometry, as well as a more versatile framework to investigate the sensitivity of TMV to the variation of the geometrical parameters. In particular, by using the model illustrated in Fig. 2.7 the radius vector describing the cell perimeter is given by:

$$\mathbf{r}_{\mathrm{i,j}} = \hat{\mathbf{r}}_{\mathrm{i,j}} \sqrt{{x_{\mathrm{i,j}}}^2 + {y_{\mathrm{i,j}}}^2} \tag{2.6}$$

$$x_{\mathrm{i,j}} = A_{\mathrm{i,j}} R_{\mathrm{i,j}} \left(\theta_{\mathrm{i,j}}\right) \cos\theta_{\mathrm{i,j}} \tag{2.7}$$

$$y_{\mathrm{i,j}} = B_{\mathrm{i,j}} R \left(\theta_{\mathrm{i,j}}\right) \sin\theta_{\mathrm{i,j}} \tag{2.8}$$

$$R_{\mathrm{i,j}}\left(\theta_{\mathrm{i,j}}\right) = \left(\left| \frac{\cos\left(m_{\mathrm{i,2j\text{-}1}}\theta_{\mathrm{i,j}}/4\right)}{a_{\mathrm{i,2j\text{-}1}}} \right|^{n_{\mathrm{i,2j\text{-}1}}} + \left| \frac{\sin\left(m_{\mathrm{i,2j}}\theta_{\mathrm{i,j}}/4\right)}{a_{\mathrm{i,2j}}} \right|^{n_{\mathrm{i,2j}}} \right)^{-\frac{1}{b_{\mathrm{i,j}}}} \tag{2.9}$$

with $i = 1,..,C_N$ and $j = 1,..,M_N$, where C_N is the cells number, M_N the membranes number, $\theta_{\mathrm{i,j}} \in [0, 2\pi]$ is a convenient angle parameters, $b_{\mathrm{i,j}} \in \mathbb{R}^+$(positive real numbers), $a_{\mathrm{i,2j\text{-}1}} \in \mathbb{R}_0^+$ and $a_{\mathrm{i,2j}} \in \mathbb{R}_0^+$(strictly positive real numbers), $\mathrm{A_{i,j}}$ and $\mathrm{B_{i,j}}$ are the scaling factors.

2.4 ELECTROMAGNETIC MODEL

As illustrated in Fig. 2.7, a pulsed electric field is generated by using two parallel–plate electrodes placed at the top and bottom surfaces of the cylinder bounding the computational domain. Since the cell dimension is negligible in comparison to the field wavelength, and the wave propagation time across the cell is much smaller than the rise time of the applied pulse, the electromagnetic problem can be considered as quasi–static and modeled by using the Laplace equation subject

to the appropriate boundary conditions. In particular, for each cell compartment the following partial differential equation is solved numerically:

$$\nabla \cdot \nabla \left(\sigma + \varepsilon_0 \frac{\partial \phi}{\partial t} \right) - \frac{\partial}{\partial t} \nabla \cdot \mathbf{P} = 0 \tag{2.10}$$

in conjunction with the equations (2.13)–(2.27) and the equation:

$$\mathbf{E} = -\nabla \phi \tag{2.11}$$

where σ is the static ionic conductivity, ϕ the electric scalar potential and $\mathbf{P}$ the polarization vector. The TMV is calculated as the difference between the electric potential on the interior (I) and outer (O) sides of each cells membranes:

$$\mathrm{TMV}_{\mathrm{i,j}}(x,y,t) = \phi^{\mathrm{I}}{}_{\mathrm{i,j}}(x,y,t) - \phi^{\mathrm{O}}{}_{\mathrm{i,j}}(x,y,t) \tag{2.12}$$

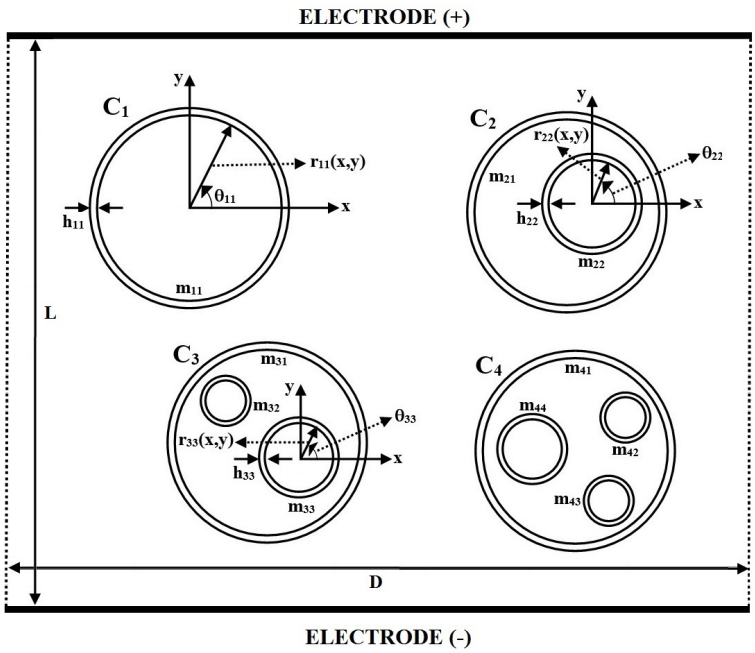

Figure 2.7: Schematic picture of the 2-D arbitrarily shaped cells exposed to uniform pulsed electric field.

2.5 COMPLEX PERMITTIVITY MODEL

The dielectric properties of the cell compartments are due to the interaction of the electromagnetic field with the material constituents, and they depend on the working frequency as well as the dynamic processes involving the reorientation of bipolar molecules or displacement of charged particles. The interfacial polarization in heterogeneous media can, also, contribute to the frequency dispersion of the material properties. As a result, the complex relative permittivity, ε_r, of the cell media exhibits multi–relaxation characteristics and can be modeled by using the following Debye–based relationship [85]:

$$\varepsilon(\omega) = \varepsilon'(\omega) - j\varepsilon''(\omega) = \varepsilon_\infty + \sum_{k=1}^{M} \frac{\Delta\varepsilon_k}{1 + j\omega\tau_k}, \tag{2.13}$$

where τ_k and $\Delta\varepsilon_k$ denote the relaxation time and strength relevant to the k–th relaxation process, respectively, M is the number of dielectric relaxation processes occurring in the considered dielectric material, $\omega = 2\pi f$ is the angular frequency, ε_∞ is the asymptotic relative permittivity value at high frequency ($\omega \to \infty$).
In linear dispersive materials, the frequency domain equation relating the electric and polarization fields is [4]:

$$\mathbf{P}(\omega) = [\varepsilon(\omega) - \varepsilon_0]\,\mathbf{E}(\omega) \tag{2.14}$$

where ε_0 denotes the permittivity of free space. By substituting (2.13) in (2.14) and taking the inverse Fourier transform of the resulting equation the following relation is obtained:

$$\sum_{k=1}^{M+1} A_{M+1,k} \frac{\partial^{k-1}\mathbf{P}}{\partial t^{k-1}} = \sum_{k=1}^{M+1} B_{M+1,k} \frac{\partial^{k-1}\mathbf{E}}{\partial t^{k-1}}, \tag{2.15}$$

where the coefficients $A_{M+1,k}, B_{M+1,k}$ are the elements of the following matrix:

$$A = \begin{pmatrix} 1 & 0 & 0 & \dots & 0 \\ 1 & A_{22} & 0 & \dots & 0 \\ 1 & A_{32} & A_{33} & \dots & 0 \\ \vdots & \vdots & \vdots & \dots & \vdots \\ 1 & A_{M+1,2} & A_{M+1,3} & \dots & A_{M+1,M+1} \end{pmatrix}$$

$$B = \begin{pmatrix} 1 & 0 & 0 & \dots & 0 \\ B_{21} & B_{22} & 0 & \dots & 0 \\ B_{31} & B_{32} & B_{33} & \dots & 0 \\ \vdots & \vdots & \vdots & \dots & \vdots \\ B_{M+1,1} & B_{M+1,2} & B_{M+1,3} & \dots & B_{M+1,M+1} \end{pmatrix}$$

and

$$A_{q,2} = \sum_{l=2}^{q} \tau_{l-1} \qquad q = 3, \dots, M+1 \tag{2.16}$$

$$A_{q,q} = \prod_{l=2}^{q} \tau_{l-1} \qquad q = 2, \dots, M+1 \tag{2.17}$$

$$A_{q,p} = A_{q-1,p} + \tau_{q-1} A_{q-1,p-1} \qquad p = 3, \dots, M+1 \quad q = p+1 \tag{2.18}$$

$$B_{q,1} = \sum_{l=2}^{q} \Delta\varepsilon_{l-1} + \varepsilon_\infty - \varepsilon_0 \qquad q = 2, \dots, M+1 \tag{2.19}$$

$$B_{q,q} = \prod_{l=2}^{q} \tau_{l-1} \left(\varepsilon_\infty - \varepsilon_0\right) \qquad q = 2, \dots, M+1 \tag{2.20}$$

$$B_{q,p} = B_{q-1,p} + \tau_{q-1} B_{q-1,p-1} + \Delta\varepsilon_{q-1} c_{q,p} \qquad p = 2, \dots, M \quad q = 1, \dots M+1 \tag{2.21}$$

where

$$c_{q,2} = \sum_{l=1}^{M-1} \tau_l \qquad q = 3,\ldots,M+1 \tag{2.22}$$

$$c_{M+1,p} = c_{M,p} + \tau_{M-1} c_{M,p-1} \qquad p = 3,\ldots,M-1 \tag{2.23}$$

$$c_{M+1,M} = \tau_{M-1} c_{M,M-1} \qquad M > 2 \tag{2.24}$$

By using expression (2.13), it is possible to model accurately the measured permittivity characteristics of a wide variety of biological media upon the proper selection of the multi-relaxation order M and the Debye parameters ε_∞, $\Delta\varepsilon_k$, τ_k.

2.6 PORE MODEL

According to the EP theory of biological membranes, the main cellular response to an externally applied PEF involves the formation of pores in the lipid bilayer membrane [76]. The resulting observable effect is the rapid dynamic increasing of electric conductivity. Moreover, the PEF–induced pores are not distributed uniformly over the membrane surface since they are localized over area experimenting higher TMV. Pore formation is calculated on the basis of the Smoluchowski's equation [76]. Such equation cannot be solved analytically and several parameters, most of which characterized by uncertain values, are involved. Since for short pulse duration (μs - ns), the pore creation process dominates pore expansion, it is possible to assume that pores are created with constant radius of 0.8 nm and the asymptotic model can be employed [4]. Within this framework the dynamic of pore formation and resealing is described by the partial differential equation:

$$\frac{\partial N_{\mathrm{i,j}}}{\partial t} = \alpha e^{\left(\frac{\mathrm{TMV_{i,j}}}{V_{\mathrm{ep}}}\right)^2} \left[1 - \frac{N_{\mathrm{i,j}}}{N_0} e^{-q\left(\frac{\mathrm{TMV_{i,j}}}{V_{ep}}\right)^2}\right] \tag{2.25}$$

where $N_{\mathrm{i,j}}$ is the membrane pore density, α and q are EP parameters, V_{ep} is the characteristic voltage of EP, N_0 is the equilibrium pore density in the nonelectroporated membrane. The membrane conductivity due to EP was evaluated at each time step and spatial coordinate as follows [4, 39]:

$$\sigma_{m\mathrm{i,j}}(x,y,t) = \sigma_m^0 + \mathscr{K} N_{\mathrm{i,j}}(x,y,t)\sigma_p \pi r_p^2 \tag{2.26}$$

where σ_m^0 is the passive membrane conductivity before EP, σ_p and r_p are the internal conductivity and radius of a single pore, respectively, and

$$\mathscr{K} = \frac{e^{\nu_{m\mathrm{i,j}}} - 1}{\dfrac{w_0 e^{w_0 - \eta \nu_{m\mathrm{i,j}}} - \eta \nu_{m\mathrm{i,j}}}{w_0 - \eta \nu_{m\mathrm{i,j}}} e^{\nu_{m\mathrm{i,j}}} - \dfrac{w_0 e^{w_0 + \eta \nu_{m\mathrm{i,j}}} + \eta \nu_{m\mathrm{i,j}}}{w_0 + \eta \nu_{m\mathrm{i,j}}}} \tag{2.27}$$

where w_0 is the energy barrier inside the pore, η is the relative length of pore entrance area, $\nu_{m\mathrm{i,j}} = (q_e/kT)\mathrm{TMV}_{\mathrm{i,j}}$ is the non–dimensional TMV, where q_e is the electron electric charge and k the Boltzmann constant. First of all, the developed model has been validated by comparing the results concerning the spherical cell simulations with the literature ones [4]. As shown in Fig. 2.8, the temporal responses for the dispersive and non-dispersive membrane models are in good agreement with the corresponding curves reported in [4]. As further validation, the results concerning the nucleated spherical cell simulations have been compared with the literature ones [28]. In particular, by an inspection of Fig. 2.9 it is worthwhile to note that the temporal evolution of plasma membrane TMV and pore density are in good agreement with the corresponding ones reported in [28]. The relative discrepancy with the literature results is essentially due to the different adopted electromagnetic model. In the comparison analysis a pore radius $r_p = 3.5$ nm have been considered. Figure 2.9a shows the plasma membrane TMV temporal evolution at the top of the cell ($\theta = 90^\circ$) when a voltage signal having amplitude $E = 2.5$ MV/m, pulse duration $T = 50$ ns, rise time $t_r = 30$ ns and fall time $t_f = 30$ ns is applied to the external electrodes. In figure 2.9b the time behavior of the plasma membrane pore density at the top of the cell is reported when: $E = 15$ kV/cm, pulse duration $T = 50$ ns, rise time $t_r = 18$ ns and fall time $t_f = 18$ ns; $E = 10$ kV/cm, pulse duration $T = 50$ ns, rise time $t_r = 12$ ns and fall time $t_f = 12$ ns.

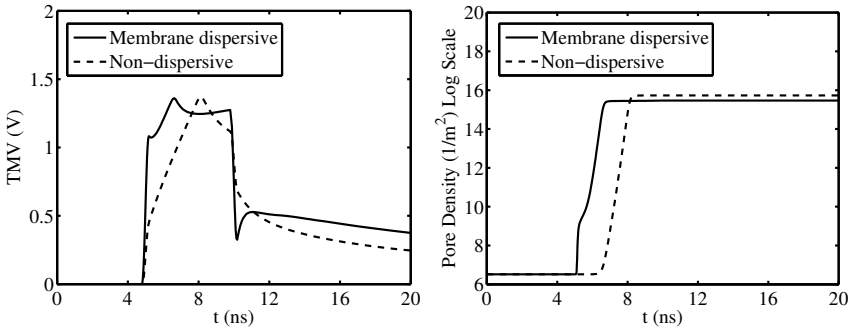

(a) (b)

Figure 2.8: Temporal evolution of (a) TMV and (b) pore density at the top of the cell ($\theta = 90^\circ$) for the dispersive (full curve) and non-dispersive membrane models. Pulse amplitude and duration equal to 50 kV/cm and 5 ns, respectively.

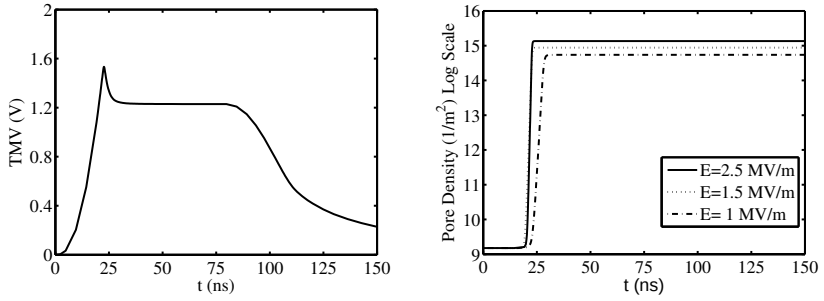

(a) (b)

Figure 2.9: Temporal evolution of (a) plasma membrane TMV at the top of the nucleated spherical cell ($\theta = 90^\circ$) for $r_p = 3.5$ nm. Applied voltage signal having amplitude $E = 25$ kV/cm, pulse duration $T = 50$ ns, rise time $t_r = 30$ ns and fall time $t_f = 30$ ns. Temporal evolution of (b) plasma membrane pore density at the top of the of the nucleated spherical cell ($\theta = 90^\circ$) for $r_p = 3.5$ nm, when three different voltage signals are applied: $E = 25$ kV/cm, pulse duration $T = 50$ ns, rise time $t_r = 30$ ns and fall time $t_f = 30$ ns; $E = 15$ kV/cm, pulse duration $T = 50$ ns, rise time $t_r = 18$ ns and fall time $t_f = 18$ ns; $E = 10$ kV/cm, pulse duration $T = 50$ ns, rise time $t_r = 12$ ns and fall time $t_f = 12$ ns.

Chapter 3

EP IN 2-D IRREGULARLY SHAPED CELLS

3.1 NON-NUCLEATED CELLS MATHEMATICAL MODEL

3.1.1 CELL GEOMETRY MODEL

In this first part of the chapter, a 2-D nonlinear, non-local, dispersive and space-time numerical algorithm has been developed and adopted to evaluate the TMV and pore density along the perimeter of realistic irregular non-nucleated cells [80]. The presented model is based on the Maxwells equations and the asymptotic Smoluchowskis equation describing the pore dynamics. The dielectric dispersion of the media forming the cell has been modeled by using a general multi-relaxation Debye-based formulation. The irregular shape of the cell is described by using the Gielis superformula. Different test cases pertaining to red blood cells, muscular cells, cell in mitosis phase, and cancer-like cell have been investigated. For each type of cell, the influence of the relevant shape, the dielectric properties, and the external electric pulse characteristics on the electroporation process has been analyzed. The numerical results demonstrate that the proposed model is an efficient numerical tool to study the electroporation problem in arbitrary shaped cells.

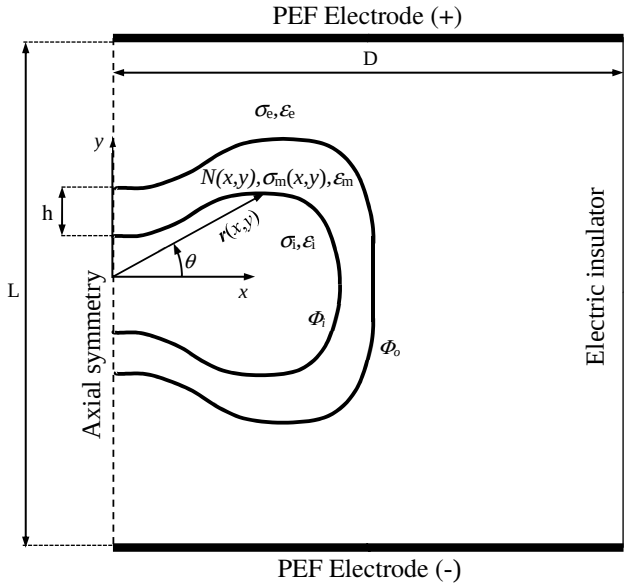

Figure 3.1: Schematic picture of the 2-D axisymmetric arbitrarily shaped cell exposed to uniform pulsed electric field.

As illustrated in Fig. 3.1, the exposure system consists of a cylindrical lossy and dispersive medium, having length L and radius D, containing an arbitrary shaped cell in the middle. The cylinder surface is an electric insulator, and the external PEF source is fixed by using the two parallel–plate electrodes placed at the top and bottom surfaces of the cylinder. The two electrodes are excited in such a way as to generate unipolar and bipolar single or train of pulses. For all the internal boundaries, continuity conditions were set. The duration, rise and fall times, amplitude of the pulse, as well as the number of pulses and their repetition rate have been considered as free parameters. As reported in the previous chapter, the irregular cell shape is described by using the Gielis' formula. In particular, with reference to the 2-D axisymmetric model illustrated in Fig.3.1 the radius vector describing the cell profile is given by:

$$\mathbf{r} = \hat{\mathbf{r}}\sqrt{x^2 + y^2} \tag{3.1}$$

$$x = k_x R(\theta)\cos\theta \tag{3.2}$$

$$y = k_y R(\theta)\sin\theta \tag{3.3}$$

$$R(\theta) = \left(\left| \frac{\cos(m_1\theta/4)}{a_1} \right|^{n_1} + \left| \frac{\sin(m_2\theta/4)}{a_2} \right|^{n_2} \right)^{-\frac{1}{b_1}} \tag{3.4}$$

where $\theta \in [-\pi/2, \pi/2]$ is a convenient angle parameters, $n_p, m_p, b_1 \in \mathbb{R}^+$ (positive real numbers), $p = 1,2$ and $a_p \in \mathbb{R}_0^+$ (strictly positive real numbers), k_x, k_y are the sizing factors. By adjusting the coefficients, many different cell shapes can be generated. Moreover, considering that eq. (3.4) describes the cell shape in parametric form, it is straightforward to generate an additional equidistant offset surface, thus modeling the cell membrane. In particular, to ensure that the offset surface does not intersect the original one the shifting is done along the radial direction.

3.1.2 ELECTROMAGNETIC AND PORE MODEL

For each cell compartment the equation (2.10) is solved numerically using a quasi-static approximations of Maxwell equations, in conjunction with the equations of complex permittivity model and pore model (2.13)–(2.27) and the equation (2.11). In the implemented numerical method, the equations of dielectric relaxation model are specified through a setting of individual coefficients in a system of partial differential equations and associated boundary conditions. The pore density equation has been turned from a differential equation into an integral equation, with a test function as a localized sampling function within the integrand to evaluate the solution. The TMV depends on both space and time coordinates, and it is calculated as the difference between the electric potentials across the boundary surface separating the inside (i) and outside (o) of the cell:

$$\mathrm{TMV}(x,y,t) = \phi_i(x,y,t) - \phi_o(x,y,t) \tag{3.5}$$

In the numerical computation the cell membrane has been directly incorporated in the model and the specific geometrical operator has been used to evaluate the TMV. In general, it allows the computation of a electric potential defined in a point of the destination domain as a function of the electric potential calculated in a point of the source domain. In other words, this operator identifies which point in the source domain corresponds to the point in the destination domain and copies

the electric potential from the source point in the destination point. In the specific case, the operator maps the electric potential from the inner side to the outer side of the membrane and from the outer side to the inner side of the membrane. The used geometrical transformations are described by the following equations:

$$x_o = \frac{x_i}{1 + \frac{h}{\sqrt{{x_i}^2 + {y_i}^2}}} \tag{3.6}$$

$$y_o = \frac{y_i}{1 + \frac{h}{\sqrt{{x_i}^2 + {y_i}^2}}} \tag{3.7}$$

$$x_i = x_o \left(1 + \frac{h}{\sqrt{{x_o}^2 + {y_o}^2}} \right) \tag{3.8}$$

$$y_i = y_o \left(1 + \frac{h}{\sqrt{{x_o}^2 + {y_o}^2}} \right) \tag{3.9}$$

where h is the membrane thickness, x_i and y_i the point coordinates on the inner side of the membrane and x_o and y_o the point coordinates on the outer side of the membrane. However, it can be noticed that the axial symmetry of the system allows for the starting 3–D electromagnetic problem to be addressed by means of a 2-D model, this leading to a significant reduction of the computational burden.

3.1.3 COMPLEX PERMITTIVITY MODEL

The cell membrane and cytoplasmic domains are modeled as lossy and dispersive media. The effect of the dielectric relaxation of the water molecules and dissolved ions forming both cytoplasm and external media is noticeable in the GHz region. For this reason, a first–order Debye equation has been used to model the relevant dielectric response. On the other hand, because of the limited rotational mobility of head-groups of membrane lipids, the dielectric relaxation of the cell membrane occurs in the range of tens to hundreds of MHz. In this case, a second-order Debye equation is more appropriate for describing the material dispersion. In particular, the polarization coefficients given in Table 3.1 have been used in the numerical procedure developed in this study.

Table 3.1: Polarization Vector Coefficients of Cell Membrane, Cytoplasm and External Medium.

Coefficient	Expression
Dielectric relaxation of cell membrane	
A_{31}	1
A_{32}	$\tau_1+\tau_2$
A_{33}	$\tau_1\tau_2$
B_{31}	$\Delta\varepsilon_1+\Delta\varepsilon_2+\varepsilon_\infty-\varepsilon_0$
B_{32}	$\tau_1(\Delta\varepsilon_2+\varepsilon_\infty-\varepsilon_0)+\tau_2(\Delta\varepsilon_1+\varepsilon_\infty-\varepsilon_0)$
B_{33}	$\tau_1\tau_2(\varepsilon_\infty-\varepsilon_0)$
Dielectric relaxation of cytoplasm and external medium	
A_{21}	1
A_{22}	τ
B_{21}	$\Delta\varepsilon+\varepsilon_\infty-\varepsilon_0$
B_{22}	$\tau(\varepsilon_\infty-\varepsilon_0)$

3.2 NUMERICAL RESULTS

Using the numerical model previously described, the EP phenomenon has been studied for different types of cells. In our study, each cell is inserted in a cylinder having length $L = 100$ μm and diameter $D = 100$ μm. In particular, the geometric, electric and EP parameters reported in Table3.2have been used in the numerical procedure developed in this study. Our computations and plots have been performed using MATLAB R2012b. The further model complexity due to the first-order Debye equation for both cytoplasm and external media needs to be taken into account for a valid treatment of EP processes when subnanosecond electric pulses are applied. In fact, by shorting the pulse duration the associated spectral energy becomes significant at frequencies where dispersive effects due to the cytoplasm and external media become important.

Table 3.2: Electric, Geometrical and EP Parameters

Symbol	Value	Description
τ_1	3×10^{-9} s	First relaxation time of membrane [4]
τ_2	4.6×10^{-10} s	Second relaxation time of membrane [4]
τ	6.2×10^{-12} s	Relaxation time of extracellular medium [86] and cytoplasm
$\Delta\varepsilon_1$	2.3×10^{-11} F/m	First relaxation amplitude of membrane [4]
$\Delta\varepsilon_2$	7.4×10^{-12} F/m	Second relaxation amplitude of membrane [4]
$\Delta\varepsilon$	5.9×10^{-10} F/m	Relaxation amplitude of extracellular medium [86] and cytoplasm
ε_∞	13.9×10^{-12} F/m	High frequency permittivity [4]
ε_0	8.85×10^{-12} F/m	Dielectric permittivity of vacuum
ε_{er}	72	Relative permittivity of extracellular medium [4]
ε_{0m}	5	Static relative permittivity of membrane [4]
ε_{cr}	72	Relative permittivity of cytoplasm [4]
σ_e	1.2 S/m	Conductivity of the extracellular medium [4]
σ_m^0	9.5×10^{-9} S/m	Passive conductivity of the membrane [4]
σ_c	0.3 S/m	Conductivity of cytoplasm [4]
σ_p	1.2 S/m	Conductivity of the solution inside the pore
r_p	0.8 nm	Pore radius [4]
α	10^9 m^{-2}s^{-1}	Pore creation rate density [4]
V_{ep}	224 mV	Characteristic voltage of electroporation [4]
N_0	3.3×10^6 m^{-2}	Equilibrium pore density [4]
q	1	Electroporation constant [4]
w_0	3.2	Energy barrier inside the pore [4]
η	0.15	Relative length of pore entrance area [4]
q_e	1.65×10^{-19} C	Electron electric charge
k	1.38×10^{-23} J/K	Boltzmann constant
T	295 K	Temperature

In order to demonstrate such statement some simulations using subnanosecond pulses have been carried out. In particular, fig. 3.2 and 3.3 shows both the TMV and pore density calculated considering the dispersive behavior of the cytoplasm and external media (full curve) and without considering this modification (dotted curve) when the pulse duration is $T = 0.5$ ns. The pulse starts at the time instant $t_{start} = 0.2$ ns and a time window 2 ns long has been used in the computation. The noticeable discordance is a compelling argument for necessarily including more complexity in the model.

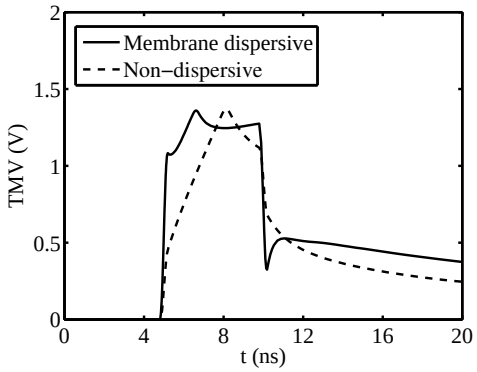

(a)

Figure 3.2: Temporal evolution of TMV at the top of the cell ($\theta = 90^\circ$) for the full dispersive (full curve) and dispersive membrane (dotted curve) models. Pulse amplitude and duration equal to 100 kV/cm and 0.5 ns, respectively.

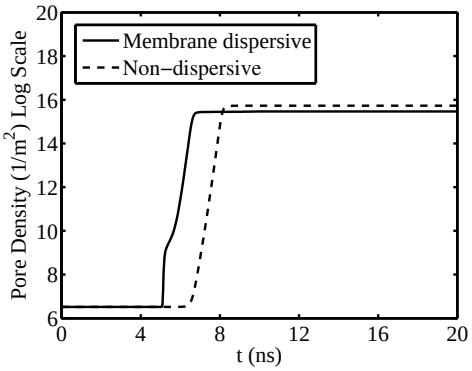

Figure 3.3: Temporal evolution of pore density at the top of the cell ($\theta = 90^\circ$) for the full dispersive (full curve) and dispersive membrane (dotted curve) models. Pulse amplitude and duration equal to 100 kV/cm and 0.5 ns, respectively.

3.2.1 DISCOCYTE RED BLOOD CELLS

The first test case is relevant to a discocyte red blood cells (RBCs). As illustrated in Fig. 3.4, the Gielis formulation allows for an analytical description of the proper discocyte RGB shape that meets size constraints, roundness, aspect ratio, or any sort of shape-related requirement [87]. In particular, the adoption of the Gielis' formula results in an enhanced accuracy of the prediction model, while providing useful flexibility in terms of the underlying numerical procedure especially when parametric investigations have to be carried out. Fig. 3.5(a) and 3.5(b) show the time response of the TMV and pore density at the top of the discocyte RBCs ($\theta = 90^{\circ}$), respectively, for different values of Gielis parameters n_1 and n_2, when a 100 kV/cm PEF having a pulse duration $T = 10$ ns, rise time $t_r = 0.9$ ns, fall time $t_f = 0.9$ ns is applied to the external electrodes. The applied voltage signal is a rectangular pulse, which starts at time instant $t_{start} = 5$ ns and finishes at time instant $t_{end} = 15$ ns. In Fig. 3.5(a) it is worth noticing that the TMV increases with a fast rate. As illustrated in Fig. 3.5(b), the creation of pores generates a rapid increase of the membrane conductivity leading to a decrease of the TMV. Furthermore, an increase of the pore density as the coefficients n_1 and n_2 became larger can be inferred by visual inspection of the same figure. Fig. 3.5(a) shows that at the end of the pulse, the TMV decreases faster when $n_1 = n_2 = 2$. This is mainly due to the fact that for $n_1 = n_2 = 2$ the conductivity of the membrane increases faster than that observed in the other test cases [4]. Fig.3.5(c) shows that the EP opening angle expands for larger values of n_1 and n_2 parameters. Fig.3.6 refers to the RBC characterized by Gielis parameters $n_1 = n_2 = 11$. It can be observed that one nanosecond after the application of the excitation pulse ($t_1 = 6$ ns) a consistent EP emerges, while the EP opening angle increases with the pulse application time, peaking at the end of the voltage pulse ($t_2 = 20$ ns).The influence of the electric field intensity on EP process has been studied, as well. As reported in Fig. 3.7(a) and 3.7(b), the slope of the TMV and the corresponding activation speed of the EP process increase as the electric field amplitude becomes larger.

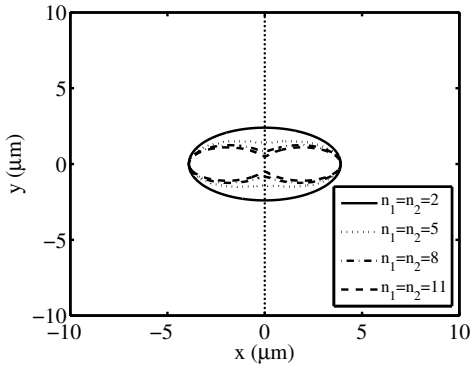

Figure 3.4: Supershaped geometric modeling of discocyte RBCs for different values of n_1 and n_2. Other parameters are $k_x = 3.9$ μm, $k_y = 2.398$ μm, $m_1 = m_2 = 2$, $a_1 = a_2 = 1$ and $b_1 = -2$. Membrane thickness $h = 8$ nm.

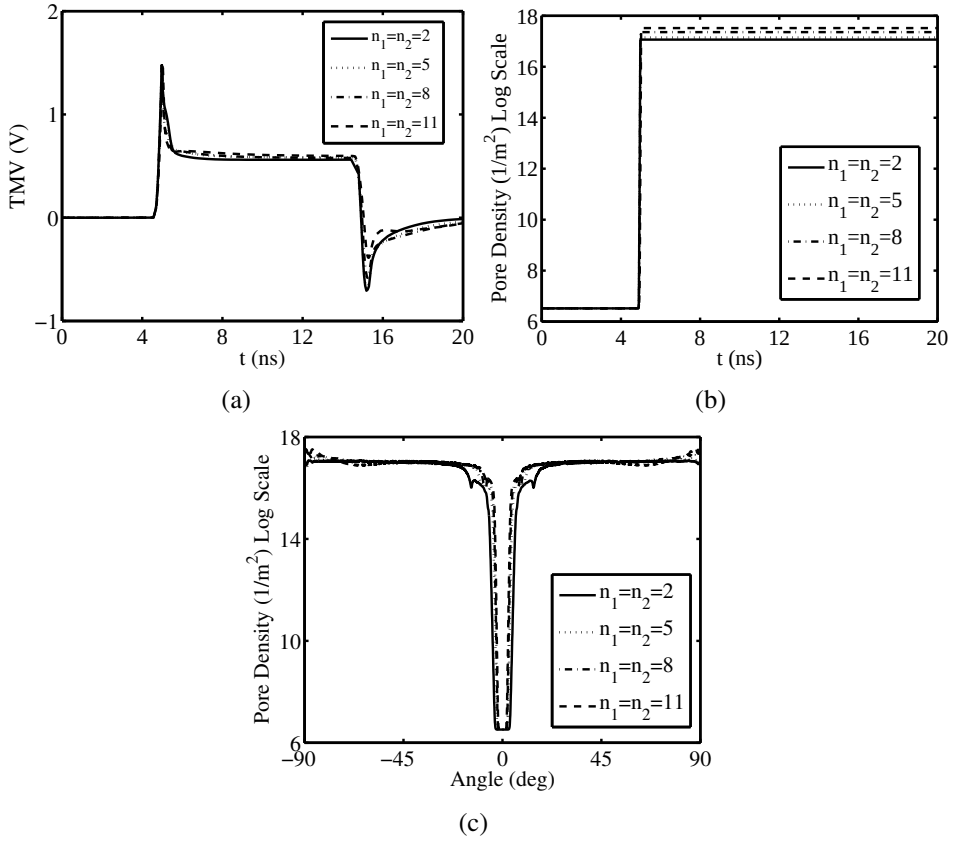

Figure 3.5: Temporal evolution of (a) TMV and (b) pore density at the top of the cell ($\theta = 90°$),(c) pore density versus the polar angle at $t = 20$ ns for different values of n_1 and n_2. Pulse amplitude and duration equal to 100 kV/cm and 10 ns, respectively.

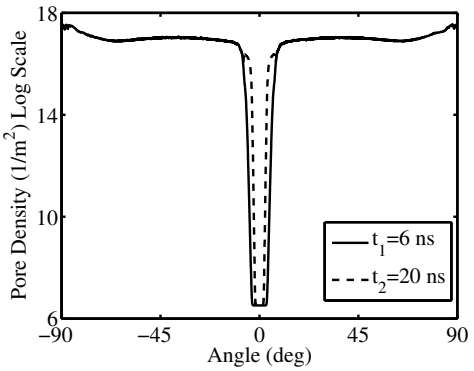

Figure 3.6: Pore density around the cell circumference at different time instants for $n_1 = n_2 = 11$. Pulse amplitude and duration equal to $100\,\mathrm{kV/cm}$ and 10 ns, respectively.

Fig. 3.7(a) shows that for $E = 70\,\mathrm{kV/cm}$ and $t_i \approx 15$ ns the TMV faster decreases quickly by reaching a negative peak value. This occurrence can be explained by considering that an enhancement of the electric field intensity induces a lowering of the membrane time constant. As a consequence, a membrane conductivity improvement and a fast reduction of the TMV occur. At the same time, as shown in Fig. 3.7(b) and Fig. 3.7(c), both the stationary value of the pore density and the EP opening angle grow significantly by increasing the electric field intensity. The EP process depends on the pulse duration, T, and number of applied pulses, N_p. In order to investigate this dependence, an extensive parameter study has been carried out on the RBC with $n_1 = n_2 = 11$.

Fig.3.8 shows the obtained results pertaining the EPRL versus the pulse duration for different value of PE. The EPRL is defined as the ratio between the length of the electroporated area and the total length. When PE is lower than 0.5 mJ, for pulse durations of a few nanoseconds, the EPRL decreases as T becomes larger, and exhibits a deep minimum for $T = 5$ ns. For higher values of T, the EPRL starts to increase reaching a constant value between about 40 and 60 ns and then begins to decrease. This behavior is due to the fact that for $T > 5$ ns, the charging time of the cell membrane, which is of about 10 ns [4], is comparable or smaller than the pulse duration, this leading to a stronger electric field–cell membrane interaction.

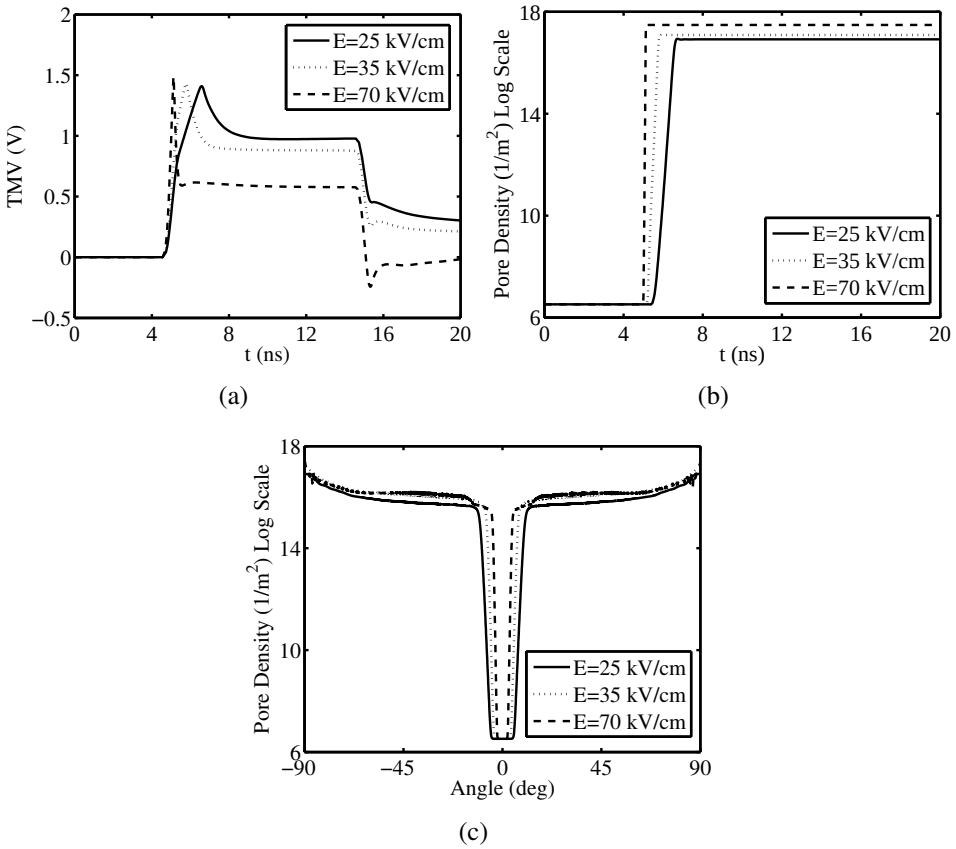

Figure 3.7: Temporal evolution of (a) TMV and (b) pore density at the top of the cell ($\theta = 90°$),(c) pore density versus the polar angle at $t = 5$ ns for different values of electric field intensity. Pulse duration equal to 5 ns, $n_1 = n_2 = 6$.

The saturation and the subsequent decrease of the EPRL can be easily understood by noticing that, for a fixed pulse energy level, the electric field intensity has to be decreased when the pulse duration grows. In contrast to this, at nanosecond and sub–nanosecond regimes, a weaker interaction occurs when the pulse duration decreases. As a result, the EPRL tends to decrease since the applied electric field intensity level falls down. For PE greater than 0.5 mJ, as the applied PEF intensity is high, the cell is strongly electroporated and the minimum at $T = 5$ ns disappears. Fig.3.9, illustrates the minimal electric field intensity versus pulse number that is needed to obtain a pore density of 10^{14} m^{-2}, that is the value of pore density for which the cell membrane is considered to be significantly electroporated [39]. It can be noticed that, moving from an individual pulse to a train of five pulses, the electric field intensity drops from about 9.7 kV/cm to about 5.9 kV/cm. In fact, as shown in Fig. 3.10, by applying a sequence of several consecutive pulses, the TMV gradually increases with a consequent augmentation of the pore density. However, an effective reduction of the pulse intensity can be obtained, also, by using a larger number of pulses and/or by extending the pulse duration.

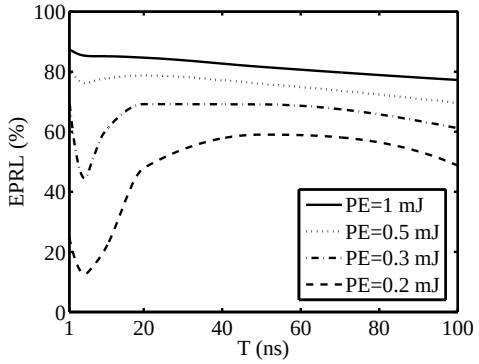

Figure 3.8: EP opening angle versus pulse duration for discocyte RBC with $n_1 = n_2 = 11$.

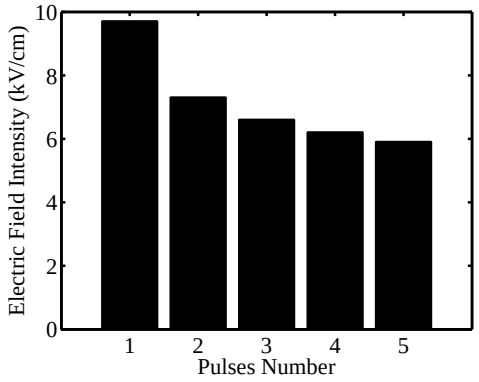

Figure 3.9: Electric field intensity threshold versus pulses number to obtain a pore density of 10^{14} m^{-2}. Pulse duration $T = 10$ ns, discocyte RBC with $n_1 = n_2 = 11$.

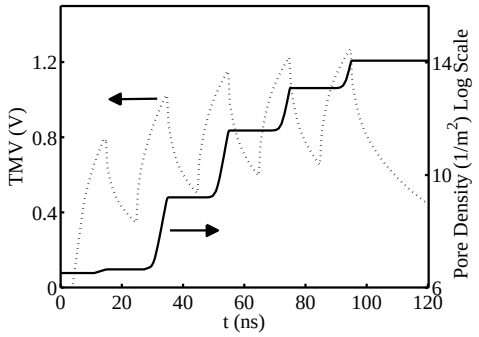

Figure 3.10: Time evolution of TMV and pore density at the top of the discocyte RBC cell ($\theta = \pi/2, n_1 = n_2 = 11$) when a regular sequence of five pulses is applied. Duty cycle 50%, electric field intensity 5.9 kV/cm, repetition time 20 ns.

3.2.2 MUSCULAR–LIKE CELL

The second test case regards the muscular–like cell illustrated in Fig. 3.11. Such kind of cell shape can be well approximated by using the superformula parameters $k_x = 4$ μm, $k_y = 7.5$ μm, $m_1 = m_2 = 2$, $n_1 = n_2 = 0.8$, $a_1 = a_2 = 1$ and $b_1 = 0.6$ [88].

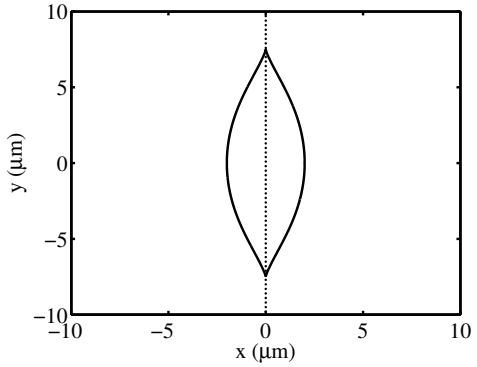

Figure 3.11: Geometric shape of muscular–like cell. Superformula parameters $k_x = 4$ μm, $k_y = 7.5$ μm, $m_1 = m_2 = 2$, $n_1 = n_2 = 0.8$, $a_1 = a_2 = 1$ and $b_1 = 0.6$. Membrane thickness $h = 5$ nm.

Fig. 3.12 shows both the TMV and pore density distributions along the muscle cell perimeter at different time instants, as well as the time–domain behavior of the TMV at different locations on the cell membrane. Because of the complex geometry of the considered cells, the TMV distribution deviates from the cosine law which characterizes spherically shaped cells. As a matter of fact, the electric field minima and maxima along the membrane of the cell strongly depend on its shape. This point can be easily inferred by inspection of Fig. 3.12(a). In particular, for muscle–like cell the TMV reaches its minimum and maximum values at points completely different from the classical -90° and 90° typical of spherical cell models. Furthermore, contrary to what observed in spherical cell models, the EP intensity is negligible at the points along the cell membrane where the PEF electrodes are applied. However, once the EP process starts, the conductivity of the cell membrane rapidly increases and the TMV decreases accordingly. This phenomenon leads to a different angular dependence of the TMV as compared to the one which is observed when the EP is not triggered.

As highlighted in both Fig.3.12(a) and Fig.3.12(b) the EP phenomenon originates within of the flat region of the cell membrane, and gets extinguished at the equatorial ($\theta \approx 0°$) and sharp ($\theta \approx \pm 90°$) zones. Finally, as it appears both in figures 3.12(a) and 3.12(b), the impact of the EP on the TMV distribution becomes particularly noticeable for $t > 14$ ns. The effect of bipolar rectangular pulses on the EP process has been investigated as well. The main numerical results pertaining to TMV and pore density distributions are illustrated in Fig. 3.13. It can be noticed that both the temporal and angular dependence of TMV strongly change as compared to the unipolar excitation (see Fig. 3.12), with a more stable time dependence of the EP opening angle being observed.

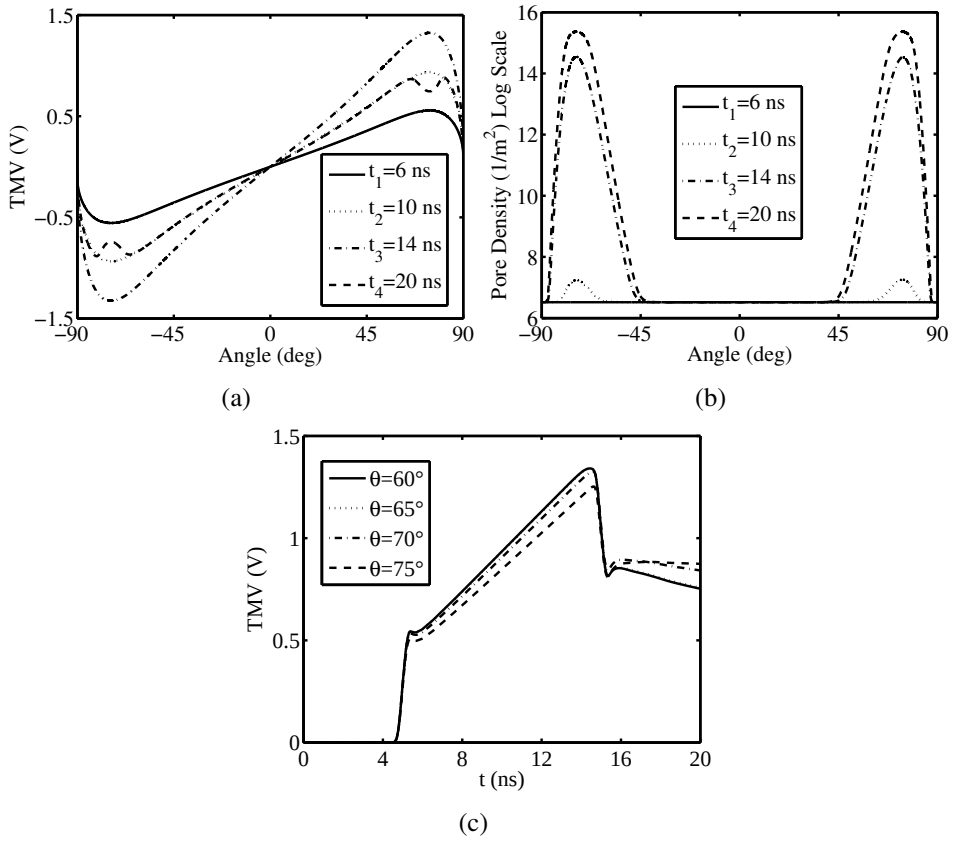

Figure 3.12: (a) TMV and (b) pore density around the cell perimeter for muscular–like cell at different time instants, (c) TMV temporal evolution at different cell membrane placement. Electric field intensity 100 kV/cm, pulse duration $T =$ 10 ns.

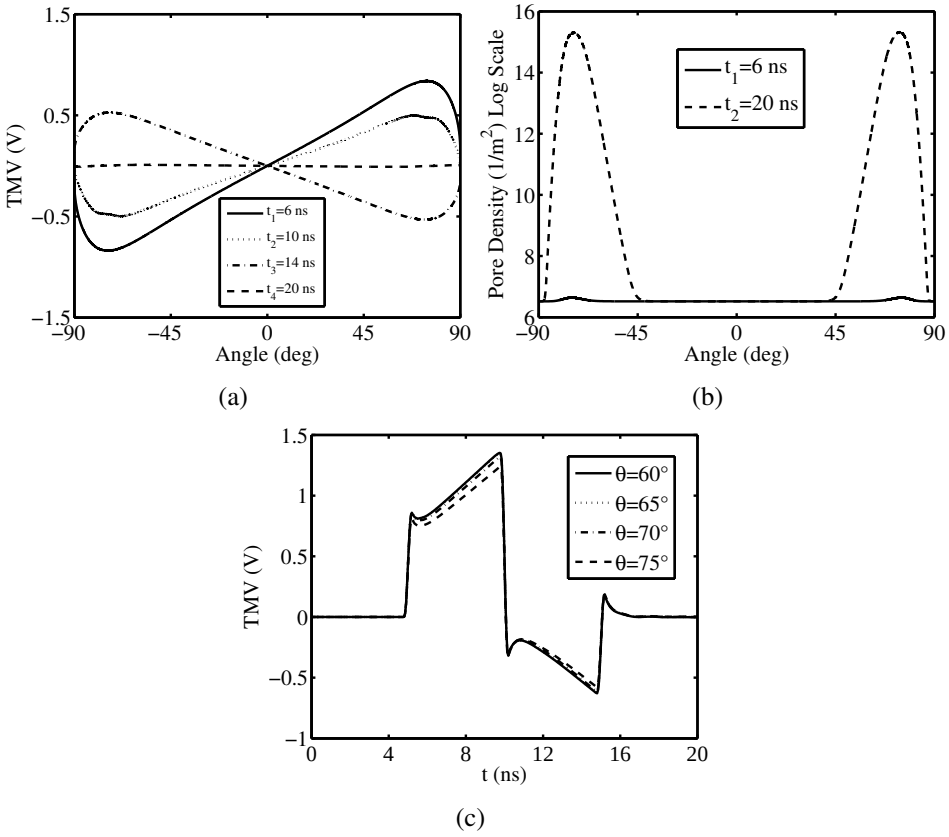

Figure 3.13: (a) TMV and (b) pore density around the cell circumference for muscular–like cell at different time instants, (c) TMV temporal evolution at different cell membrane placement. Rectangular bipolar pulse type, electric field intensity 150 kV/cm, pulse duration $T = 10$ ns.

3.2.3 CELL IN MITOSIS PHASE

The third test case regards the cell in mitosis phase [4], illustrated in Fig. 3.14, which can be well approximated by using the superformula parameters $k_x = k_y =$ 10 µm, $m_1 = m_2 = 2$, $n_1 = n_2 = 1$, $a_1 = a_2 = 1.4$ and $b_1 = -0.2$. For this specific type of cell, the time-domain behavior of the TMV and pore density along the cell perimeter have been calculated (see Fig. 3.15). As shown in the Fig. 3.15(a) and Fig. 3.15(b) the EP does not occur in very limited areas around the angles $\theta = 0^\circ$ and $\theta = \pm 45^\circ$. However, just outside the spot at $\theta = 0^\circ$, the mitosis phenomenon induces a sudden EP. Similarly to what observed in spherical cell models, a noticeable EP process occurs near the cell region next to the electrodes ($\theta = \pm 90^\circ$). Even in the considered case, the irregular cell geometry results in a deviation of the space distribution of the TMV from the cosine law which is observed in spherically shaped cells. In addition to that, one can notice a significant change in the TMV level with respect to the canonical model.

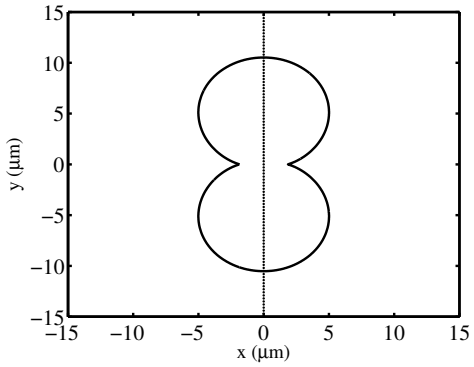

Figure 3.14: Geometric shape of the cell in mitosis phase. Superformula parameters $k_x = k_y = 10$ µm,$m_1 = m_2 = 2$, $n_1 = n_2 = 1$, $a_1 = a_2 = 1.4$ and $b_1 = -0.2$. Membrane thickness $h = 5$ nm.

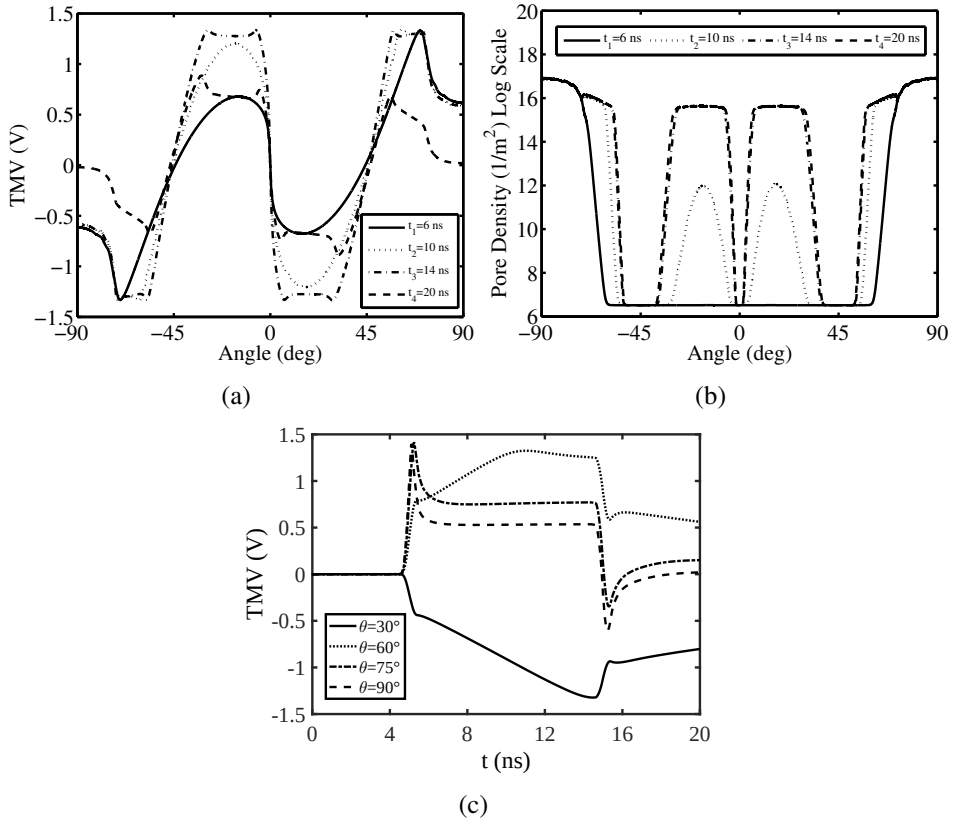

Figure 3.15: (a) TMV and (b) pore density around the cell perimeter for cell in mitosis phase at different time instants, (c) TMV temporal evolution at different cell membrane placement. Rectangular unipolar pulse type, electric field intensity 100 kV/cm, pulse duration $T = 10$ ns.

3.2.4 CANCER CELL

A further test case pertains to a cancer cell [89], approximated by using the super-formula parameters $k_x = k_y = 16.8$ µm, $m_1 = m_2 = 6$, $n_1 = n_2 = 1$, $d_1 = d_2 = 1$ and $b_1 = -2$ (see Fig.3.16). This analysis is relevant as the variation of the dielectric properties of malignant cells with respect to the normal ones has a dramatic impact on the EP characteristics. In particular, an extensive parameter study has been conducted in order to investigate the effect of the cytoplasm conductivity, which is known to become smaller in cancer cells [90]. Fig. 3.17 shows the pore density and the EPRL as a function of the cytoplasm conductivity. It is worth noticing that, for cancer cells (conductivity smaller than $1.2\,\mathrm{S/m}$), both the pore density and EPRL are smaller than those typically observed in normal cells. The decrease of the cytoplasmic conductivity results in the increase of the cytoplasm impedance and, consequently, an increase of the cytoplasm voltage. Since the voltage levels on the extracellular medium and across the cell are constant, the increase of the cytoplasm voltage causes a TMV fall, this leading to a reduced pore density and EP opening angle. Fig. 3.18(a) shows the time response of TMV at the top of cancer cell. As a matter of fact, the increase of the cytoplasm conductivity is driven by an increase of the pore density and membrane conductivity, this causing a reduction of the time constant of the membrane, as well as a subsequent quick drop of the TMV at the end of the PEF signal, when $\sigma_c = 0.3\,\mathrm{S/m}$. Fig. 3.18(b) illustrates the pore density around the cell perimeter for different values of the cytoplasm conductivity. As expected, the pore density and the EPRL increase for larger cytoplasm conductivity values.

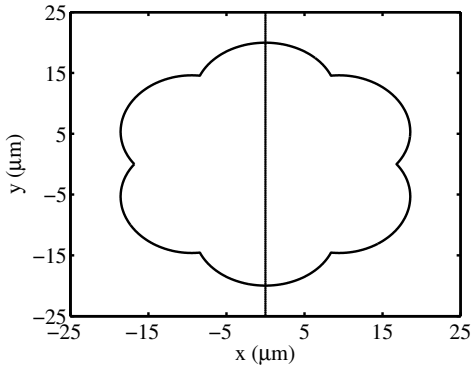

Figure 3.16: Geometric shape of the cancer cell. Superformula parameters $k_x = k_y = 16.8$ μm, $m_1 = m_2 = 6$, $n_1 = n_2 = 1$, $a_1 = a_2 = 1$ and $b_1 = -2$. Membrane thickness $h = 5$ nm.

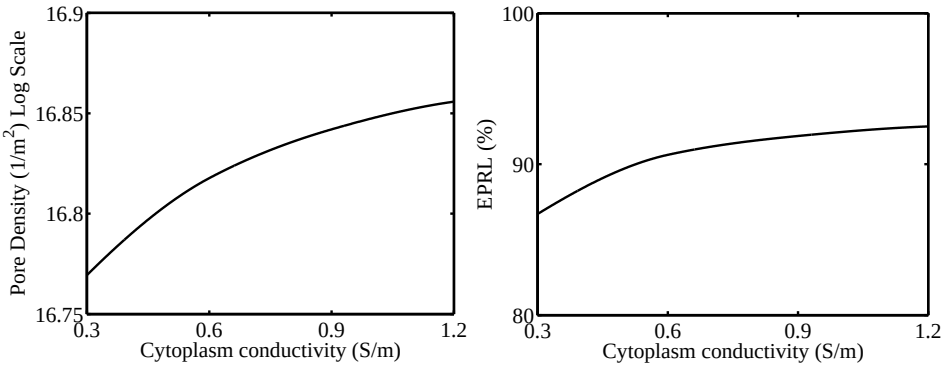

Figure 3.17: (a) Pore density calculated at the top of the cell ($\theta = 90^\circ$) and (b) EP opening angle versus the cytoplasm conductivity. Rectangular unipolar pulse type, electric field intensity 100 kV/cm, pulse duration $T = 10$ ns.

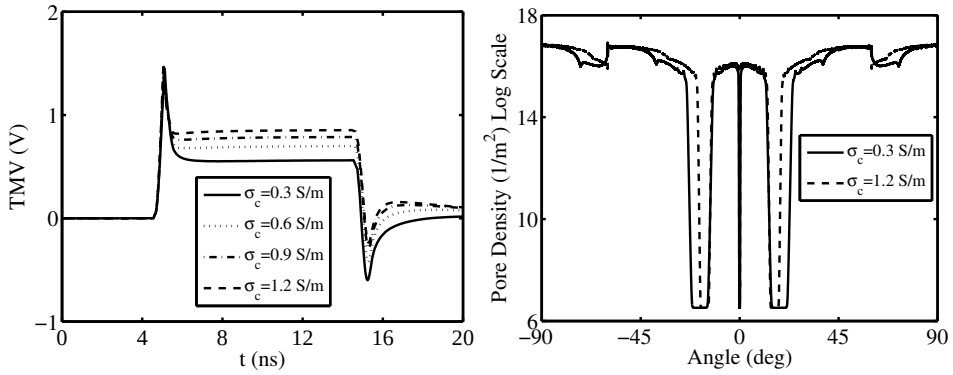

(a) (b)

Figure 3.18: (a) Time evolution of TMV at the top of the cell ($\theta = 90°$) and (b) pore density around the cell perimeter for different values of cytoplasm conductivity. Rectangular unipolar pulse type, electric field intensity 100 kV/cm, pulse duration $T = 10$ ns.

3.2.5 STOMATOCYTE RED BLOOD CELLS

The last test case is relevant to a stomatocyte red blood cells (RBCs), approximated by using the superformula parameters $k_x = 5.31$ μm, $k_y = 0.73$ μm, $m_1 = 8.5$, $m_2 = 1.5$, $n_1 = 143$, $n_2 = 8$, $d_1 = 1$, $d_2 = 0.3$ and $b_1 = 9$ (see Fig. 3.19). In our simulations, the biological cell is exposed to a pulsed electric field having pulse duration, rise and fall time equal to 7 ns, 2 ns and 2 ns, respectively. Moreover, a time delay of 4 ns and a time computational windows of 20 ns are considered. Fig. 3.20 shows the pore density along the cell perimeter at different time instants, considered with respect to $t_0 = 0$ ns. It can be observed that two nanoseconds after the pulse application a consistent electroporation emerges. A significant electroporation can be observed at the bottom and the top of the cell and the non electropored zone is mainly localized around the cell sides.

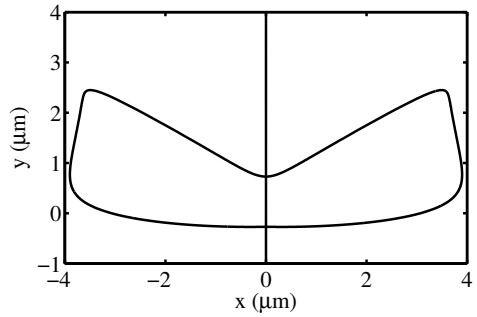

Figure 3.19: Geometric shape of of stomatocyte red blood cell. Superformula parameters $k_x = 5.31$ μm, $k_y = 0.73$ μm, $m_1 = 8.5$, $m_2 = 1.5$, $n_1 = 143$, $n_2 = 8$, $d_1 = 1$, $d_2 = 0.3$ and $b_1 = 9$.

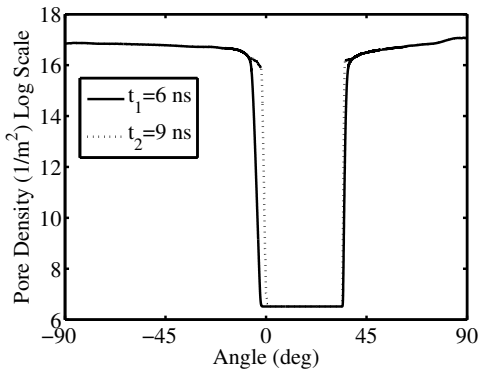

Figure 3.20: Pore density along the cell perimeter at different time, considered with respect to $t_0 = 0$ ns. Applied pulsed electric field having amplitude of 50 kV/cm, duration of 7 ns, rise time $t_r = 2$ ns and fall time $t_f = 2$ ns.

3.3 MATHEMATICAL FORMULATION FOR NUCLEATED CELLS

3.3.1 CELL GEOMETRY MODEL

As illustrated in Fig.3.21, the biological system considered in the proposed studies is an axisymmetric cell constituted by the extracellular electrolyte (Ex), the cytoplasm (Cp), the nucleoplasm (Np), the plasma (Pm) and nuclear (Nm) membranes. The applied pulsed electric field is generated by a couple of ideal planar electrodes placed on the top and lower ends of the computational domain. The irregular cell geometry is modelled by using the Gielis superformula. In particular, the radius vectors describing the nuclear ($\mathbf{r}_1$) and plasma ($\mathbf{r}_2$) membranes are given by:

$$\mathbf{r}_{1,2} = \hat{\mathbf{r}}_{1,2}\sqrt{x^2+y^2} \tag{3.10}$$

$$x_{1,2} = A_{1,2}R_{1,2}(\theta)\cos\theta \tag{3.11}$$

$$y_{1,2} = B_{1,2}R_{1,2}(\theta)\sin\theta \tag{3.12}$$

$$R_1(\theta) = \left(\left|\frac{\cos(m_1\theta/4)}{a_1}\right|^{n_1} + \left|\frac{\sin(m_2\theta/4)}{a_2}\right|^{n_2}\right)^{-\frac{1}{b_1}} \tag{3.13}$$

$$R_2(\theta) = \left(\left|\frac{\cos(m_3\theta/4)}{a_3}\right|^{n_3} + \left|\frac{\sin(m_4\theta/4)}{a_4}\right|^{n_4}\right)^{-\frac{1}{b_2}} \tag{3.14}$$

where $\theta \in [-\pi/2, \pi/2]$, $m_i, n_i, i = 1,...,4$ and $b_j, j = 1,2$ are positive real numbers, $a_p, p = 1,...,4$ are strictly positive real numbers, $A_{1,2}, B_{1,2}$ are suitable scale factors.

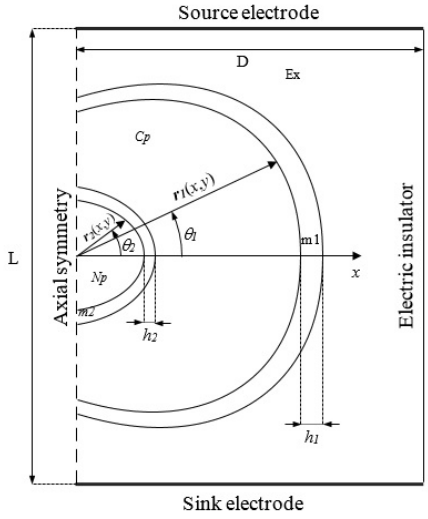

Figure 3.21: Sketch of irregular nucleated biological cell exposed to uniform electric field.

3.3.2 ELECTROMAGNETIC MODEL

The electric potential ϕ and electric field $\mathbf{E}$ are computed under the quasi-static approximation solving in each cell subdomain the Laplace equation:

$$\nabla \cdot \nabla \left(\sigma + \varepsilon_0 \frac{\partial \phi}{\partial t} \right) - \frac{\partial}{\partial t} \nabla \cdot \mathbf{P} = 0 \tag{3.15}$$

in conjunction with the equations of complex permittivity model and pore model, and the equation:

$$\mathbf{E} = -\nabla \phi \tag{3.16}$$

Moreover, the transmembrane voltage is calculated as the difference between the electric potential on the interior (i) and outer (o) sides of the plasma and nuclear membranes:

$$\mathrm{TMV}_{Pm}(x,y,t) = \phi_{i,Pm}(x,y,t) - \phi_{o,Pm}(x,y,t) \tag{3.17}$$

$$\mathrm{TMV}_{Nm}(x,y,t) = \phi_{i,Nm}(x,y,t) - \phi_{o,Nm}(x,y,t) \tag{3.18}$$

where TMV_{Pm} and TMV_{Nm} are the transmembrane voltage for the plasma and nuclear membranes, respectively. In the numerical calculations the plasma and

nuclear membranes have been directly incorporated in the model and the extrusion operator has been used to evaluate the TMV. The extrusion transformation from the interior side to the outer side of the plasma membrane and from the outer side to the inner side of the plasma membrane are described by the following equations:

$$x_o = \frac{x_i}{1 + \frac{h_{Pm}}{\sqrt{{x_i}^2 + {y_i}^2}}} \tag{3.19}$$

$$y_o = \frac{y_i}{1 + \frac{h_{Pm}}{\sqrt{{x_i}^2 + {y_i}^2}}} \tag{3.20}$$

$$x_i = x_o \left(1 + \frac{h_{Pm}}{\sqrt{{x_o}^2 + {y_o}^2}} \right) \tag{3.21}$$

$$y_i = y_o \left(1 + \frac{h_{Pm}}{\sqrt{{x_o}^2 + {y_o}^2}} \right) \tag{3.22}$$

where h_{Pm} is the plasma membrane thickness. While the equations for the extrusion transformations related to the nuclear membrane are:

$$x_o = \frac{x_i}{1 + \frac{h_{Nm}}{\sqrt{{x_i}^2 + (y_i - s)^2}}} \tag{3.23}$$

$$y_o = \frac{(y_i - s)}{1 + \frac{h_{Nm}}{\sqrt{{x_i}^2 + (y_i - s)^2}}} + s \tag{3.24}$$

$$x_i = x_o \left(1 + \frac{h_{Nm}}{\sqrt{{x_o}^2 + (y_o - s)^2}} \right) \tag{3.25}$$

$$y_i = (y_o - s) \left(1 + \frac{h_{Nm}}{\sqrt{{x_o}^2 + (y_o - s)^2}} \right) + s \tag{3.26}$$

where h_{Nm} is the nuclear membrane thickness and s is the nucleus shift respect to the origin along the y direction.

The electrical boundary conditions pertaining to the source and sink electrodes were set to $\phi = V(t)$ and $\phi = 0$, respectively, $V(t)$ being the PEF signal constructed using smoothed piecewise function consisting of unipolar pulse. The study was performed using a direct solver managing a large sparse linear system of equations with good memory efficiency. The solver uses the LU decomposition to compute the system solution and a pre-ordering algorithm that permutes the columns of the system matrix to minimize the number of non-zeros in the L and U factors. A free time-stepping algorithm was utilized to allow the solver to freely select the time steps during the computation.

3.3.3 COMPLEX PERMITTIVITY MODEL

Considering that for several PEF applications the pulse spectral energy becomes significant at frequencies where dispersive effects occur, the developed numerical model takes into account the dielectric relaxation due to the time-dependent response of the dielectric media. In particular, the dielectric properties of cell media are modelled by the Debye dispersion equation:

$$\varepsilon(\omega) = \varepsilon_\infty + \sum_{k=1}^{M} \frac{\Delta\varepsilon_k}{1 + j\omega\tau_k}, \tag{3.27}$$

where ε_∞ is the high frequency permittivity, M is the order of Debye dispersion process, $\Delta\varepsilon_k$ is the k-th relaxation amplitude and τ_k is the k-th relaxation time. In detail, a second order Debye equation is used to model the plasma and nuclear membranes and a first order Debye equation to model the extracellular medium, the cytoplasm and the nucleoplasm. Under the assumption that the coupling between the PEF and the dielectric medium is weak, the linear response approximation will suffice to describe the dielectric polarization. For the homogeneous media characterizing the cell compartments, the linear response of the polarization vectors $\mathbf{P}_1$ and $\mathbf{P}_2$, corresponding to the first and second order Debye dispersion model, to a time-varying electric field can be expressed as:

$$\mathbf{P}_{1,Ex} + \tau_{Ex}\frac{\partial \mathbf{P}_{1,Ex}}{\partial t} = (\Delta\varepsilon_{Ex} + \varepsilon_\infty - \varepsilon_0)\mathbf{E} + (\varepsilon_\infty - \varepsilon_0)\tau_{Ex}\frac{\partial \mathbf{E}}{\partial t} \tag{3.28}$$

$$\mathbf{P}_{1,Cp} + \tau_{Cp}\frac{\partial \mathbf{P}_{1,Cp}}{\partial t} = (\Delta\varepsilon_{Cp} + \varepsilon_\infty - \varepsilon_0)\mathbf{E} + (\varepsilon_\infty - \varepsilon_0)\tau_{Cp}\frac{\partial \mathbf{E}}{\partial t} \tag{3.29}$$

$$\mathbf{P}_{1,Np} + \tau_{Np}\frac{\partial \mathbf{P}_{1,Np}}{\partial t} = (\Delta\varepsilon_{Np} + \varepsilon_\infty - \varepsilon_0)\mathbf{E} + (\varepsilon_\infty - \varepsilon_0)\tau_{Np}\frac{\partial \mathbf{E}}{\partial t} \tag{3.30}$$

$$a_{2,Pm}\frac{\partial^2 \mathbf{P}_{2,Pm}}{\partial t^2} + a_{1,Pm}\frac{\partial \mathbf{P}_{2,Pm}}{\partial t} + \mathbf{P}_{2,Pm} = b_{2,Pm}\frac{\partial^2 \mathbf{E}}{\partial t^2} + b_{1,Pm}\frac{\partial \mathbf{E}}{\partial t} + b_{0,Pm}\mathbf{E} \tag{3.31}$$

$$a_{2,Nm}\frac{\partial^2 \mathbf{P}_{2,Nm}}{\partial t^2} + a_{1,Nm}\frac{\partial \mathbf{P}_{2,Nm}}{\partial t} + \mathbf{P}_{2,Nm} = b_{2,Nm}\frac{\partial^2 \mathbf{E}}{\partial t^2} + b_{1,Nm}\frac{\partial \mathbf{E}}{\partial t} + b_{0,Nm}\mathbf{E} \tag{3.32}$$

where

$$a_{1,Pm} = \tau_{1,Pm} + \tau_{2,Pm} \tag{3.33}$$

$$a_{2,Pm} = \tau_{1,Pm} + \tau_{2,Pm} \tag{3.34}$$

$$b_{0,Pm} = \Delta\varepsilon_{1,Pm} + \Delta\varepsilon_{2,Pm} + \varepsilon_\infty - \varepsilon_0 \tag{3.35}$$

$$b_{1,Pm} = (\Delta\varepsilon_{2,Pm} + \varepsilon_\infty - \varepsilon_0)\tau_{1,Pm} + (\Delta\varepsilon_{1,Pm} + \varepsilon_\infty - \varepsilon_0)\tau_{2,Pm} \tag{3.36}$$

$$b_{2,Pm} = (\varepsilon_\infty - \varepsilon_0)\tau_{1,Pm}\tau_{2,Pm} \tag{3.37}$$

and

$$a_{1,Nm} = \tau_{1,Nm} + \tau_{2,Nm} \tag{3.38}$$

$$a_{2,Nm} = \tau_{1,Nm} + \tau_{2,Nm} \tag{3.39}$$

$$b_{0,Nm} = \Delta\varepsilon_{1,Nm} + \Delta\varepsilon_{2,Nm} + \varepsilon_\infty - \varepsilon_0 \tag{3.40}$$

$$b_{1,Nm} = (\Delta\varepsilon_{2,Nm} + \varepsilon_\infty - \varepsilon_0)\tau_{1,Nm} + (\Delta\varepsilon_{1,Nm} + \varepsilon_\infty - \varepsilon_0)\tau_{2,Nm} \tag{3.41}$$

$$b_{2,Nm} = (\varepsilon_\infty - \varepsilon_0)\tau_{1,Nm}\tau_{2,Nm} \tag{3.42}$$

3.4 PORE MODEL

The pore density number for the plasma, N_{Pm}, nuclear, N_{Nm}, membranes is calculated by using the asymptotic Smoluchowski equation [76]. In particular, the temporal evolutions are described by the following first-order partial differential equations:

$$\frac{\partial N_{Pm}}{\partial t} = \alpha \left[\exp\left(\mathrm{TMV_{Pm}}/\mathrm{V_{ep}}\right)^2 - \frac{N_{\mathrm{Pm}}}{N_{eq}} \right] \tag{3.43}$$

$$\frac{\partial N_{Nm}}{\partial t} = \alpha \left[\exp\left(\mathrm{TMV_{Nm}}/\mathrm{V_{ep}}\right)^2 - \frac{N_{\mathrm{Nm}}}{N_{eq}} \right] \tag{3.44}$$

Whenever the electroporation occurs, the formation of the pores in the cell membranes increases their conductivity. In particular, the average membrane conductivity is given by the sum of static membrane conductivity and the contribution due to the electroporated part:

$$\sigma_{Pm}(x,y,t) = \sigma_{0,Pm} + \mathscr{K}_{Pm} N_{Pm}(x,y,t) \sigma_{Pm} \pi r_p^2 \tag{3.45}$$

$$\sigma_{Nm}(x,y,t) = \sigma_{0,Nm} + \mathscr{K}_{Nm} N_{Nm}(x,y,t) \sigma_{Nm} \pi r_p^2 \tag{3.46}$$

with

$$\mathscr{K}_{Pm} = \frac{e^{v_{Pm}} - 1}{\dfrac{w_0 e^{w_0 - \eta v_{Pm}} - \eta v_{Pm}}{w_0 - \eta v_{Pm}} e^{v_{Pm}} - \dfrac{w_0 e^{w_0 + \eta v_{Pm}} + \eta v_{Pm}}{w_0 + \eta v_{Pm}}} \tag{3.47}$$

$$\mathscr{K}_{Nm} = \frac{e^{v_{Nm}} - 1}{\dfrac{w_0 e^{w_0 - \eta v_{Nm}} - \eta v_{Nm}}{w_0 - \eta v_{Nm}} e^{v_{Nm}} - \dfrac{w_0 e^{w_0 + \eta v_{Nm}} + \eta v_{Nm}}{w_0 + \eta v_{Nm}}} \tag{3.48}$$

where $\sigma_{0,Pm}$ and $\sigma_{0,Nm}$ are the static plasma and nuclear membrane conductivity, $\sigma_{p,Pm}$ and $\sigma_{p,Nm}$ are the conductivity of the solution inside the pore for the plasma and nuclear membranes,v_{Pm} and v_{Nm} are the non-dimensional transmembrane voltage for the plasma and the nuclear membranes calculated using the following equations:

$$v_{Pm} = (q_e/kT) TMV_{Pm} \tag{3.49}$$

$$v_{Nm} = (q_e/kT) TMV_{Nm} \tag{3.50}$$

3.5 NUMERICAL RESULTS

Using the numerical model previously described, the electroporation process has been studied for two types of cells: prolate spheroid and muscular-like. The cells are inserted in a cylindrical computational domain having radius and height equal to 100 μm. Table 3.3 summarizes the polarization, geometric, electric and electroporation parameters used in numerical simulations. Our computations and data plots have been performed using MATLAB suite software.

3.5.1 NUCLEATED PROLATE SPHEROID CELL

The first type of cell has a prolate spheroid shape (see Fig. 3.22a), having semi-axis $a_1 = 2$ μm and $b_1 = 7.5$ μm, for the plasma membrane, and semi-axis $a_2 = 0.75$ μm and $b_2 = 1.5$ μm, for the nuclear membrane. The thickness of plasma and nuclear membranes are $h_Pm = 5$ μm and $h_Nm = 10$ μm, respectively. In our simulations, the biological cells are exposed to a PEF having rectangular shape with amplitude $100\,\mathrm{kV/cm}$, duration $T = 10$ ns, rise time $t_r = 0.9$ ns, and fall time $t_f = 0.9$ ns. All results refer to both plasma dispersive (D_{Pm}) and nuclear dispersive (D_{Nm}) membranes as well as plasma non-dispersive (nD_{Pm}) and nuclear non-dispersive (nD_{Nm}) membrane models. Figures 3.22b-3.22c show the time response of the transmembrane voltage and pore density at the top of the spheroidal cell. In the calculations, we have taken into account that the nuclear envelope consists of two lipid membranes, that we suppose having same electrical properties. Thus, assuming as in [41] that the transmembrane voltage is equally distributed between the two lipid membranes, the TMV across the single membrane is calculated as half of the voltage across the entire nuclear envelope. As shown in figure 3.22b-3.22c, in accordance with results reported in [4] , the increase of the transmembrane voltage and the resulting activation of electroporation occur faster in the dispersive model. The reason is that the membrane time constants of the dispersive model are significantly smaller than that of the non-dispersive one.

Table 3.3: Polarization, Electric, Geometrical and EP Parameters

Symbol	Value	Description
τ_1^{Pm}	3×10^{-9} s	First relaxation time of plasma membrane [4]
τ_1^{Nm}	3×10^{-9} s	First relaxation time of nuclear membrane [4]
τ_2^{Pm}	4.6×10^{-10} s	Second relaxation time of plasma membrane [4]
τ_2^{Nm}	4.6×10^{-10} s	Second relaxation time of plasma membrane [4]
τ_{Ex}	6.2×10^{-12} s	Relaxation time of extracellular medium [86]
τ_{Cp}	6.2×10^{-12} s	Relaxation time of cytoplasm [86]
τ_{Np}	6.2×10^{-12} s	Relaxation time of nucleoplasm [86]
$\Delta\varepsilon_1^{Pm}$	2.3×10^{-11} F/m	First relaxation amplitude of plasma membrane [4]
$\Delta\varepsilon_1^{Nm}$	2.3×10^{-11} F/m	First relaxation amplitude of nuclear membrane [4]
$\Delta\varepsilon_2^{Pm}$	7.4×10^{-12} F/m	Second relaxation amplitude of plasma membrane [4]
$\Delta\varepsilon_2^{Nm}$	7.4×10^{-12} F/m	Second relaxation amplitude of nuclear membrane [4]
$\Delta\varepsilon_{Ex}$	5.9×10^{-10} F/m	Relaxation amplitude of extracellular medium [86]
$\Delta\varepsilon_{Cp}$	5.9×10^{-10} F/m	Relaxation amplitude of cytoplasm [86]
$\Delta\varepsilon_{Np}$	5.9×10^{-10} F/m	Relaxation amplitude of nucleoplasm [86]
ε_∞	13.9×10^{-12} F/m	High frequency permittivity [4]
ε_0	8.85×10^{-12} F/m	Dielectric permittivity of vacuum
ε_e^{Ex}	72	Relative permittivity of extracellular medium [4]
ε_0^{Pm}	5	Static relative permittivity of plasma membrane [4]
ε_e^{Cp}	72	Relative permittivity of cytoplasm [4]
ε_0^{Nm}	7	Static relative permittivity of nuclear membrane [4]
ε_e^{Np}	72	Relative permittivity of nucleoplasm [4]
σ_{Ex}	1.2 S/m	Conductivity of the extracellular medium [4]
σ_0^{Pm}	9.5×10^{-9} S/m	Passive Conductivity of the plasma membrane [4]
σ_{Cp}	0.3 S/m	Conductivity of cytoplasm [4]
σ_0^{Nm}	1×10^{-4} S/m	Passive Conductivity of the nuclear membrane[41]
σ^{Np}	0.6 S/m	Conductivity of nucleoplasm[41]
σ_p^{Pm}	0.6492 S/m	Conductivity of solution inside the pore for plasma membrane [41]
σ_p^{Nm}	0.4328 S/m	Conductivity of solution inside the pore for nuclear membrane [41]
r_p	0.8 nm	Pore radius [4]
α	10^9 m^{-2}s^{-1}	Pore creation rate density [4]
V_{ep}	224 mV	Characteristic voltage of electroporation [4]
N_{eq}	3.3×10^6 m^{-2}	Equilibrium pore density [4]
w_0	3.2	Energy barrier inside the pore [4]
η	0.15	Relative length of pore entrance area [4]
q_e	1.65×10^{-19} C	Electron electric charge
k	1.38×10^{-23} J/K	Boltzmann constant
T	295 K	Temperature
h_{Pm}	5 nm	Plasma membrane thickness[41]
h_{Nm}	10 nm	Nuclear membrane thickness[41]

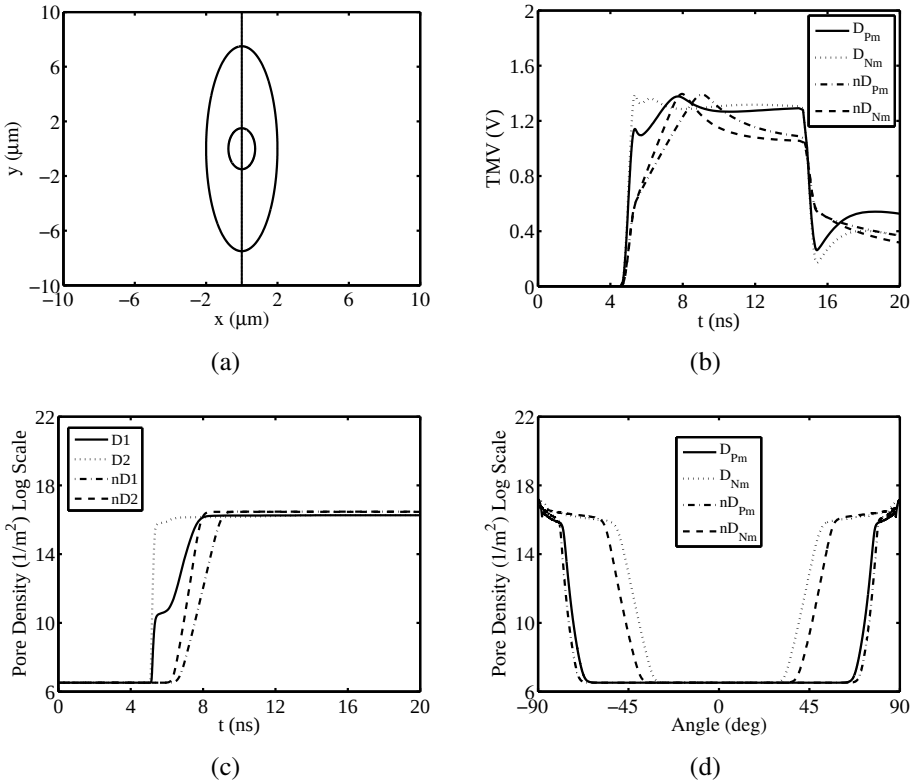

Figure 3.22: Nucleated biological cell with prolate spheroidal shape (a), results for plasma (Pm) and nuclear (Nm) membranes obtained using the dispersive (D) and non-dispersive (nD) model: (b) Temporal evolution of TMV and (c) pore density at the top of the cell ($\theta = 90°$), (d) pore density versus the polar angle at $t = 20$ ns. Pulse amplitude and duration equal to 100 kV/cm and 10 ns, respectively.

However, the increase of pore density in the plasma and nuclear membranes, generates a fast increase of membranes conductivity leading to a decrease of the transmembrane voltage. In contrast to non-dispersive model, in dispersive one the nuclear membrane is electroporated before the plasma membrane. For both the dispersive and non-dispersive models, the nuclear membrane is electroporated before the plasma membrane. The explanation of this phenomenon is related to the fact that the charging time constant of nuclear membrane is less than that of the plasma membrane [91] . This effect is more evident when shorter pulses are used, as in our case. Figure 3.22d reports the pore density around the cell circumference at time instant $t = 20$ ns and a relevant difference is evaluated between the dispersive and non-dispersive model.

In particular, the electroporation relative length (EPRL), i.e. the ratio between the length of the electroporated area and the total length of the cell membrane, pertaining the plasma membrane and calculated using the dispersive model is about 2.5 % higher than that calculated using non-dispersive one. Moreover, the EPRL of the nuclear membrane calculated using the dispersive model is about 7.3 % higher than that calculated using non-dispersive one. To evaluate the EPRL, the cell membranes are considered to be significantly electroporated when the pore density reaches a value of 10^{14} m^{-2} [39] .

3.5.2 NUCLEATED MUSCULAR-LIKE CELL

The second analyzed nucleated cell is the muscular-like reported in Fig.3.23a. For this type of cell, the shape of the plasma membrane has been modelled using the Gielis superformula parameter $m_1 = m_2$, $n_1 = n_2 = 0.8$, $d_1 = d_2 = 1$, $b_1 = 0.6$ [80] . The spatial scale factors are $A_1 = 4$ μm and $B_1 = 7.5$ μm. The nucleus has prolate spheroid shape with semi-axis $a_2 = 0.75$ μm and $b_2 = 1.5$ μm and center shifted of $s = 1$ μm respect to the origin. Figures 3.23b and 3.23c show the time response of the TMV and pore density at the angular place $\theta = 75^\circ$ for both plasma and nuclear membranes, obtained using the dispersive and non-dispersive model. Also in this case, the activation of electroporation occurs faster in the dispersive model. In contrast to the nucleated prolate spheroidal cell, for nucleated muscular-like cell the nuclear membrane is electroporated before the plasma membrane for both the dispersive and non-dispersive model. In agreement with the nucleated prolate spheroidal cell, also for nucleated muscular-like cell the nuclear membrane is electroporated before the plasma membrane for both the dispersive and non-dispersive model. As reported in Figures 3.23c and 3.23d, a significant difference is evaluated between the two analyzed models. For this type of cell, the difference between the two used models is accentuated by the irregular geometrical shape of the plasma membrane. At $\theta = 75^\circ$, considering the dispersive model, both plasma and nuclear membranes are electroporated. In contrast, in the non-dispersive model, only the nuclear membrane is significantly electroporated. At $\theta = 75^\circ$, considering the dispersive and non-dispersive models, only the nuclear membrane is significantly electroporated.

From figure 3.23d it can be inferred a significant absolute difference between the dispersive and non-dispersive EPRL for both the membranes. In particular, the EPRL difference is about 26.7 %, for the plasma membrane, and about 7.1 %, for the nuclear membrane.

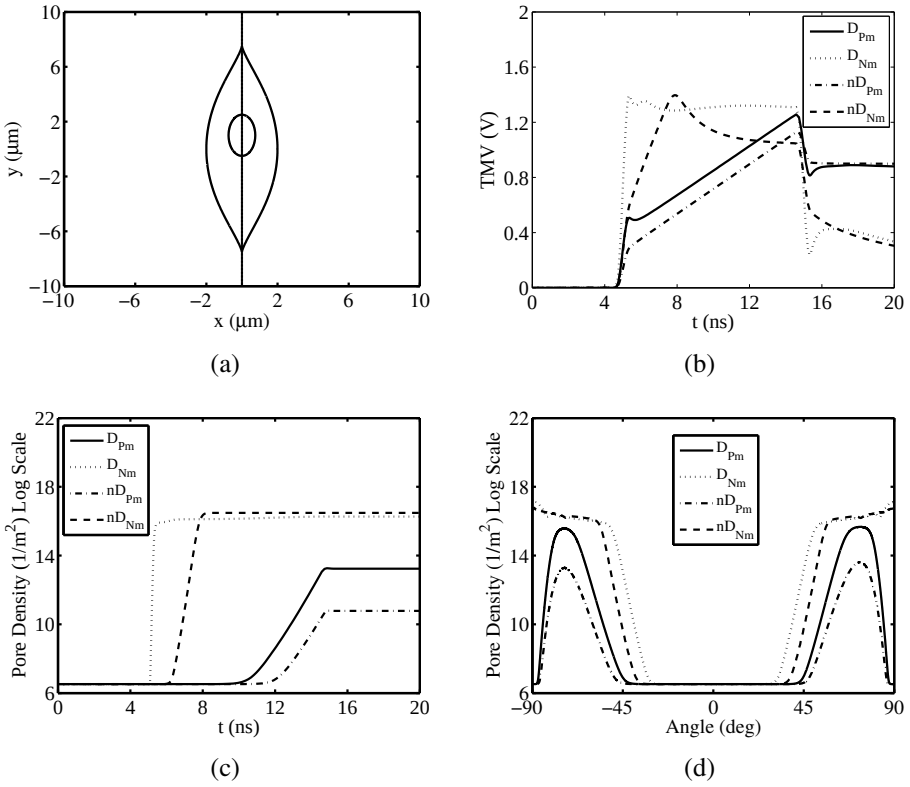

Figure 3.23: Smooth muscular cell with decentralized nucleus (a), results for plasma (Pm) and nuclear (Nm) membranes obtained using the dispersive (D) and non-dispersive (nD) model: (b) Temporal evolution of TMV and (c) pore density for $\theta = 75^\circ$, (d) pore density versus the polar angle at $t = 20$ ns. Pulse amplitude and duration equal to 100 kV/cm and 10 ns, respectively.

3.5.3 NUCLEUS DECENTRALIZATION STUDY

To investigate the influence of the nucleus shift on the EP process, a parametric study has been carried out. Also in this case, the analysis has been performed for plasma and nuclear membranes, using both the dispersive and non-dispersive model. Figures 3.24a and 3.24b illustrate, respectively, the EPRL for plasma and nuclear membranes as functions of the nucleus shift s, calculated using the dispersive (D) and non-dispersive (nD) model. The plasma EPRL calculated using the dispersive model changes within a limited values ranging from 25 % to 27 %. Instead the plasma EPRL evaluated using the non-dispersive model is zero for s ranging from -1.5 µm to 1.5 µm and it increases to about 8 % moving the nucleus towards the electrodes. For the nuclear membranes the EPRL calculated using the dispersive and non-dispersive model is quite constant and equal to about 58 % and 51 %, respectively. As showed in figure 3.24c, the absolute difference between EPRL of plasma membrane calculated using the dispersive and non-dispersive models has a minimum of about 17.2 % at $s = \pm 3$ µm reaching the maximum value of about 27.2 % close to $s = \pm 1.5$ µm. A local minimum of about 25.8 % is evident at $s = 0$ µm. Figure 3.24d shows that for the nuclear membrane, the absolute difference between the dispersive and non-dispersive EPRL change in the range 7 % - 7.3 %.

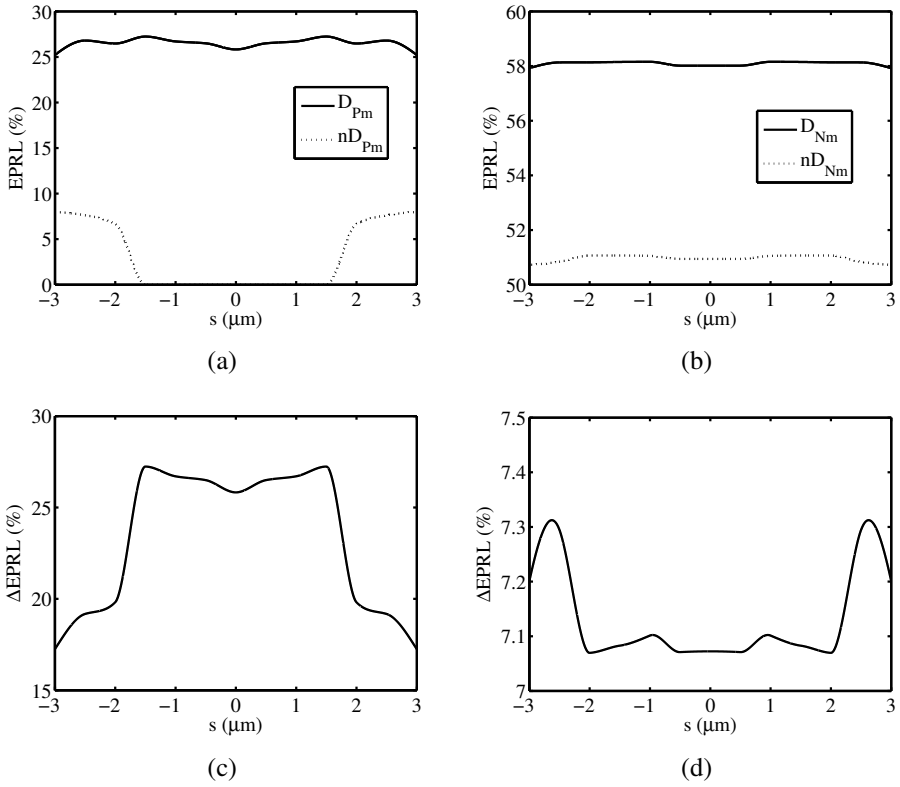

Figure 3.24: Nucleus decentralization parametric study: (a) EPRL for plasma membrane (Pm) and (b) EPRL for nuclear membrane (Nm) versus the nucleus decentralization parameter s, obtained using the dispersive (D) and non-dispersive (nD) model. Absolute difference between the dispersive and non-dispersive EPRL versus the nucleus decentralization parameter s for (c) plasma membrane and for (d) nuclear membrane.

Chapter 4

EP IN MULTIPLE IRREGULAR CELLS SYSTEMS

4.1 2-D EP MULTIPLE CELLS MODEL

Most of the electroporation process studies are based on models using a single isolated cell with a circular or elliptical shape. In order to provide a predictive description of in vitro experiments, a nonlinear dispersive numerical model describing the irregularly cells shape and the effects of each cell on the neighbors has been developed. In this paragraph, the EP process induced by PEFs in multiple irregularly shaped cells systems has been analyzed. Using the numerical model described in Chapter 2, the electroporation process has been studied for two types of multiple irregularly shaped cells systems: packed system (Fig. 4.1) and sparse system (Fig. 4.2). Each multiple irregularly shaped cells system is constituted by 7 nucleated muscular-like cells. For this kind of cell, the geometric shape of the plasma membrane is modelled by using the Gielis' superformula parameters $A_1 = 4$ μm, $B_1 = 7.5$ μm, $m_1 = m_2 = 2$, $n_1 = n_2 = 0.8$, $a_1 = a_2 = 1$ and $b_1 = 0.6$. The nucleus has a prolate spheroid shape with semi-axis $A_2 = 0.75$ μm and $B_2 = 1.5$ μm and it is centered in the middle of each cell. Table 4.1 and 4.2 report the space position of each cell with respect to the origin for the packed and the sparse system, respectively.

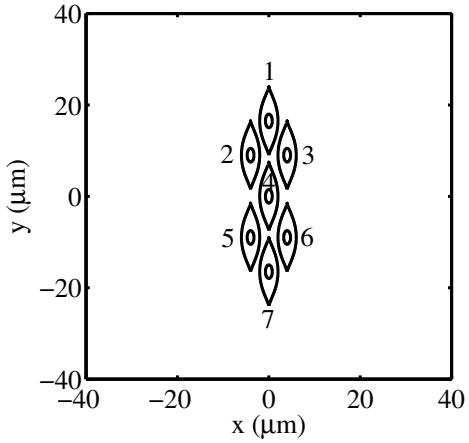

Figure 4.1: Multiple irregularly shaped cells packed system.

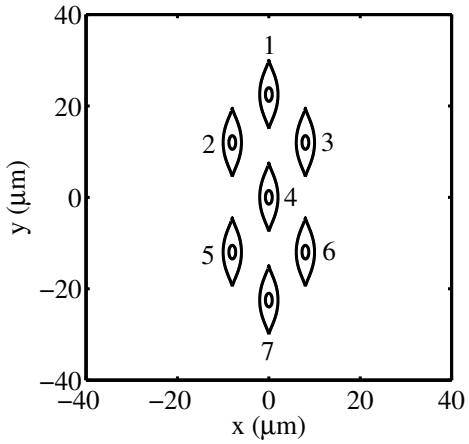

Figure 4.2: Multiple irregularly shaped cells sparse system.

Table 4.1: Packed System Cells Space Position

CELL	x (μm)	y (μm)
1	0	16.5
2	-4	9
3	4	9
4	0	0
5	-4	-9
6	4	-9
7	0	-16.5

Table 4.2: Sparse System Cells Space Position

CELL	x (μm)	y (μm)
1	0	22.5
2	-8	12
3	8	12
4	0	0
5	-8	-12
6	8	-12
7	0	-22.5

4.1.1 NUMERICAL RESULTS

In our study, each cells system is inserted in a cylinder domain having radius and height equal to 100 μm. The polarization, geometric, electric and electroporation parameters used in the numerical procedure are summarized in table 3.3. In the simulations, the biological systems are exposed to a PEF having rectangular shape with amplitude $E = 100\,\mathrm{kV/cm}$, duration $T = 10$ ns, rise time $t_r = 0.9$ ns and fall time $t_f = 0.9$ ns. Figure 4.3 shows the time response of the TMV and pore density at the angular place $\theta = 75^\circ$ for both plasma and nuclear membranes, obtained for the packed system. As consequence of the external pulse application, the transmembrane voltage on plasma and nuclear membranes on each cell increase approximately to 1.4 V. As shown in Fig. 4.3, the increase of transmembrane voltage and the resulting activation of electroporation occurs faster in the nuclear membranes. This effect is more evident when shorter pulses are used, as in our case.

In the present discussion, the cells membranes are considered to be significantly electroporated when the pore density reaches a value of 10^{14} m^{-2} [39]. As reported in Fig. 4.3b, the plasma membrane of each cell is electroporate with exception of the plasma membrane of cell 5, that in the point of evaluation is affected by the shielding effect of the other cells. Furthermore, the activation of electroporation for the plasma membranes of each cell occurs in different time instants, resulting in the following sequence of EP activation: cell 7 and cell 6, cell 2, cell 3, cell 4, cell 1, cell 5 (no EP). Instead, from Fig. 4.3d it can be inferred that the nuclear membranes are all significantly electroporated at the same time instant.

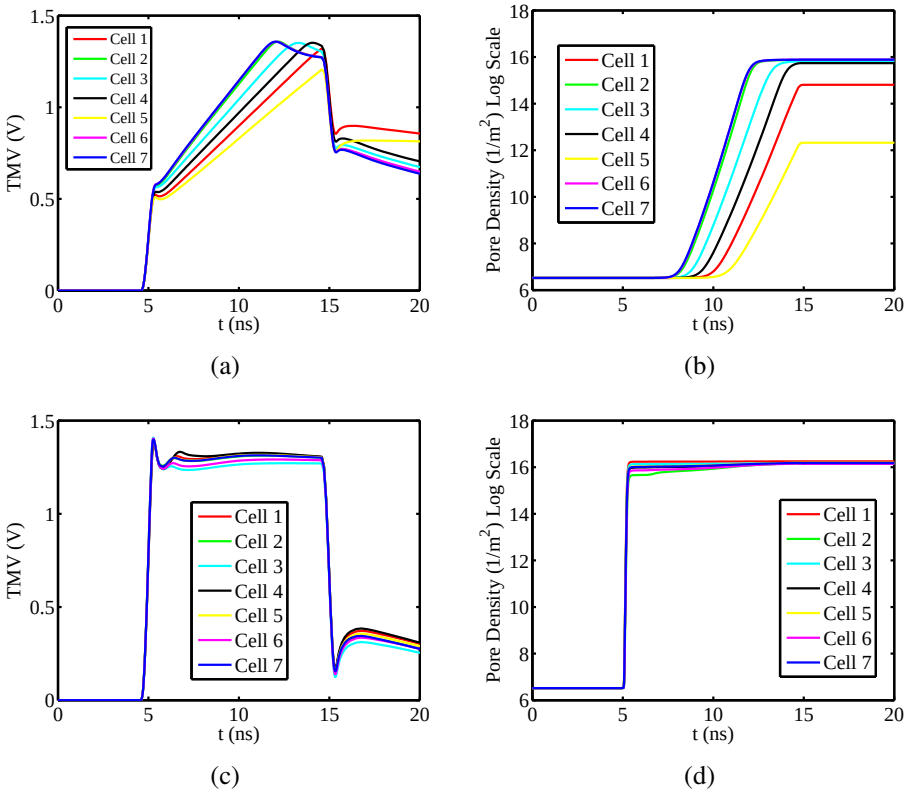

Figure 4.3: Packed System - Temporal evolution for plasma membranes (Pm) of (a) TMV and (b) pore density for $\theta = 75°$. Temporal evolution for nuclear membranes (Nm) of (c) TMV and (d) pore density for $\theta = 75°$. Pulse amplitude and duration equal to 100 kV/cm and 10 ns.

Fig. 4.4 and 4.5 report the pore density versus the polar angle at time instant $t = 20$ ns for the plasma and the nuclear membranes of each cell, respectively. As reported in Fig. 4.4, the EP process originates within of the smoothed region of the plasma membrane of each cell, and gets estinguished at the equatorial ($\theta = 0^\circ$ and $\theta = \pm 180^\circ$) and sharp ($\theta = \pm 90^\circ$) zones. In particular, the electroporation relative length (EPRL) of the plasma membranes of cell 1, cell 2, cell 3, cell 5, cell 6 and cell 7 is about 37 % (Tab. 4.3). As show in Fig. 4.4, for these cells the pore density around the plasma perimeter has an asymmetric distribution due to the electric interaction of each cell with the neighboring ones. Differently, as reported in Fig. 4.4d the plasma membrane pore density versus the polar angle for cell 4 has a symmetric distribution due to its centric placement in the whole system. For this cell the plasma EPRL is equal to 24.22 %. As reported in Fig. 4.5, the EP phenomenon is maximum at the top and the bottom of the nuclear membranes ($\theta = \pm 90^\circ$) of each cell, and estinguishes at the equatorial ($\theta = 0^\circ$ and $\theta = \pm 180^\circ$). The nuclear EPRL of cell 1 and cell 7 is about 56.5 %. Furthermore the nuclear EPRL of cell 2, cell 3, cell 5 and cell 6 is about 58 %. As shown in Fig. 4.5, the distribution around the nuclear membrane pore density is symmetric only for cell 4, having a nuclear EPRL of 53.56 %.

Table 4.3: Packed System EPRL

CELL	PLASMA EPRL %	NUCLEAR EPRL %
1	37.42	56.50
2	37.46	58.24
3	37.34	58.25
4	24.22	53.56
5	37.51	58.24
6	37.46	58.24
7	37.61	56.55

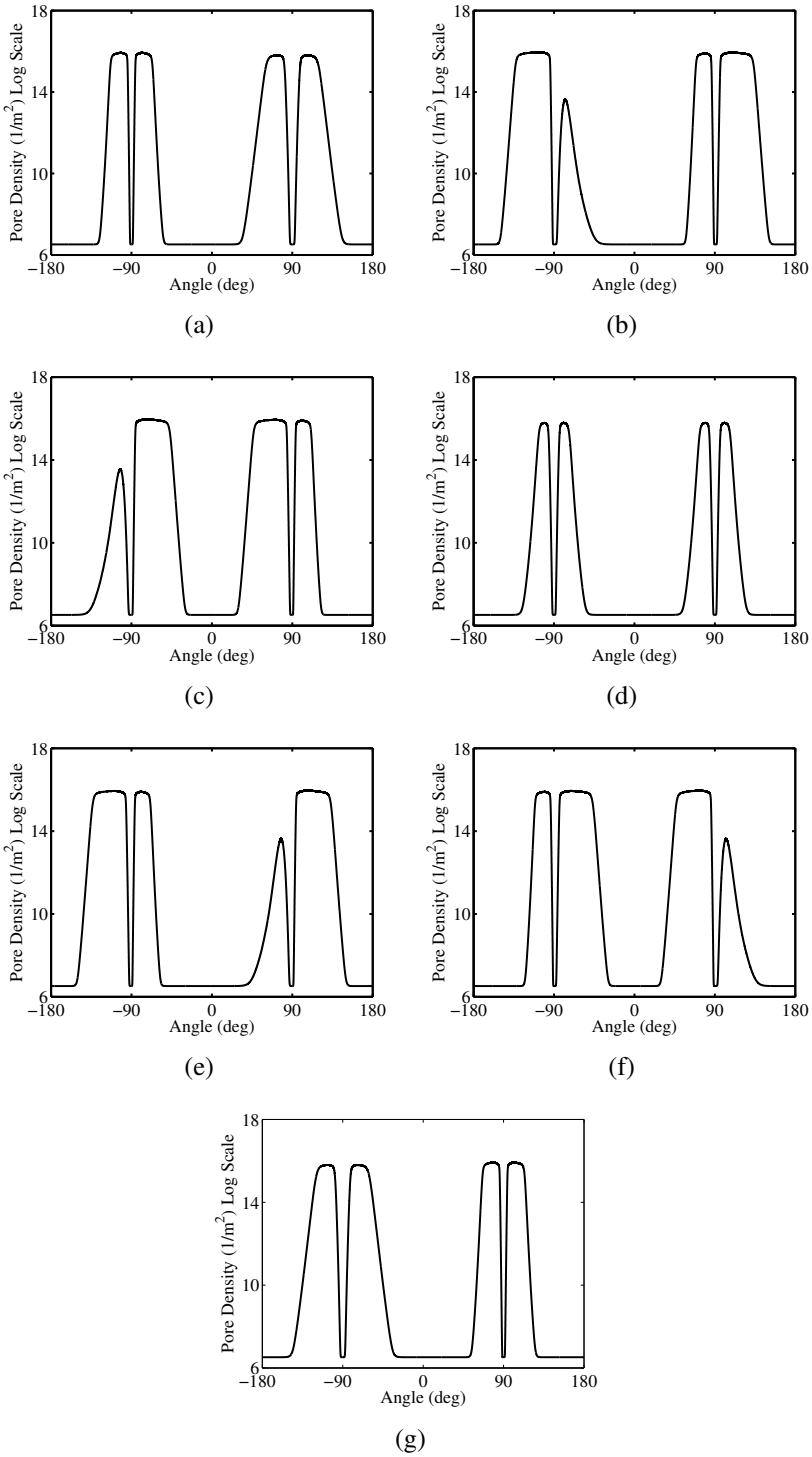

Figure 4.4: Packed System - Plasma membranes (Pm) pore density versus the polar angle at time instant $t = 20$ ns for cell 1 (a), cell 2 (b), cell 3 (c), cell 4 (d), cell 5 (e), cell 6 (f), cell 7 (g). Pulse amplitude and duration equal to 100 kV/cm and 10 ns.

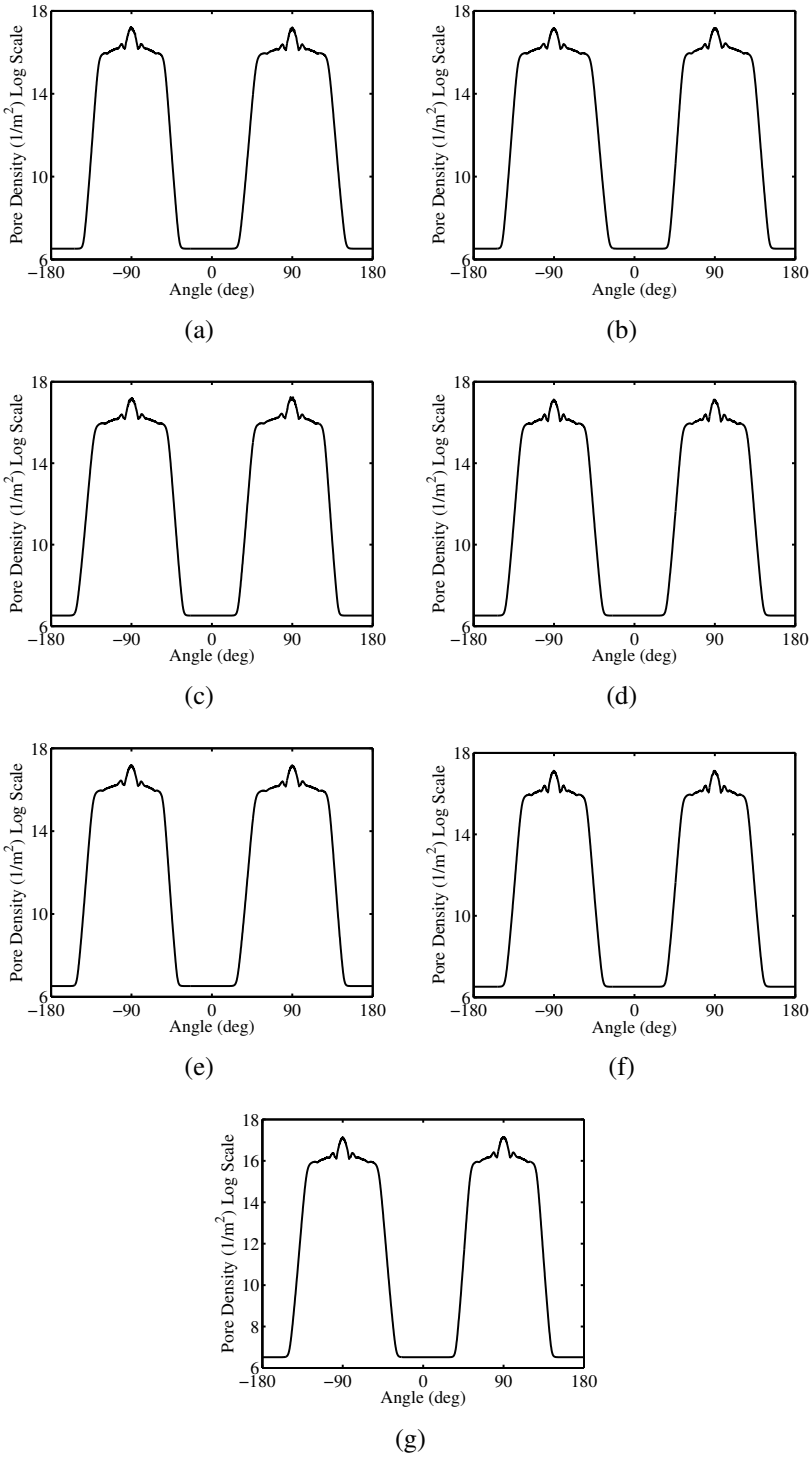

Figure 4.5: Packed System - Nuclear membranes (Nm) pore density versus the polar angle at time instant $t = 20$ ns for cell 1 (a), cell 2 (b), cell 3 (c), cell 4 (d), cell 5 (e), cell 6 (f), cell 7 (g). Pulse amplitude and duration equal to 100 kV/cm and 10 ns.

Fig. 4.6 shows the temporal evolution for plasma and nuclear membranes of TMV and pore density for ($\theta = 75^{\circ}$), obtained for the sparse system. Also in this case, the increase of TMV and the resulting activation of EP occurs faster in the nuclear membranes. As shown in Fig. 4.6b, the plasma membrane of each cell is electroporated in different time instants, resulting in the following new sequence of EP activation: cell 6, cell 3, cell 7, cell 4, cell 2, cell 1, cell 5. Also in these case, the nuclear membranes are significantly electroporated at the same EP activation time instant. Fig. 4.7 and Fig. 4.8 report the plasma and the nuclear membrane pore density versus the polar angle at time instant $t = 20$ ns. In particular, the EPRL (Tab. 4.4) of the plasma membranes of cell 1 and cell 7 is about 47 %. The EPRL of plasma membranes of cell 2, cell 3, cell 5 and cell 6 is about 48.7 %, and the EPRL of cell 4 is 44.78 %. Furthermore, the nuclear EPRL of cell 1 and cell 7 is about 58 %, the nuclear EPRL of cell 2, cell 3, cell 5 and cell 6 is about 58.8 %, and the nuclear EPRL of cell 4 is 57.57 %. Also in this case, cell 4 is the only cell to have a symmetric distribution of plasma and nuclear membrane pore density along the membranes circumference. In conclusion, the electroporation process is more evident in the sparse system than in the packed one. This occurrence is essentially due to the shielding effect of each cell on the others.

Table 4.4: Sparse System EPRL

CELL	PLASMA EPRL %	NUCLEAR EPRL %
1	47.22	58.14
2	48.72	58.82
3	48.67	58.82
4	47.78	57.57
5	48.73	58.82
6	48.72	58.82
7	47.40	58.14

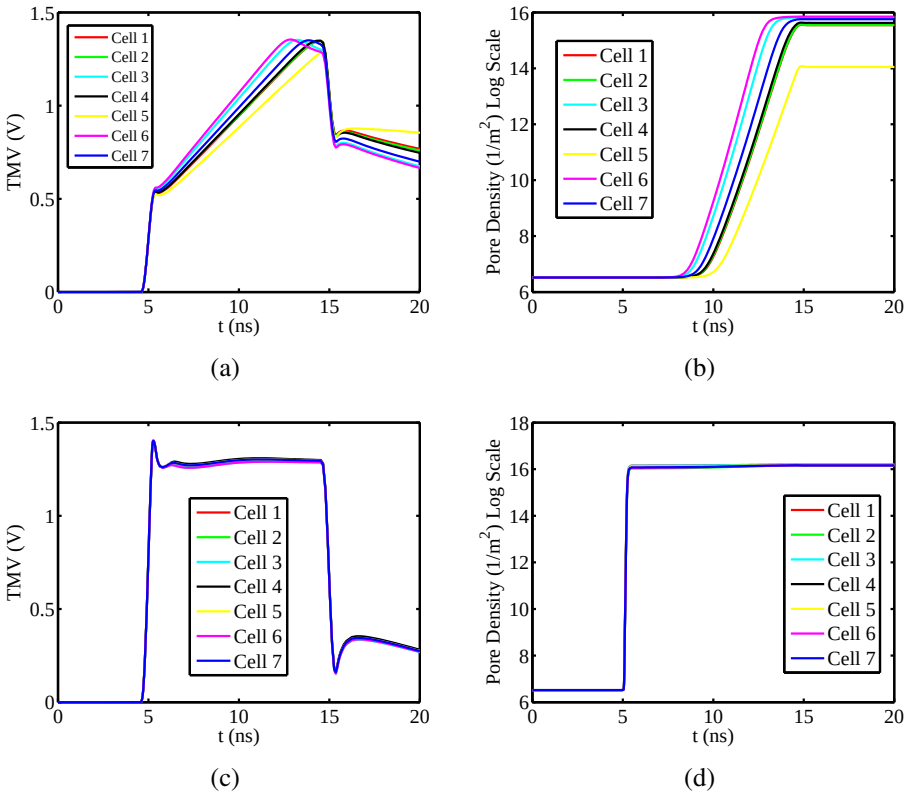

Figure 4.6: Sparse System - Temporal evolution for plasma membranes (Pm) of (a) TMV and (b) pore density for $\theta = 75°$. Temporal evolution for nuclear membranes (Nm) of (c) TMV and (d) pore density for $\theta = 75°$. Pulse amplitude and duration equal to 100 kV/cm and 10 ns.

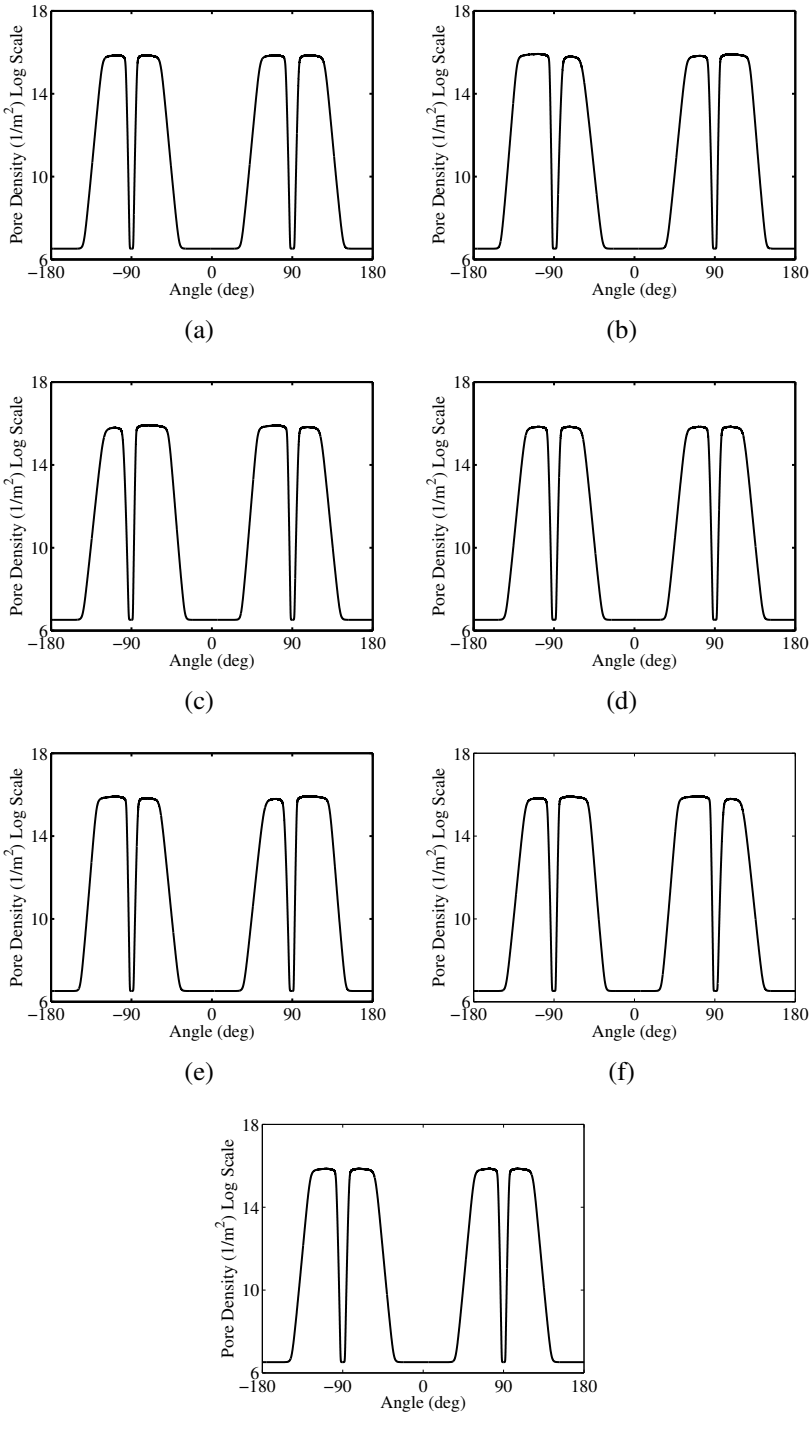

Figure 4.7: Sparse System - Plasma membranes (Pm) pore density versus the polar angle at time instant $t = 20$ ns for cell 1 (a), cell 2 (b), cell 3 (c), cell 4 (d), cell 5 (e), cell 6 (f), cell 7 (g). Pulse amplitude and duration equal to 100 kV/cm and 10 ns.

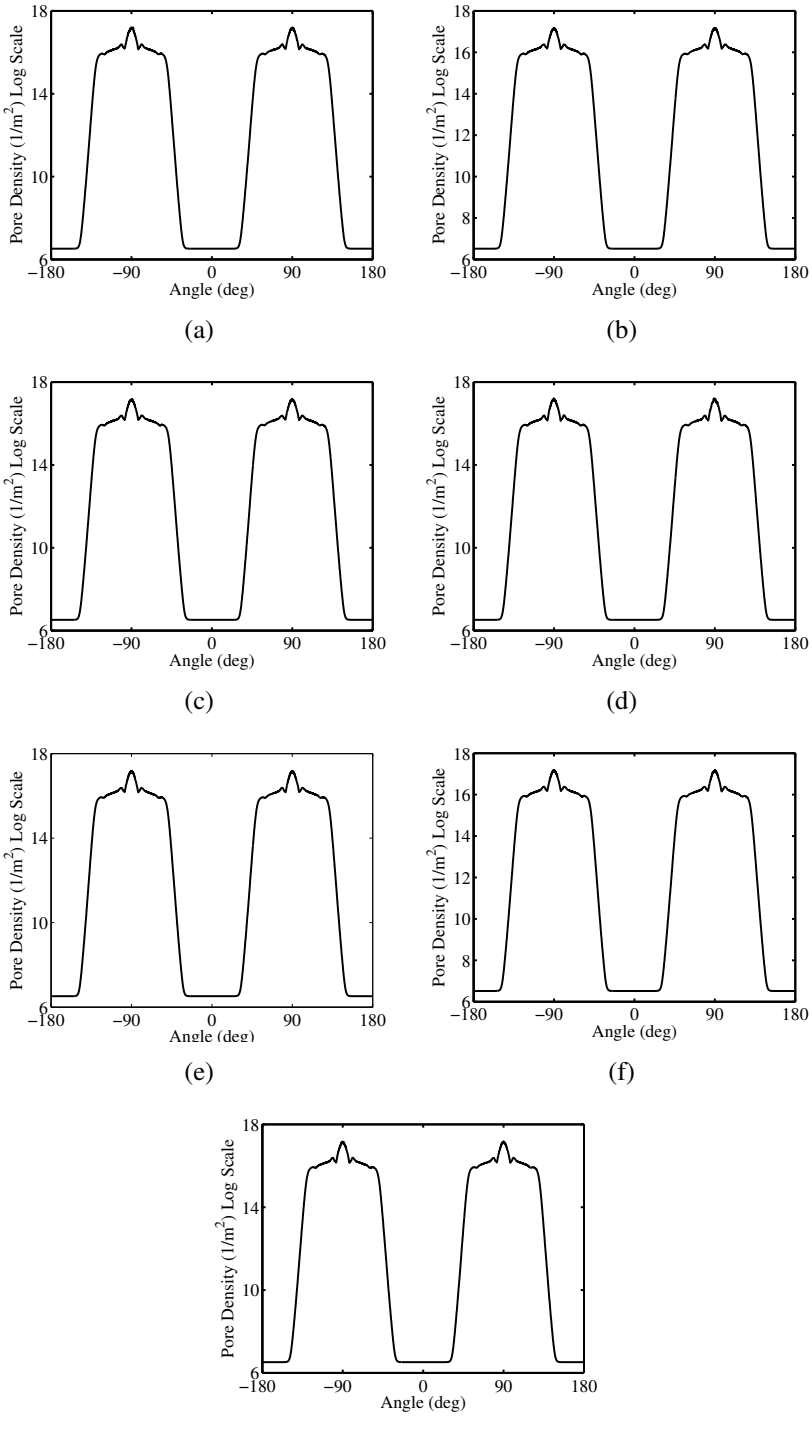

Figure 4.8: Sparse System - Nuclear membranes (Nm) pore density versus the polar angle at time instant $t = 20$ ns for cell 1 (a), cell 2 (b), cell 3 (c), cell 4 (d), cell 5 (e), cell 6 (f), cell 7 (g). Pulse amplitude and duration equal to 100 kV/cm and 10 ns.

To better analyze the shielding effect of each cell on the others the current density and the electric field at time instant $t = 10$ ns have been evaluated for the packed and the sparse system, respectively. As reported in Fig. 4.9, the current flow between the cells as the electric field interaction are more pronounced in the packed system. In particular, as shown in Fig. 4.9a-b, for the packed system an electrical interaction is evident between cells 1,2,3 and 4 as well as between cells 4,5,6 and 7. Furthermore, a good electrical mutual influence is present between the cells on the right side (cells 2 and 5) and on the left side (cells 3 and 6) of the packed system. On the contrary, as shown in Fig. 4.9c-d, the increase of the distance between the cells reduces the cells interaction on each other. Thus, in the sparse system the electrical interaction is pronounced between cells 1,2,and 3 as well as between cells 5,6 and 7.

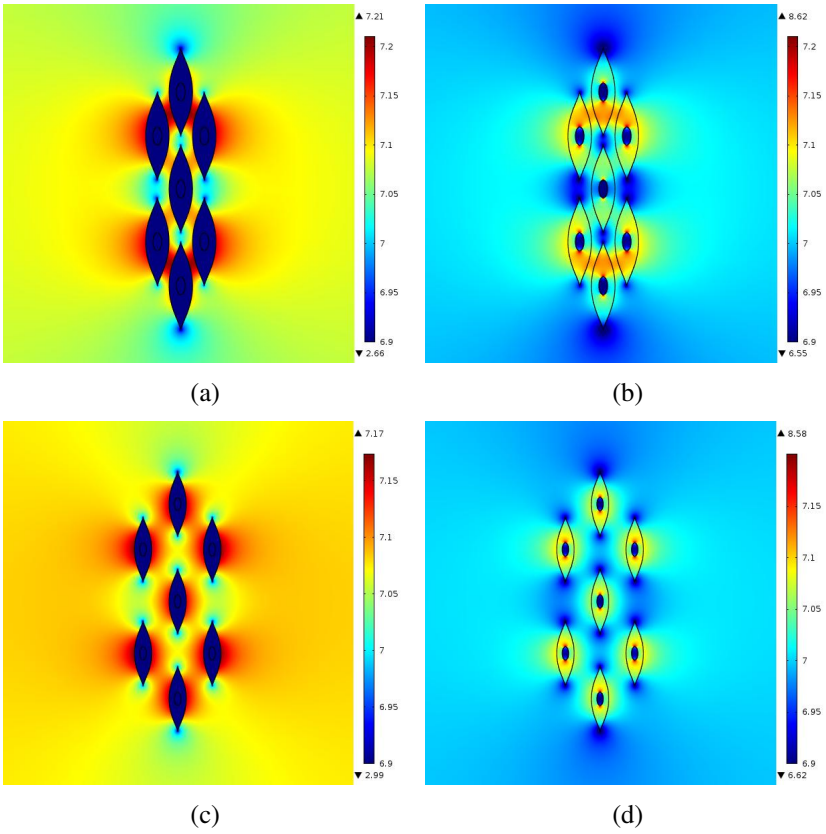

Figure 4.9: Packed System - (a) Current density log scale; (b) Electric Field log scale; Sparse System - (c) Current density log scale; (d) Electric Field log scale. Computational time instant $t = 10$ ns.

4.2 ELECTROPORATION IN 3-D IRREGULARLY SHAPED CELLS

4.2.1 ELECTRODES AND VOLTAGE DROP MEASURE

In this second part of the chapter, the research activity performed inside the laboratory of Biocybernetics of Faculty of Electrical Engineering of University of Ljubljana is described. The experimental system used for the electroporation is constituted by the signal generator BetaTech B10, the electrodes and a chamber containing the biological cells. Figure 4.10 shows the electrodes system designed to electroporate the biological cells. Three groups of 8 electrodes have been used in the experiments having a distance D between the electrodes named 1 and 5 equal to 350 μm, 250 μm and 150 μm, respectively (Fig. 4.11). The thickness of each electrode is 100 nm. Figure 4.12 shows the equivalent circuit of the system used in the experiments, where $R_m = 10\ \mathrm{k}\Omega$ is the measurement resistance, R_e the electrodes resistance and Z_c the impedance of the chamber (Fig. 4.13) filled with a sample of NaCl having a conductivity $\sigma_{NaCl} = 1.622\ \mathrm{S/m}$. A rectangular voltage pulse with amplitude of 60 V and duration of 100 μs, has been applied to channel 1, V_{CH1}, and the voltage on channel 2, V_{CH2}, has been measured (Fig. 4.14a). Using the following equation the voltage on the chamber, V_c, has been calculated (Fig. 4.14b):

$$V_c = V_{CH1} - I(R_m + R_e) \tag{4.1}$$

where I is the current that flows in the circuit, calculated as follow:

$$I = \frac{V_{CH1}}{R_m} \tag{4.2}$$

The mean value of V_c used in Comsol Multiphysics simulation has been evaluated equal to 59.9192 V. Figure 4.14c reports the comparison between the measured current and the simulated current.

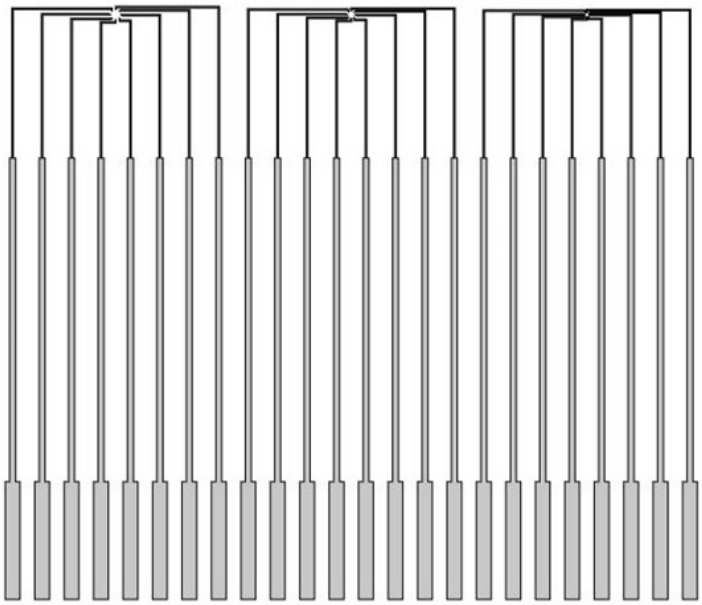

Figure 4.10: Electrodes used in the experiments.

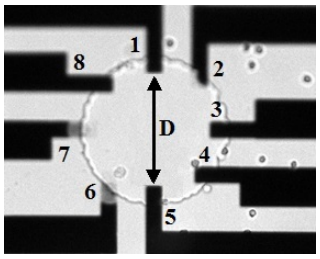

Figure 4.11: Picture enlargement of the electrodes used in the experiments in correspondence of the positioning zone of the chamber holding the biological cells. Distance D between the electrodes named 1 and 5 equal to 350 μm, 250 μm and 150 μm, respectively.

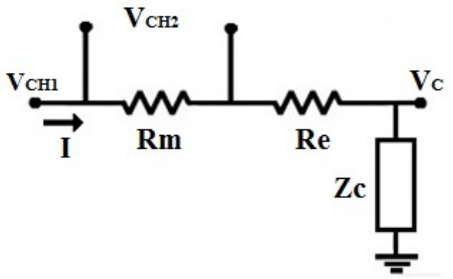

Figure 4.12: Equivalent circuit of the system used in the experiments.

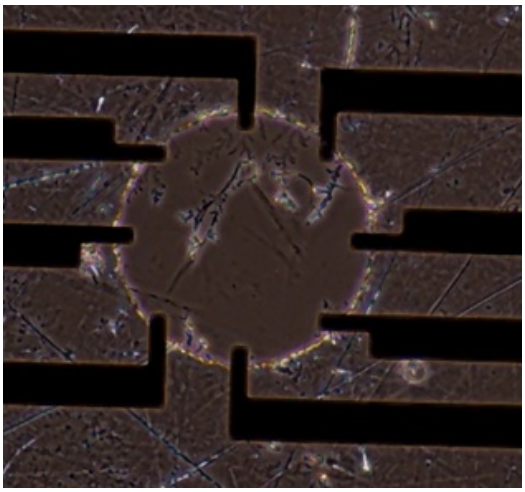

Figure 4.13: Chamber used in the experiments.

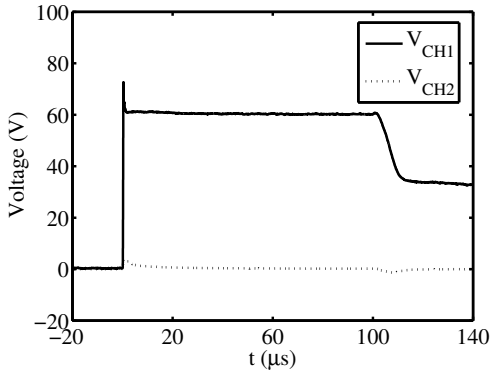

(a)

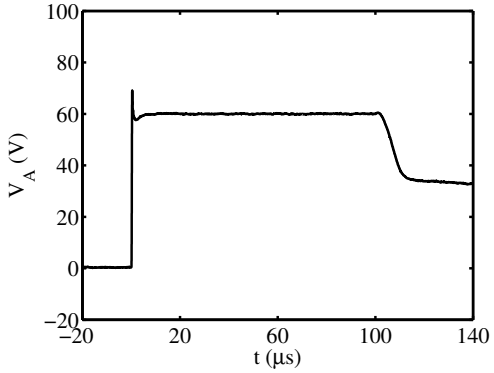

(b)

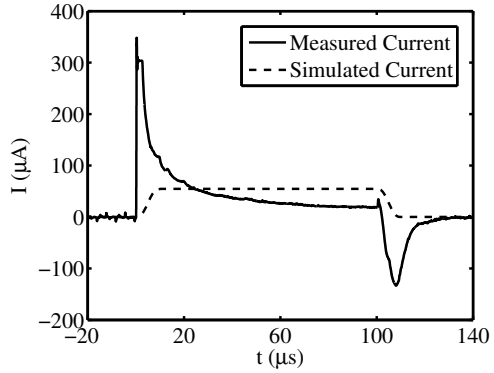

(c)

Figure 4.14: V_{CH1}, rectangular voltage pulse with amplitude of 60 V and duration of 100 µs applied to channel 1; V_{CH2}, voltage measured on channel 2.

4.2.2 3D CELLS GEOMETRY RECONSTRUCTION

Mouse melanoma cell line B16-F10 stably transfected with fluorescent protein tdTomato has been used during the experiments. The images of the real cells (Fig. 4.15) have been obtained using the confocal laser scanning microscope ZEISS LSM 800. Each cell cross-section (Fig. 4.16 and 4.17) has been acquired by shifting the focus of the microscope vertically in constant steps of 0.5 μm from the bottom to the top of the cells. The RGB images of the cells cross-section have been elaborated using an extraction algorithm based on the edge detection Sobel method. In the 3D numerical model reconstruction the cross-sections of the cells have been considered in a vertical increments of 4 μm from the bottom to the up of the cells. The extraction process generates the vector image of the contour of each cell for the different z sections (Fig. 4.18, 4.19 and 4.20). The numerical computations have been performed using MATLAB software suite. The obtained vector images for each z stack have been imported in Comsol Multiphysics and the 3D geometry of each cell have been reconstructed using the Loft operator. The generated tridimensional cell shapes have been validated comparing it with their tridimensional structure reported in ZEN software suite (Fig. 4.21, 4.22 and 4.23).

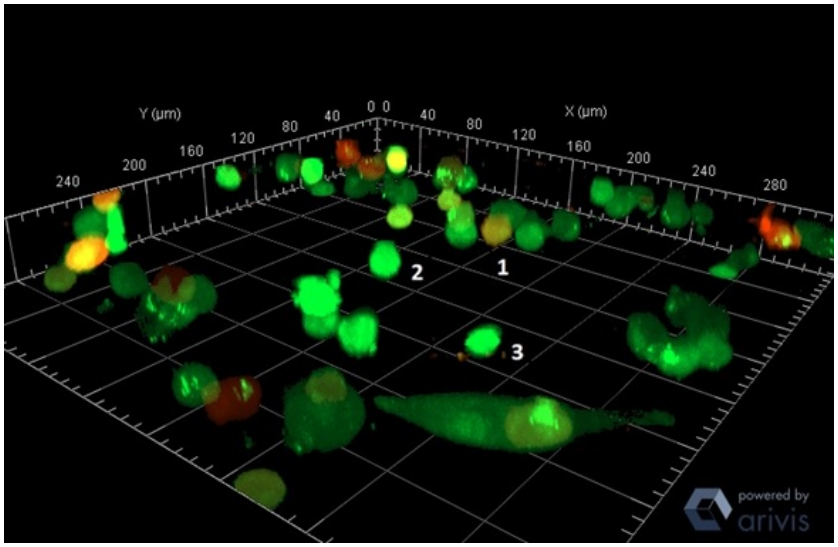

Figure 4.15: Cells 3D view obtained using ZEN software suite.

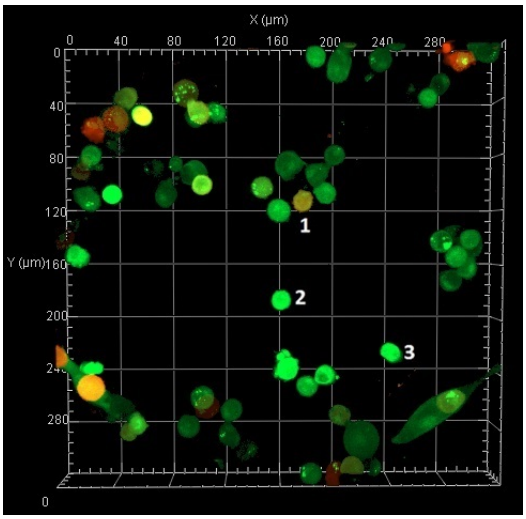

Figure 4.16: Top view of the cells using ZEN software suite.

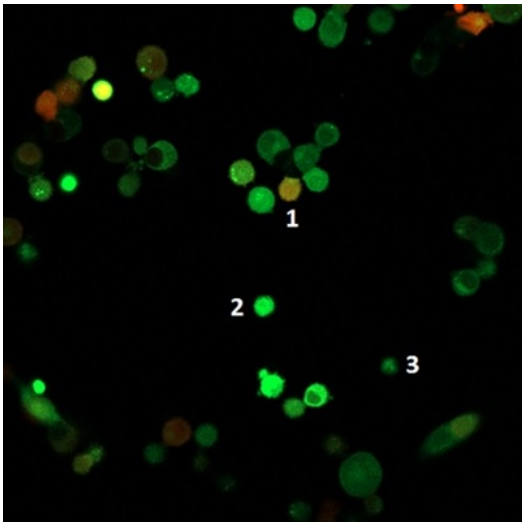

Figure 4.17: Cross-section example of the reconstructed cells.

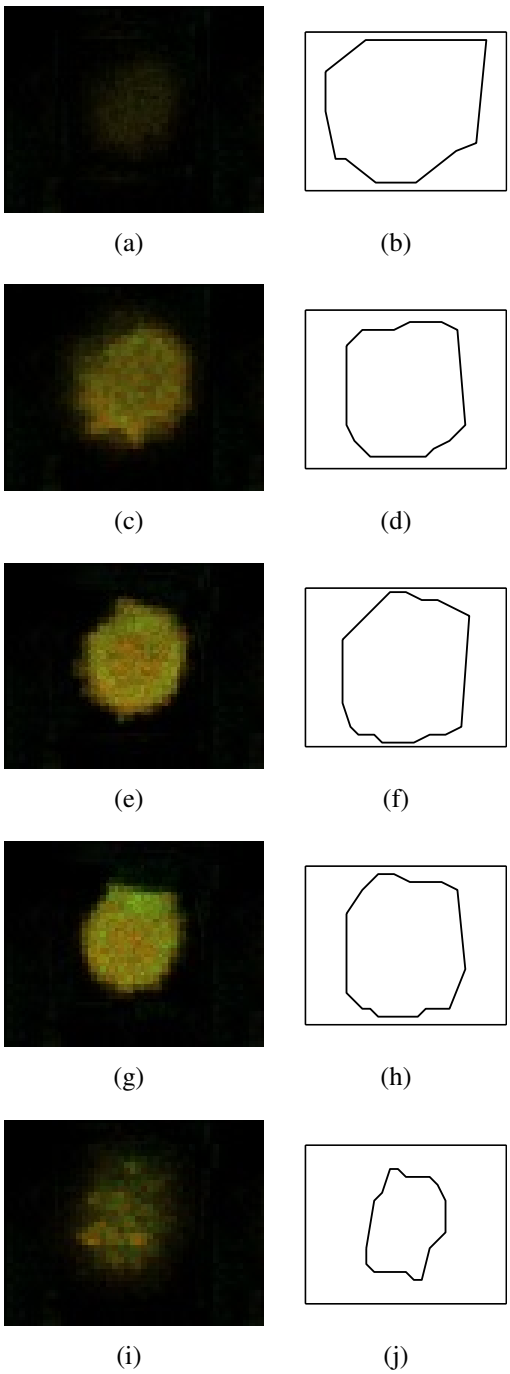

Figure 4.18: Cross-sections of cell 1 and relative contours, from the bottom to the top of the cell.

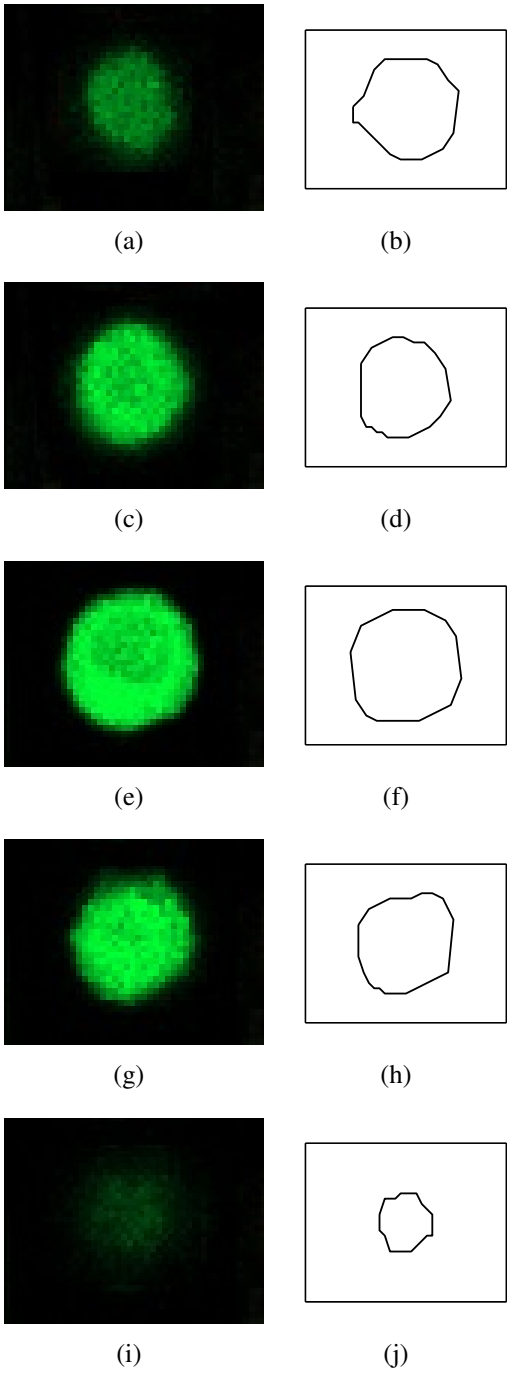

Figure 4.19: Cross-sections of cell 2 and relative contours, from the bottom to the top of the cell.

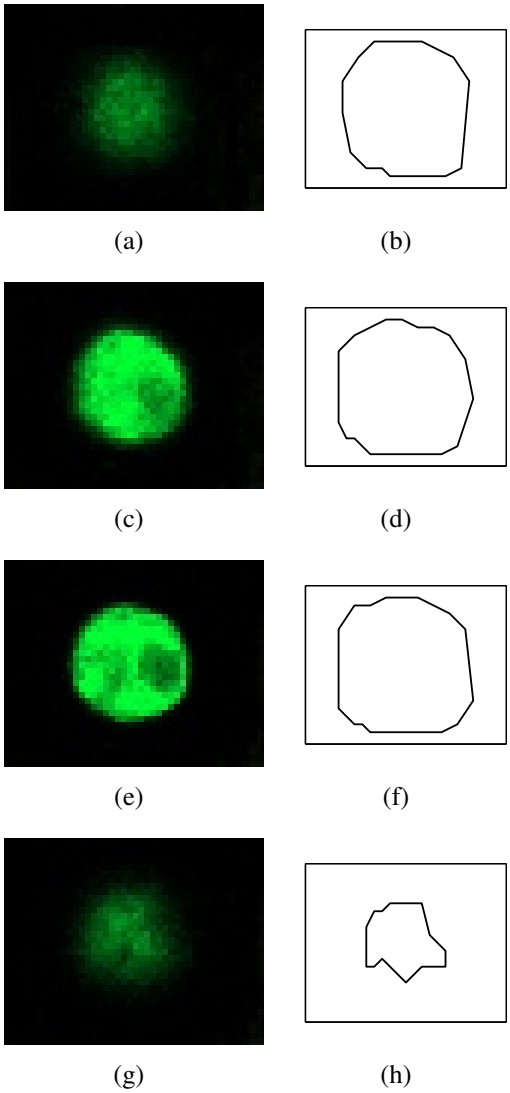

Figure 4.20: Cross-sections of cell 3 and relative contours, from the bottom to the top of the cell.

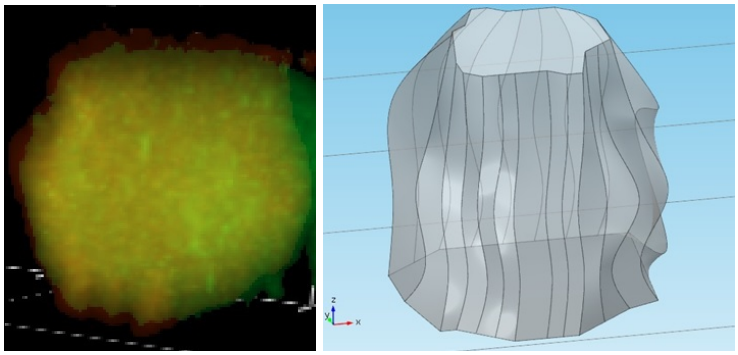

(a) (b)

Figure 4.21: (a) 3D view of cell 1 using ZEN software; (b) 3D model of cell 1.

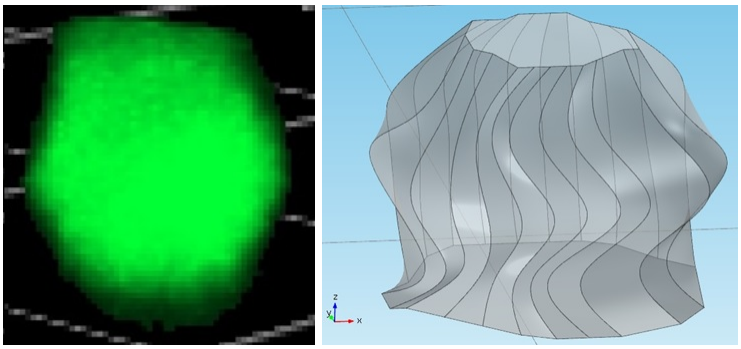

(a) (b)

Figure 4.22: (a) 3D view of cell 2 using ZEN software; (b) 3D model of cell 2.

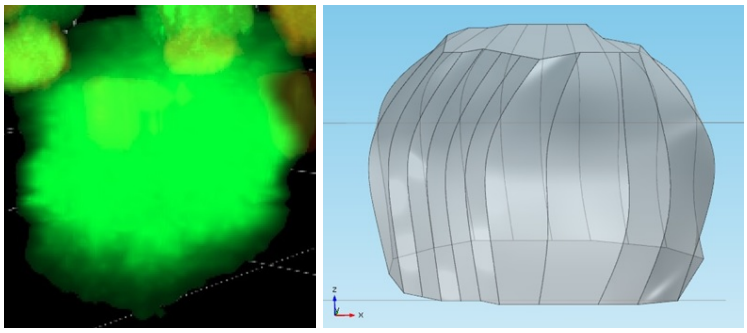

(a) (b)

Figure 4.23: (a) 3D view of cell 3 using ZEN software; (b) 3D model of cell 3.

4.3 NUMERICAL RESULTS

Figures 4.24 and 4.25 show the reconstructed 3D cells and the simulated geometry with electrodes, respectively. The group of electrodes used in the simulation and experiments has a distance between the electrodes named 1 and 5 equal to 250 μm. In the previous section the voltage drop on the electrodes has been calculated and validated. Thus to reduce the computational complexity, the model considers only the terminal parts of electrodes. In the computations, a nonlinear mathematical model of electroporation has been employed. The model solves the Maxwell's equations in conjunction with Smolouchouski partial differential equation, which describes the nonlinear pore dynamics creation. To reduce the computational complexity, each cells compartment are considered as non-dispersive media. To avoid the problems related to building the very thin cells plasma membranes, the membranes have been modeled as boundary condition [12, 92]. The geometric, electric and electroporation parameters used in the numerical procedure are summarized in table 3.2. The simulations have been performed using Comsol Multiphics. In the numerical computations and experiments the voltage signal is applied between electrodes 1 and 5. A preliminary simulation has been carried out exposing the biological cells to a rectangular voltage pulse with amplitude of 60 V, duration of 100 μs ad rise time and fall time of 40 μs. Figure 4.26 shows the obtained maximum surface pore density versus the time. In the simulation a time window of 1 s has been considered. In Fig. 4.27 and 4.28 the electric field distribution at time instant $t_0 = 100$ μs has been reported. Figure 4.29, 4.30 and 4.31 illustrate the pore density surface distribution for the three cells at time instant $t_0 = 100$ μs. In the experiments 8 pulses of 100 μs with a repetion frequency of 1 Hz have been applied to the biological system. By inspection of figure 4.26 can be inferred that the pore density reaches the equilibrium value N_0 before the starting of the next pulse. Thus the final simulation has been carried out using a single rectangular pulse. Furthermore, in the final simulation the rise time and the fall time of the rectangular voltage pulse have been reduced to 10 μs and also the voltage drop on the electrodes has been taken into account.

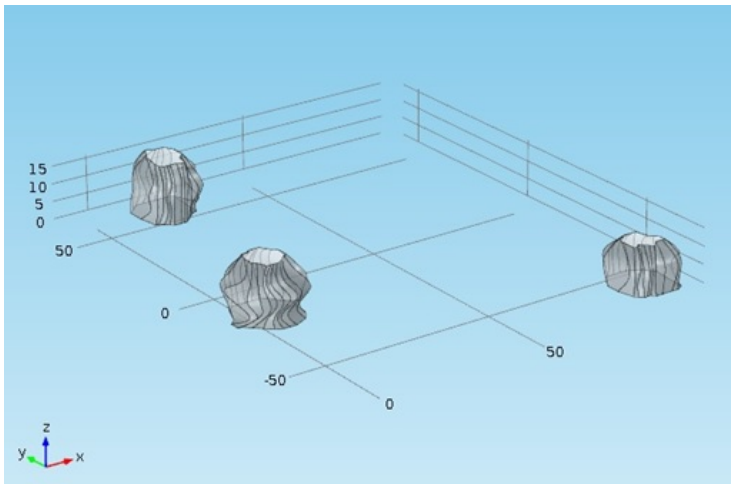

Figure 4.24: 3D cells model.

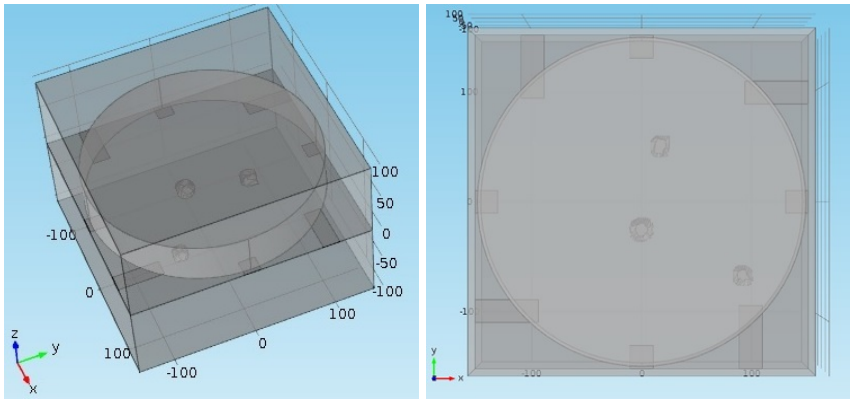

(a) (b)

Figure 4.25: (a) 3D cells model with electrodes; (b) Top view of the 3D cells model with electrodes.

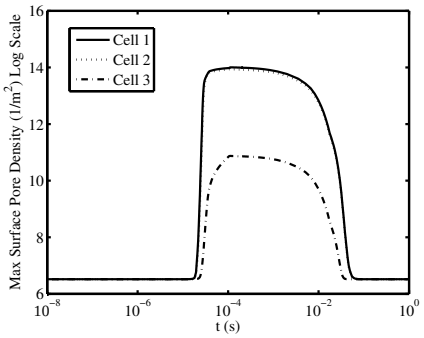

Figure 4.26: Temporal evolution of Maximum Surface Pore Density for three different cells when a time window of 1 s is considered; Rectangular unipolar pulse type, voltage amplitude 60 V, duration $T = 100$ µs, rise time $t_r = 40$ µs, fall time $t_f = 40$ µs.

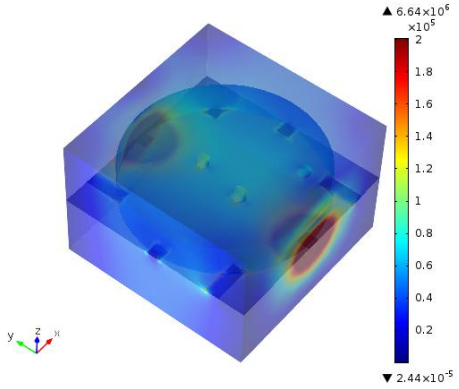

Figure 4.27: 3D view of Electric Field (V/m) distribution at time instant $t_0 =$ 100 µs.

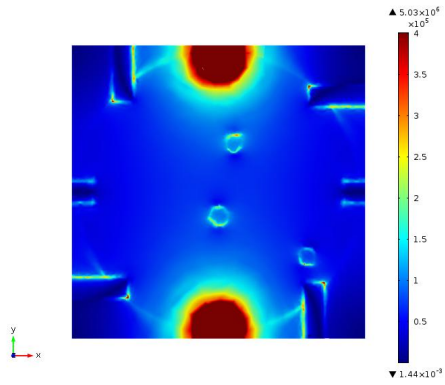

Figure 4.28: Electric Field (V/m) distribution for $z = 0$ at time instant $t_0 = 100$ µs.

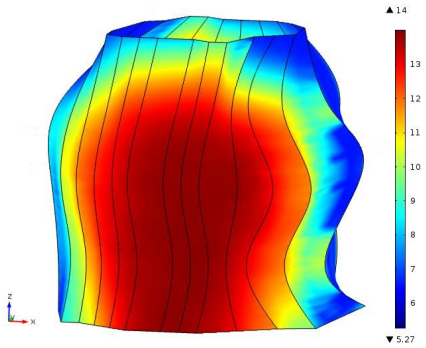

Figure 4.29: Pore Density surface distribution for cell 1 at time instant $t_0 = 100$ µs.

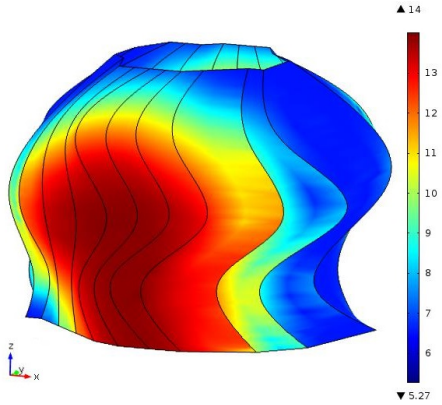

Figure 4.30: Pore Density surface distribution for cell 2 at time instant $t_0 = 100$ µs.

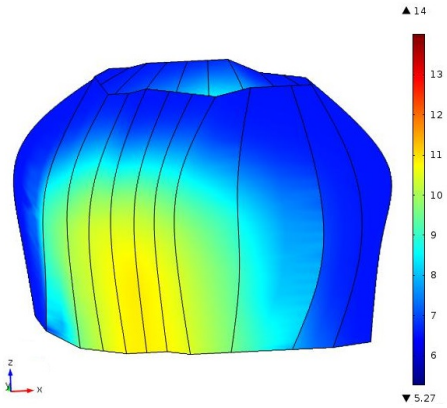

Figure 4.31: Pore Density surface distribution for cell 3 at time instant $t_0 = 100$ µs.

Fig. 4.32a and 4.32b show the temporal evolution of maximum surface TMV and pore density when the biological cells are exposed to a rectangular unipolar pulse type having voltage amplitude 60 V (voltage used in the simulation 59.9192 V), duration of 100 µs, rise time and fall time of 10 µs. The obtained numerical results have been compared with experimental ones reported in Fig. 4.32c. Electroporation was detected using the calcium sensitive dye Fluo-4 AM (ThermoFischer Scientific, USA). Stably transfected cells with fluorescent protein tdTomato emitted fluorescence in red range and in green range from Fluo-4 AM when the intracellular calcium concentration increased due to electroporation. By inspection of Fig. 4.32b and 4.32c, it is inferred that cell 1 and cell 2 are both electroporated and cell 3 is not electroporated. As result a good agreement between the numerical and experimental results has been obtained.

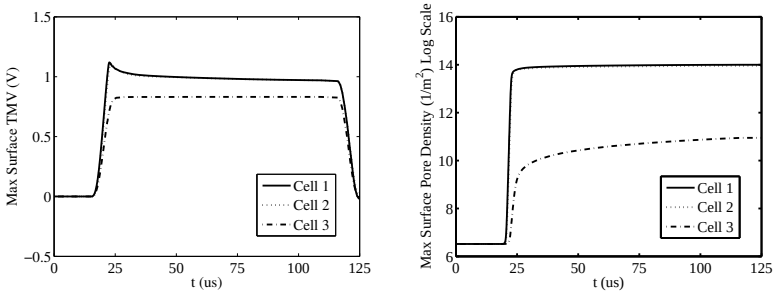

(a) (b)

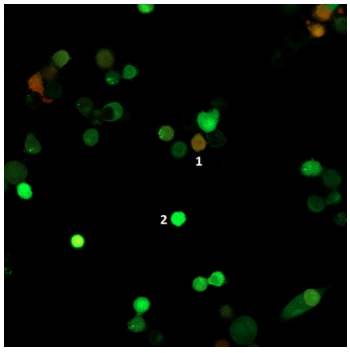

(c)

Figure 4.32: (a) Temporal evolution of Maximum Surface TMV for three different cells; (b) Temporal evolution of Maximum Surface Pore Density for three different cells. (c) Experimental results. Rectangular unipolar pulse type, voltage amplitude 60 V (voltage used in the simulation 59.9192 V), duration $T = 100$ µs, rise time $t_r = 10$ µs, fall time $t_f = 10$ µs.

CONCLUSIONS

In this PhD dissertation, the electroporation process induced by pulsed electric field on different biological cells and on multiple irregular cells systems has been analyzed. A non-local and space-time numerical model based on the asymptotic Smoluchowskis equation and the Maxwells equations has been developed to study the EP process induced by PEFs in irregularly shaped cells. The shape of the general cell has been modeled by using a unified geometrical approach based on Gielis superformula. Furthermore, in order to enable an accurate prediction of both the spatial distribution and the time response of TMV and pore density under nanosecond pulsed regime, the dielectric relaxation of the extracellular, plasma membrane, cytoplasm and nuclear media have been modeled using a general multi-relaxation Debye based formulation. In the first part of third chapter the EP induced by PEF has been studied for different types of non-nucleated cells. An unconventional behavior has been observed in the considered class of irregularly shaped cells, contrary to canonical spherical cell based models. In particular, the typical cosine law of TMV is lost, while inhomogeneous EP phenomena occur. The muscular-like cell exhibits a negligible pore density within the sharp region facing the PEF electrodes. The cell in mitosis phase, on the contrary, shows a very high pore density within the same membrane sector. For the cell in mitosis phase the EP does not occur in the very limited areas around the angles $\theta = 0^\circ$ and $\theta = \pm 45^\circ$. In contrast, the muscular-like cell has a negligible pore density within the wide membrane area ranging from $\theta = -45^\circ$ to $\theta = 45^\circ$. In the second part of the third chapter, considering the nucleated prolate spheroidal cell and the smooth muscular cell with decentralized nucleus, various simulations have been done to investigate the differences between the nonlinear dispersive model and the nonlinear nondispersive model.

Starting from the prolate spheroidal cell, an absolute difference between the dispersive and non-dispersive EPRL of 2.5 % for the plasma membrane and 7.3 % for the nuclear membrane are obtained. This difference increases with the irregular geometrical shape of the plasma membrane. In particular, for the muscular-like cell with the nucleus decentralized along the Y axes of $s = 1$ μm, EPRL is, respectively, 26.7 % for the plasma membrane and 7.1 % for the nuclear membrane. Finally, a parametric analysis has been conducted, to evaluate the absolute difference between the dispersive and non-dispersive EP opening angles as functions of the nucleus decentralization parameter s. A $\Delta EPRL$ ranging, respectively, between 17.2 % and 27.2 % for the plasma membrane and between 7 % and 7.3 % for the nuclear membrane is obtained. From the results analyzed it is possible to conclude that for real like cells a relevant difference is evaluated between the nonlinear dispersive model and the nonlinear nondispersive model. In the first part of the last chapter, the EP process induced by PEFs in 2-D multiple irregularly shaped cells systems has been analyzed. Using the numerical model described in Chapter 2, the electroporation process has been studied for two types of multiple irregularly shaped cells systems: packed system and sparse system. For each multiple irregularly shaped cells system 7 nucleated muscular-like cells have been considered. By the computational analysis it is concluded that the electroporation process is more evident in the sparse system than in the packed system. This result is essentially due to the shielding effect of each cell on the others. In the last part of the PhD thesis the research activity performed inside the laboratory of Biocybernetics of Faculty of Electrical Engineering of University of Ljubljana has been described. The cells cross-section RGB images have been elaborated using an extraction algorithm based on the edge detection Sobel method and the 3D geometry of each cell have been reconstructed in Comsol Multiphysics. The biological cells have been exposed to a rectangular unipolar pulse type having voltage amplitude 60 V, duration of 100 μs, rise time and fall time of 10 μs. As result a good agreement between the numerical and experimental results has been obtained.

FUTURE WORK

As previosly highlighted in the present work, the mathematical model developed for the study of the electroporation process calculates the temporal evolution of pore creation and resealing using the Smoluchowskis equation. Such equation involves several parameters and cannot be solved analytically. To overcome this drawback, it has been assumed that pores have a constant radius of 0.8 nm and thus the asymptotic Smoluchowskis equation has been employed. However, in the literature there are models of the phenomenon of electroporation, which include in the numerical analysis the temporal variation of the pores size [76, 93]. These models calculate transmembrane potential, number of pores, and distribution of pore radii as functions of time and position on the cell surface. Both the models presented in [76] and [93] evaluate the pores size spatial and time evolution by using a set of differential equations. Therefore, in order to improve the numerical analysis of the electroporation process presented in this thesis dissertation, it is proposed in a future work the insertion in the mathematical model of the differential equations that describe the dynamics of the pore radii. Furthermore the developed computational model has introduced the polarization vector in the electroquasistatic equation, describing the dispersive properties of cell's media. In particular, a first-order Debye equation has been used to model the cytoplasm and external media and a second-order Debye equation to describe the cell's membrane dispersion. A further improvement of the model can be obtained by describing the dispersive properties of the materials in a more specific way. For this purpose, in a future work in the model the dispersive properties of the materials will be described by using multi-relaxation Debye equations higher than the second order.

Bibliography

[1] T. S. Santra, C. W. Lee, S. Kar, J. Borana, P. C. Wang, and F. G. Tseng, "Nanolocalized single cell membrane nanoelectroporation." *Proceedings of the 9th IEEE International Conference on Nano/Micro Engineered and Molecular Systems*, pp. 285–288, 2014.

[2] P. Deng, H. Mei, and Y. K. Lee, "A nonlinear cell electroporation model and its verification using micro electroporation chips." *Proceedings of the 9th IEEE International Conference on Nano/Micro Engineered and Molecular Systems*, pp. 311–314, 2014.

[3] K. C. Smith and J. C. Weaver, "Active mechanisms are needed to describe cell responses to submicrosecond, megavolt-per-meter pulses: Cell models for ultrashort pulses." *Biophysical Journal*, vol. 95, pp. 1547–1563, 2008.

[4] E. Salimi, D. J. Thomson, and G. E. Bridges, "Membrane dielectric dispersion in nanosecond pulsed electroporation of biological cells," *IEEE Trans. Dielectr. Electr. Insul.*, vol. 20, no. 4, pp. 1256–1265, 2013.

[5] A. Denzi, C. Merla, P. Camilleri, A. Paffi, G. dInzeo, F. Apollonio, and M. Liberti, "Microdosimetric study for nanosecond pulsed electric fields on a cell circuit model with nucleus." *J Membrane Biol.*, pp. 351–354, 2013.

[6] S. R. Bolsover, J. S. Hyams, E. A. Shephard, H. A. White, and C. G. Wiedemann, "Cell biology a short course, second edition," *John Wiley and Sons*, pp. 1–16, 2004.

[7] L. A. MacQueen, M. Thibault, M. D. Buschmann, and M. R. Wertheimer, "Electro–manipulation of biological cells in microdevices," *IEEE Trans. Dielectr. Electr. Insul.*, vol. 19, pp. 1261–1268, 2012.

[8] Y. T. Chow, S. Chen, R. Wang, C. Liu, C. Kong, R. A. Li, S. H. Cheng, and D. Sun, "Single cell transfection through precise microinjection with quantitatively controlled injection volumes," *Scientific Reports*, vol. 6, pp. 1–9, 2016.

[9] M. L. Yarmush, A. Golberg, G. Sersa, T. Kotnik, and D. Miklavcic, "Electroporation-based technologies for medicine: Principles, applications and challenges," *Annual Review of Biomedical Engineering*, vol. 16, pp. 295–320, 2014.

[10] A. G. Pakhomov, D. Miklavcic, and M. S. Markov, "Advanced electroporation techniques in biology and medicine," *CRC Press*, 2010.

[11] A. Denzi, F. Camera, C. Merla, B. Benassi, C. Consales, A. Paffi, F. Apollonio, and M. Liberti, "A microdosimetric study of electropulsation on multiple realistically shaped cells: Effect of neighbours." *J Membrane Biol*, pp. 691–701, 2016.

[12] L. Towhidi, T. Kotnik, G. Pucihar, S. M. P. Firoozabadi, H. Mozdaran, and D. Miklavcic., "Variability of the minimal transmembrane voltage resulting in detectable membrane electroporation." *Electromagnetic Biology and Medicine*, vol. 27, p. 372385, 2008.

[13] H. Qiu, S. Xiao, and R. P. Joshi, "Simulations of voltage transients across intacellular mitochondrial membranes due to nanosecond electrical pulses," *IEEE Trans. Plasma Sci.*, vol. 42, no. 10, pp. 3113–3120, 2014.

[14] G. Pucihar, J. Krmelj, M. Rebersek, T. B. Napotnik, and D. Miklavicic, "Equivalent pulse parameters for electroporation," *IEEE Transactions on Biomedical Engineering*, vol. 58, p. 3279 3288, 2011.

[15] K. C. Melikov, V. A. Frolov, A. Shcherbakov, A. V. Samsonov, Y. A. Chizmadzhev, and L. V. Chernomordik, "Voltage-induced nonconductive pre-

pores and metastable single pores in unmodified planar lipid bilayer," *Biophysical Journal*, vol. 80, p. 1829 1836, 2001.

[16] R. E. Neal, P. A. Garcia, J. L. Robertson, and R. V. Davalos, "Experimental characterization and numerical modeling of tissue electrical conductivity during pulsed electric fields for irreversible electroporation treatment planning," *IEEE Transactions on Biomedical Engineering*, vol. 59, pp. 1076–1085, 2012.

[17] J. Gehl, "Electroporation: theory and methods, perspectives for drug delivery, gene therapy and research," *Acta Physiologica Scandinavica*, vol. 177, pp. 437–447, 2003.

[18] M. Rao, J. Baraban, F. Rajaii, and S. Sockanathan, "In vivo comparative study of rnai methodologies by in ovo electroporation in the chick embryo," *Developmental Dynamics*, vol. 231, p. 592 600, 2004.

[19] M. Sustarsic, A. Plochowietz, L. Aigrain, Y. Yuzenkova, N. Zenkin, and A. Kapanidis, "Optimized delivery of fluorescently labeled proteins in live bacteria using electroporation," 2014.

[20] K. Yan, H. Todo, and K. Sugibayashi, "Transdermal drug delivery by in-skin electroporation using a microneedle array," *International Journal of Pharmaceutics*, vol. 397, p. 7783, 2010.

[21] S. Baron, J. Poast, D. Rizzo, E. McFarland, and E. Kieff, "Electroporation of antibodies, dna, and other macromolecules into cells: a highly efficient method," *Journal of Immunological Methods*, vol. 242, pp. 115–126, 2000.

[22] S. Yumura, "Rapid redistribution of myosin ii in living dictyostelium amoebae, as revealed by fluorescent probes introduced by electroporation," *Protoplasma*, vol. 192, pp. 217–227, 1996.

[23] C. Liu, X. Xie, W. Zhao, N. Liu, P. A. Maraccini, L. M. Sassoubre, A. B. Boehm, and Y. Cui, "Conducting nanosponge electroporation for affordable and highefficiency disinfection of bacteria and viruses in water," *American Chemical Society Nano Letters*, pp. A–F, 2013.

[24] H. Y. Lin, S. E. Lin, S. F. Chien, and M. K. Chern, "Electroporation for three commonly used yeast strains for two-hybrid screening experiments," *Analytical Biochemistry*, vol. 416, pp. 117–119, 2011.

[25] G. W. Bates, "Genetic transformation of plants by protoplast electroporation," *Molecular Biotechnology*, vol. 2, pp. 135–145, 1994.

[26] H. Fujimoto, K. Kato, and H. Iwata, "Electroporation microarray for parallel transfer of small interfering rna into mammalian cells," *Analytical and Bioanalytical Chemistry*, vol. 392, pp. 1309–1316, 2008.

[27] F. Guo, C. Yao, C. Li, Y. Mi, Y. Wen, and J. Tang, "Dependence on pulse duration and number of tumor cell apoptosis by nanosecond pulsed electric fields," *IEEE Trans. Dielectr. Electr. Insul.*, vol. 20, pp. 1195–1200, 2013.

[28] P. Lamberti, V. Tucci, S. Romeo, A. Sannino, M. R. Scarfi, and O. Zeni, "nspef-induced effects on cell membranes: Use of electrophysical model to optimize experimental design." *IEEE Transactions on Dielectrics and Electrical Insulation*, vol. 20, pp. 1231–1238, 2013.

[29] S. J. Beebe, "Bioelectrics in basic science and medicine: Impact of electric fields on cellular structures and functions," *J. Nanomed. Nanotechol.*, vol. 4, no. 2, pp. 1–8, 2013.

[30] H. P. Schwan, "Electrical properties of tissue and cell suspensions," *Advances in Biological and Medical Physics*, vol. 5, pp. 147–209, 1957.

[31] T. Kotnik and D. Miklavcic, "Theoretical evaluation of the distributed power dissipation in biological cells exposed to electric fields," *Bioelectromagnetics*, vol. 21, pp. 385–394, 2000.

[32] A. J. H. Sale and W. A. Hamilton, "Effects of high electric fields on microorganism iii. lysis of erythrocytes and protoplasts," *Biochimica et Biophysica Acta*, pp. 37–43, 1968.

[33] C. Yao, Y. Mi, C. Li, X. Hu, X. Chen, and C. Sun, "Study of transmembrane potentials on cellular inner and outer membranefrequency response model

and its filter characteristic simulation," *IEEE Transactions on Biomedical Engineering*, vol. 55, pp. 1792–1799, 2008.

[34] M. Pavlin, T. Kotnik, D. Miklavcic, P. Kramar, and A. M. Lebar, "Advances in planar lipid bilayers and liposomes," *Elsevier*, vol. 6, 2008.

[35] T. Kotnik, P. Kramar, G. Pucihar, and D. Miklavcic, "Cell membrane electroporation - part 1: The phenomenon," *IEEE Electrical Insulation Magazine*, vol. 28, pp. 14–23, 2012.

[36] G. Pucihar, D. Miklavcic, and T. Kotnik, "A time–dependent numerical model of transmembrane voltage inducement and electroporation of irregularly shaped cells," *IEEE Trans. Biomed. Eng.*, vol. 56, no. 5, pp. 1491–1501, 2009.

[37] K. C. Smith, T. R. Gowrishankar, A. T. Esser, D. A. Stewart, and J. C. Weaver, "The spatially distributed dynamic transmembrane voltage of cells and organelles due to 10-ns pulses: Meshed transport networks." *IEEE Transactions on Plasma Science*, vol. 34, pp. 1394–1404, 2006.

[38] L. D. S. Pereira and D. O. H. Suzuki, "Effects of nanoelectroporation on plasma and nuclear membranes." *VII Latin American Symposium on Circuits and Systems (LASCAS)*, pp. 351–354, 2016.

[39] L. Retelj, G. Pucihar, and D. Miklavcic, "Electroporation of intracellular liposomes using nanosecond electric pulses–a theoretical study," *IEEE Trans. Biomed. Eng.*, vol. 60, pp. 2624–2635, 2013.

[40] C. Yao, H. Liu, Y. Zhao, Y. Mi, S. Dong, and Y. Lv, "Analysis of dynamic processes in single-cell electroporation and their effects on parameter selection based on the finite-element model," *IEEE Trans. Plasma Sci.*, vol. 45, pp. 889–900, 2017.

[41] L. Rems, M. Uaj, M. Kanduer, M. Reberek, D. Miklavcic, and G. Pucihar, "Cell electrofusion using nanosecond electric pulses." *Scientific Reports*, pp. 1–10, 2013.

[42] A. Denzi, A. A. Escobar, C. Nasta, C. Merla, B. Benassi, C. Consales, F. Apollonio, and M. Liberti, "A microdosimetry study for a realistic shaped nucleus." *IEEE*, pp. 4189–4192, 2016.

[43] T. B. Napotnik, M. Reberek, P. T. Vernier, B. Mali, and D. Miklavcic, "Effects of high voltage nanosecond electric pulses on eukaryotic cells (in vitro): A systematic review." *Bioelectrochemistry*, pp. 1–12, 2016.

[44] R. P. Joshi and Q. Hu, "Case for applying subnanosecond high-intensity, electrical pulses to biological cells." *IEEE Transactions on Biomedical Engineering*, vol. 58, pp. 2860–2866, 2011.

[45] D. Miklavcic and L. Towhidi, "Numerical study of the electroporation pulse shape effect on molecular uptake of biological cells," *Radiology and Oncology*, vol. 44, pp. 34–41, 2009.

[46] D. A. Stewart, T. R. Gowrishankar, and J. C. Weaver, "Transport lattice approach to describing cell electroporation: use of a local asymptotic model." *IEEE Transactions on Plasma Science*, vol. 32, p. 16961708, 2004.

[47] J. C. Neu and W. Krassowska, "Asymptotic model of electroporation." *Physical Review E*, vol. 59, p. 34713482, 1999.

[48] J. Gielis, "A generic geometric transformation that unifies a wide range of natural and abstract shapes," *American Journal of Botany*, vol. 90, pp. 333–338, 2003.

[49] P. Bia, D. Caratelli, L. Mescia, and J. Gielis, "Analysis and synthesis of supershaped dielectric lens antennas," *IET Microwaves, Antennas & Propagation*, vol. 9, pp. 1497–1504, 2015.

[50] L. Mescia, P. Bia, D. Caratelli, M. A. Chiapperino, O. Stukach, and J. Gielis, "Electromagnetic mathematical modeling of 3d supershaped dielectric lens antennas," *Mathematical Problems in Engineering*, vol. 2016, p. Article ID 8130160, 2016.

[51] A. G. Pakhomov, I. Semenov, S. Xiao, O. N. Pakhomova, B. Gregory, K. H. Schoenbach, J. C. Ullery, H. T. Beier, S. R. Rajulapati, and B. L. Ibey, "Cancellation of cellular responses to nanoelectroporation by reversing the stimulus polarity." *Cellular and Molecular Life Sciences.*, 2014.

[52] T. R. Gowrishankar, A. T. Esser, Z. Vasilkoski, K. C. Smith, and J. C. Weaver, "Microdosimetry for conventional and supra-electroporation in cells with organelles," *Biochemical and Biophysical Research Communications*, pp. 1266–1276, 2006.

[53] D. Xiao, C. Yao, H. Liu, C. Li, J. Cheng, F. Guo, and L. Tang, "Irreversible electroporation and apoptosis in human liver cancer cells induced by nanosecond electric pulses." *Bioelectromagnetics*, pp. 512–520, 2013.

[54] O. N. Pakhomova, B. Gregory, I. Semenov, and A. G. Pakhomov, "Calcium-mediated pore expansion and cell death following nanoelectroporation." *Biochimica et Biophysica Acta*, pp. 2547–2554, 2014.

[55] M. Gundersen, P. T. Vernier, L. Marcua, A. Lib, X. Zhub, A. Z. Gallam, T. Katsouleas, C. Young, and M. B. C. M. Craftb, "Ultrashort pulse electroporation: Applications of high pulsed electric fields to induced caspase activation of human lymphocytes." *IEEE*, pp. 667–670, 2002.

[56] P. T. Vernier, M. J. Ziegler, Y. Sun, W. V. Chang, M. A. Gundersen, and D. P. Tieleman, "Nanopore formation and phosphatidylserine externalization in a phospholipid bilayer at high transmembrane potential." *American Chemical Society*, vol. 128, pp. 6288–6289, 2006.

[57] P. T. Vernier, Y. Sun, L. Marcu, S. Salemi, C. M. Craf, and M. A. Gundersena, "Calcium bursts induced by nanosecond electric pulses." *Biochemical and Biophysical Research Communications*, pp. 286–295, 2003.

[58] T. B. Napotnik, T. H. Wu, M. A. Gundersen, D. Miklavcic, and P. T. Vernier, "Nanosecond electric pulses cause mitochondrial membrane permeabilizationin jurkat cells." *Bioelectromagnetics*, pp. 257–264, 2012.

[59] S. J. Beebe, J. White, P. F. Blackmore, Y. Deng, K. Somers, and K. H. Schoenbach, "Diverse effects of nanosecond pulsed electric fields on cells and tissues." *DNA and Cell Biology*, vol. 22, p. 785796, 2003.

[60] C. Domenge, B. Luboinski, T. D. Baere, G. Schwaab, J. Belehradek, and L. M. Mir, "Antitumor electrochernotherapy new advances in the clinical protocol," *American Cancer Society*, vol. 77, pp. 956–963, 1996.

[61] L. M. Mir, S. Orlowski, J. B. Jr, J. Teissi, M. Rols, G. Sersa, D. Miklavicic, R. Gilbert, and R. Heller, "Biomedical applications of electric pulses with special emphasis on antitumor electrochemotherapy," *Bioelectrochemistry and Bioenergetics*, vol. 38, pp. 203–207, 1995.

[62] M. Rebersek, S. Corovic, G. Sersa, and D. Miklavcic, "Electrode commutation sequence for honeycomb arrangement of electrodes in electrochemotherapy and corresponding electric field distribution." *Bioelectrochemistry*, vol. 74, pp. 26–31, 2008.

[63] A. Zupanic, S. Corovic, and D. Miklavcic, "Optimization of electrode position and electric pulse amplitude in electrochemotherapy," *Radiology and Oncology*, vol. 42, pp. 93–101, 2008.

[64] G. Pucihar, L. M. Mir, and D. Miklavcic, "The effect of pulse repetition frequency on the uptake into electropermeabilized cells in vitro with possible applications in electrochemotherapy," *Bioelectrochemistry*, vol. 57, pp. 167–172, 2002.

[65] G. Sersa, "The state-of-the-art of electrochemotherapy before the esope study; advantages and clinical uses," *EJC Supplements*, vol. 4, pp. 52–59, 2006.

[66] L. G. Campana, A. Testori, N. Mozzillo, and C. R. Rossi, "Treatment of metastatic melanoma with electrochemotherapy," *Journal of Surgical Oncology*, vol. 109, pp. 301–307, 2014.

[67] E. M. Grischke, C. Rohm, E. Staub, F. A. Taran, S. Y. Brucker, and D. Wallwiener, "Electrochemotherapy supplementary treatment for loco-regional

metastasized breast carcinoma administered to concomitant systemic therapy," *Radiology and Oncology*, vol. 51, pp. 317–323, 2017.

[68] A. Groselj, M. Bosnjak, P. Strojan, M. Krzan, M. Cemazar, and G. Sersa, "Efficiency of electrochemotherapy with reduced bleomycin dose in the treatment of nonmelanoma head and neck skin cancer: Preliminary results," *Head & Neck*, pp. 1–6, 2017.

[69] G. F. Macri, A. Greco, A. Gallo, M. Fusconi, C. Marinelli, and M. de Vincentiis, "Use of electrochemotherapy in a case of neck skin metastasis of oral squamous cell carcinoma: Case report and considerations," *Head & Neck*, pp. 86–90, 2014.

[70] S. P. Salwa, M. G. Bourke, P. Forde, M. OShaughnessy, S. T. OSullivan, E. J. Kelly, D. M. Soden, and A. J. P. Clover, "Electrochemotherapy for the treatment of ocular basal cell carcinoma; a novel adjunct in the disease management," *Journal of Plastic, Reconstructive & Aesthetic Surgery*, vol. 67, pp. 403–406, 2014.

[71] R. V. Davalos, L. M. Mir, and B. Rubinsky, "Tissue ablation with irreversible electroporation," *Annals of Biomedical Engineering*, vol. 33, pp. 223–231, 2005.

[72] J. J. Wendler, M. Pech, S. Blaschke, M. Porsch, A. Janitzky, M. Ulrich, O. Dudeck, J. Ricke, and U. B. Liehr, "Angiography in the isolated perfused kidney: Radiological evaluation of vascular protection in tissue ablation by nonthermal irreversible electroporation," *Cardiovascular and Interventional Radiological*, vol. 35, pp. 383–390, 2012.

[73] T. W. Wong, C. H. Chen, C. C. Huang, C. D. Lin, and S. W. Hui, "Painless electroporation with a new needle-free microelectrode array to enhance transdermal drug delivery," *Journal of Controlled Release*, vol. 110, pp. 557–565, 2006.

[74] R. S. Son, T. R. Gowrishankar, K. Smith, and J. C. Weaver, "Modeling a conventional electroporation pulse train: Decreased pore number, cumula-

tive calcium transport and an example of electrosensitization," *IEEE Trans. Biomed. Eng.*, vol. 63, no. 3, pp. 571–580, 2016.

[75] C. Merla, A. Paffi, F. Apollonio, P. Leveque, G. D'Inzeo, and M. Liberti, "Microdosimetry for nanosecond pulsed electric field applications: A parametric study for a single cell," *IEEE Trans. Biomed. Eng.*, vol. 58, no. 5, pp. 1294–1302, 2011.

[76] W. Krassowska and P. D. Filev, "Modeling electroporation in a single cell," *Biophysical Journal*, vol. 92, pp. 404–417, 2007.

[77] Q. Hu and R. P. Joshi, "Model evaluation of changes in electrorotation spectra of biological cells after nspef electroporation," *IEEE Trans. Dielectr. Electr. Insul.*, vol. 17, no. 6, pp. 1888–1894, 2010.

[78] M. Leube, M. G. Notarangelo, M. Twarogowska, R. Natalini, and Poignard, "Mathematical model for transport of dna plasmids from the external medium up to the nucleus by electroporation," *Mathematical Biosciences*, pp. 1–26, 2016.

[79] T. Murovec, D. C. Sweeney, E. Latouche, R. V. Davalos, and C. Brosseau, "Modeling of transmembrane potential in realistic multicellular structures before electroporation," *Biophys J*, vol. 111, pp. 2286–2295, 2016.

[80] ©[2018] IEEE, Reprinted, with permission from, L. Mescia, M. A. Chiapperino, P. Bia, J. Gielis, and D. Caratelli, "Modeling of electroporation induced by pulsed electric fields in irregularly shaped cells." *IEEE Trans. Biomedical Engineering*, vol. 65, pp. 414–423, 2018.

[81] J. Gielis, D. Caratelli, C. M. de Jong van Coevorden, and P. E. Ricci, "The common descent of biological shape description and special functions," *Spring Proceeding in Mathematics & Statistics*, pp. 1–13, 2018.

[82] S. Zhou, X. Huang, Q. Li, and Y. M. Xiei, "A study of shape optimization on the metallic nanoparticles for thin-film solar cells," *Nanoscale Research Letters*, vol. 8, pp. 1–6, 2013.

[83] J. Gielis, "The geometrical beauty of plants," *Atlantis Press*, pp. 87–90, 2017.

[84] J. Gielis, E. Bastiaens, T. Krikken, A. Kiefe, and M. de Blochouse, "Variational superformula curves for 2d and 3d graphic arts," *Proceedings SIGGRAPH 2004*, p. 1, 2004.

[85] D. Caratelli, L. Mescia, P. Bia, and O. Stukach, "Fractional-calculus-based FDTD algorithm for ultrawideband electromagnetic characterization of arbitrary dispersive dielectric materials," *IEEE Trans. Antennas Propag.*, vol. 64, pp. 3533–3544, 2016.

[86] T. Kotnik and D. Miklavcic, "Theoretical evaluation of the distributed power dissipation in biological cells exposed to electric fields," *Bioelectromagnetics*, vol. 21, pp. 385–394, 2000.

[87] S. M. S. Mart, J. Sebastin, M. Sancho, and G. Alvarez, "Modeling normal and altered human erythrocyte shapes by a new parametric equation: Application to the calculation of induced transmembrane potentials," *Bioelectromagnetics*, vol. 27, pp. 521–527, 2006.

[88] clinicalgate.com/smooth-muscle-and-the-cardiovascular-and-lymphatic systems/.

[89] J. Medlock, A. A. K. Das, L. A. Madden, D. J. Allsup, and V. N. Paunov, "Cancer bioimprinting and cell shape recognition for diagnosis and targeted treatment," *The Royal Society of Chemistry*, 2017.

[90] Y. Polevaya, I. Ermolina, M. Schlesinger, B. Ginzburg, and Y. Feldman, "Time domain dielectric spectroscopy study of human cells ii. normal and malignant white blood cells," *Biochimica et Biophysica Acta*, vol. 1419, pp. 257–271, 1999.

[91] K. H. Schoenbach, B. Hargrave, R. P. Josh, J. F. Kolb, R. Nuccitelli, C. Osgood, A. Pakhomov, M. Stacey, R. J. Swanson, J. A. White, S. Xiao, J. Zhang, S. J. Beebe, P. F. Blackmore, and E. S. Buescher, "Bioelectric

effects of intense nanosecond pulses." *IEEE Transactions on Dielectrics and Electrical Insulation*, vol. 14, pp. 1088–1109, 2007.

[92] G. Pucihar, T. Kotnik, B. Valic, and D. Miklavcic, "Numerical determination of transmembrane voltage induced on irregularly shaped cells." *Annals of Biomedical Engineering*, vol. 34, pp. 642–652, 2006.

[93] M. Legube, A.Silve, L. M. Mir, and C.Poignard, "Conducting and permeable states of cell membrane submitted to high voltage pulses: Mathematical and numerical studies validated by the experiments," *Journal of Theoretical Biology*, vol. 360, pp. 83–94, 2014.